

3D Transient Modeling of Thin-Film Coated Surfaces to Predict
the Temperature and Ablated Areas during Laser Processing

by

Babak Baradaran Naghshine

M.Sc.Eng, Isfahan University of Technology, 2014

A Thesis Submitted in Partial Fulfillment of
the Requirements for the Degree of

Masters of Science in Engineering

In the Graduate Academic Unit of Mechanical Engineering

Supervisor: Amirkianoosh Kiani, PhD, Mechanical Engineering

Examining Board: Andrew Gerber, PhD, Mechanical Engineering
Andy Simoneau, PhD, Mechanical Engineering (chair)
Felipe Chibante, PhD, Chemical Engineering

This thesis is accepted by the
Dean of Graduate Studies

THE UNIVERSITY OF NEW BRUNSWICK

August, 2017

© Babak Baradaran Naghshine, 2017

Abstract

Increasing the biocompatibility of biomaterials is a hot topic in biomedical engineering. Introducing new surface modification methods, that can just slightly enhance the biocompatibility can directly improve the quality of lives of thousands or millions of people all around the globe. The main goal of this thesis is to study laser processed thin film multilayer structures which can be potentially used for biomedical applications.

In this thesis, the laser treatment process is numerically modeled to predict the temperature field and surface profile for each set of laser parameters including the average power, repetition rate and scanning speed. The model is successfully verified with experimental measurements. The same model was modified for laser processing of thin film coated metals. The results show that applying a thin film on the surface can completely change the temperature field and make the heat affected zone smaller or larger.

A new surface modification method is introduced by combining laser processing and electrospinning technique. In this method, the surface is processed by laser beam and then it is coated with an electrospun thin layer. This method has potential applications in bone implant fabrication. The implant can benefit from excellent biocompatibility of the electrospun layer in short-term, before the fibers are degraded, as well as long-term biocompatibility of the laser treated surface. In vitro tests showed that, this method can improve the biocompatibility, especially when the laser processed surface is coated with nanoscale fibers. Furthermore, it is shown that, by applying the electrospun layer on the surface, the thermal conductivity of the surface is closer to human body's conductivity. It

makes it an attractive method for modification of dental implants, where the cells can be damaged while drinking a hot beverage. Additionally, antibacterial agents (e.g. silver and ampicillin) were added to the fibers as an antibacterial agent, to prevent implant infection.

Acknowledgements

I would like to express my gratitude and appreciation to Dr. Kiani. It was impossible to complete this project without his support and guidance and he helped me to become a better researcher over past two years.

Also, I would like to thank Dr. Shawn MacLellan, Dr. Felipe Chibante and Dr. Huining Xiao who generously let me use their facilities and helped me to conduct my experimental tests.

To my colleagues Mitra Radmanesh, Candace Colpitts, Sarah Hamza, Will Zhao, James Cosman, Chirag Paladiya and Amin Ektesabi for their help and support and a special thank to my committee members for their valuable feedback.

Finally, I'd like to thank New Brunswick Innovation Foundation (NBIF) and the National Sciences and Engineering Research Council (NSERC) for their financial support.

Table of Contents

Abstract	ii
Acknowledgements	iv
List of Figures	vii
List of Tables.....	x
Nomenclature	xi
Introduction	1
1.1 Motivations and background	1
1.1.1 Biomaterials and biocompatibility	3
1.1.2 Bone implants.....	4
1.1.3 Biological, chemical and physical requirements for bone implants.....	5
1.1.4 Different categories of biomaterials	6
1.1.5 Surface modification for biocompatibility enhancement	6
1.1.6 Thermal models for laser processing	8
1.1.7 Thin film deposition techniques	10
1.1.8 Electrospinning technique	12
1.1.9 Implant-related infection.....	15
1.2 Research objectives	16
Methodology	17
2.1 Experimental methods and equipment	17
2.1.1 Laser processing.....	17
2.1.2 Electrospinning.....	18
2.1.3 Three-dimensional (3D) optical microscopy.....	18
2.1.4 Scanning Electron Microscopy (SEM)	19
2.1.5 Energy Dispersive X-ray (EDX).....	20
2.1.6 X-Ray Diffraction (XRD)	20
2.1.7 Simulated Body Fluid (SBF) Immersion	21
2.1.8 Antibacterial testing	22
2.1.9 Thermal conductivity measurement.....	22
2.2 Numerical methods	23
2.2.1 2D heat equation and ADI method.....	24
2.2.2 3D heat equation and Douglas-Gunn method	25
2.3 Samples and objects of study	27

2.4 Validity and reliability of the measurements	28
2.5 Assumptions	28
Thermal modeling of laser processing on a metallic surface	29
3.1 Temperature calculations	30
3.2 Boundary conditions	31
3.3 Phase change and ablation.....	31
3.4 Plasma shielding and power loss.....	35
3.5 Numerical and experimental results for laser processing of a titanium sheet	36
Laser processing of a thin film coated surface	41
4.1 Materials and sample preparation	41
4.2 Laser processing of bare silicon sheets	43
4.3 Laser processing of aluminum coated silicon sheets	49
4.4 Laser processing of gold coated silicon sheets.....	54
Potential use of laser treated metallic surfaces coated by a thin layer of electrospun fibers for implant fabrication.....	59
5.1 The proposed method	60
5.2 Sample preparation.....	61
5.3 Biocompatibility assessment	62
5.4 Thermal analysis of a dental implant coated by electrospun fibers while drinking a hot beverage	66
5.5 Adding antibacterial agents to the fibers	73
Summary and future work.....	77
6.1 Summary	77
6.2 Future work	79
References	81
Appendix A – Physical and thermal properties of the materials.....	89
Aluminium	89
Gold.....	90
Silicon.....	90
Titanium	91
Appendix B – Laser processing simulation software.....	92
Appendix C – List of publications	96
Curriculum Vitae	

List of Figures

Figure 1 - Electrospinning setup _____	13
Figure 2 – Various signals generated as a result of interaction between electron beam and the surface _____	19
Figure 3 – (a)Thermal conductivity [78], (b)specific heat [78] and (c)Absorption [79] as a function of temperature _____	31
Figure 4 – The computational flowchart at each time step _____	33
Figure 5 – The flowchart of evaporation _____	34
Figure 6 – Plasma absorption for laser processing of titanium sheets used in this study	36
Figure 7 – (a) Average calculated ablation depth vs. average measured depth (b) Maximum calculated ablation depth vs. maximum observed depth _____	37
Figure 8 – Ablation depth vs. frequency at (a) power=5 W, scanning speed=200 mm/s (b) power=10 W, scanning speed=200 mm/s (c) power=10 W, scanning speed=700 mm/s	38
Figure 9 – (a) Ablation depth vs. power at frequency=50 kHz, scanning speed=200 mm/s (b) Ablation depth vs. scanning speed at power=10 W, frequency=50 kHz _____	38
Figure 10 – (a) Variations of ablation depth of a single point during the process for different frequencies at power=10 W, scanning speed=200 mm/s (b) Variations of ablation depth of a single point during the process for different scanning speeds at power=10 W, frequency=50 kHz (c) Ablation depth during a single pulse at power=10 W, scanning speed=200 mm/s _____	39
Figure 11 – Cross section of the ablated zone and maximum temperature at power=5 W, scanning speed=200 mm/s and (a) frequency=25 kHz, pulse duration=22 ns (b) frequency=50 kHz, pulse duration=36 ns (c) frequency=60 kHz, pulse duration=42 ns and measured groove profile at the same power and scanning speed and (d) frequency=25 kHz (e) frequency=50 kHz (f) frequency=60 kHz. _____	39
Figure 12 – (a) Maximum surface temperature at power=5 W, frequency=50 kHz and scanning speed=200 mm/s (b) Color change on the surface for the same laser parameters _____	40

Figure 13 – (a) Isolated pulse on the surface of silicon, (b) Isolated pulse on the surface of aluminum, (c) Isolated pulse on the surface of gold	42
Figure 14 – (a) Thermal conductivity of silicon [86], (b) specific heat of silicon [86], (c) absorbance of silicon [87].	43
Figure 15 - Plasma absorption for laser processing of silicon sheets obtained from experimental results	44
Figure 16 – (a) Measured profile at 5 W and 25 kHz, (b) measured profile at 5 W and 50 kHz, (c) calculated profile at 5 W and 25 kHz, (d) calculated profile at 5 W and 50 kHz, (e) calculated profile at 5 W and 75 kHz.	45
Figure 17 – Shallow holes formed on the surface of the silicon sample at 75 kHz and 5 W	46
Figure 18 – (a) Measured profile at 5 W and 50 kHz, (b) measured profile at 10 W and 50 kHz, (c) measured profile at 15 W and 50 kHz, (d) calculated profile at 5 W and 50 kHz, (e) calculated profile at 10 W and 50 kHz, (f) calculated profile at 15 W and 50 kHz.	47
Figure 19 – Temperature contour at the end of the pulse at 25 kHz and 5 W for (a) cross-section (b) surface	48
Figure 20 – (a) Thermal conductivity of aluminum [88], (b) specific heat of aluminum [88], (c) absorbance of aluminum [87].	49
Figure 21 - Plasma absorption for laser processing of aluminum obtained from experimental results	50
Figure 22 – (a) Measured profile at 5 W and 25 kHz, (b) measured profile at 5 W and 50 kHz, (c) measured profile at 5 W and 75 kHz, (d) calculated profile at 5 W and 25 kHz, (e) calculated profile at 5 W and 50 kHz, (f) calculated profile at 5 W and 75 kHz.	51
Figure 23 – (a) Measured profile at 5 W and 50 kHz, (b) measured profile at 10 W and 50 kHz, (c) measured profile at 15 W and 50 kHz, (d) calculated profile at 5 W and 50 kHz, (e) calculated profile at 10 W and 50 kHz, (f) calculated profile at 15 W and 50 kHz.	52
Figure 24 – Temperature contour at the end of the pulse at 50 kHz and 5 W for (a) cross-section (b) surface	53
Figure 25 – (a) Thermal conductivity of gold [89], (b) absorbance of gold [87]	54

Figure 26 - Plasma absorption for laser processing of gold obtained from experimental results _____	55
Figure 27 – (a) Measured profile at 5 W and 25 kHz, (b) measured profile at 5 W and 50 kHz, (c) measured profile at 5 W and 75 kHz, (d) calculated profile at 5 W and 25 kHz, (e) calculated profile at 5 W and 50 kHz, (f) calculated profile at 5 W and 75 kHz ____	55
Figure 28 – (a) Measured profile at 5 W and 50 kHz, (b) measured profile at 10 W and 50 kHz, (c) measured profile at 15 W and 50 kHz, (d) calculated profile at 5 W and 50 kHz, (e) calculated profile at 10 W and 50 kHz, (f) calculated profile at 15 W and 50 kHz. _	56
Figure 29 – Temperature contour at the end of the pulse at 50 kHz and 5 W for (a) cross-section (b) surface _____	58
Figure 30 - Combination of laser processing and electrospinning _____	60
Figure 31 - SEM images of sample surfaces before SBF immersion. A) nanofibers B) microfibers _____	62
Figure 32- SEM images of samples with microscale fibers after SBF immersion. A) unprocessed sample, 5000X magnification B) laser-processed sample, 5000X magnification _____	63
Figure 33 - SEM images of samples with nanoscale fibers after SBF immersion. A) Unprocessed sample, 100X magnification; B) laser-processed sample, 100X magnification; C) unprocessed sample, 5000X magnification; D) laser-processed sample, 5000X magnification _____	63
Figure 34 - EDX analysis of A) unprocessed nanoscale sample B) processed nanoscale sample C) unprocessed microscale sample D) processed microscale sample _____	64
Figure 35 - XRD analysis of samples _____	65
Figure 36 - Cross-sectional view of crown, implant, fibers and bone _____	68
Figure 37 - Temperature rise of fibrous layer after applying a 200 mW heat source for A) microscale sample B) nanoscale sample _____	71
Figure 38 - Maximum bone temperature while drinking hot coffee, considering an implant without any fiber and implants covered with a layer of electrospun nanoscale fibers with three different thicknesses. _____	72
Figure 39 – The flowchart of the computational code _____	73

Figure 40 – Antibacterial testing of the fibers containing silver nanospheres against wild type E. coli.	74
Figure 41 - Antibacterial testing of the ampicillin loaded fibers (labeled as “H” in the images) and fibers soaked in ampicillin (labeled “D” in the images) against wild type E. coli.	75
Figure 42 – The laser processing program	92
Figure 43 – Input values for laser processing of bulk materials and thin film multilayer structures.	93
Figure 44 – The “Line Graph” window	93
Figure 45 – The “Contours” window	94
Figure 46 – The “3D Graph” window	94
Figure 47 – The “Report” window	95

List of Tables

Table 1 – SBF ingredients [67]	21
Table 2 – Measured and calculated ablation depths	45
Table 3 – Measured and calculated ablation depths	50
Table 4 – Measured and calculated ablation depths	56
Table 5 - Chosen parameters for electrospinning process	61
Table 6 - Mechanical and thermal properties of materials	69

Nomenclature

c_e	Entanglement Concentration
c_p	Specific heat (J/kgK)
E_a	Energy absorbed by plasma (J)
h	Convective heat transfer coefficient (W/m ² K)
$h_{ablation}$	Ablation depth (m)
k	Thermal conductivity (W/mK)
L_f	Latent heat of fusion (J/kg)
L_v	Latent heat of vaporization (J/kg)
P	Porosity
q''_{laser}	Laser pulse flux (W/m ²)
$q''_{metabolism}$	Metabolic rate (W/m ³)
T	Temperature (K)
t	Time (s)
α	Absorption
α_{plasma}	Plasma absorption
α_{max}	Maximum plasma absorption
Δt	Time step (s)
ε	Emissivity
Λ	Optical thickness

ρ	Density (kg/m ³)
σ	Stefan–Boltzmann constant (W/m ² K ⁴)
ψ	Non-dimensionalized pulse power
ω	Blood perfusion rate (ml/min/100g)

List of Acronyms

ADI Method – Alternating Direction Implicit Method

CVD – Chemical Vapor Deposition

ECM – Extracellular Matrix

EDX – Energy Dispersive X-ray

HA – Hydroxyapatite

HAZ– Heat Affected Zone

LB – Lysogeny Broth

MEMS – Microelectromechanical systems

MSC – Mesenchymal Stem Cells

NEMS – Nanoelectromechanical systems

PBS – Phosphate-Buffered Saline

PCL – Polycaprolactone

PEO – polyethylene Oxide

PLGA – Poly(lactic acid)-co-poly(glycolic acid)

PVD – Physical Vapor Deposition

SBF – Simulated Body Fluid

SEM – Scanning Electron Microscopy

TFT – Thin Film Transistor

TPS – Transient Plane Source

XRD – X-Ray Diffraction

Chapter 1

Introduction

1.1 Motivations and background

Laser processing is a fast and easy method that has been studied previously for increasing the biocompatibility of metallic surfaces [1-7]. Since metals are the most popular materials used in bone implant fabrication, their surface can be processed by laser beam to make them more biocompatible and minimize the risk of rejection without affecting the chemical and mechanical properties of the bulk material. This method can even turn a non-biocompatible metal into a biocompatible material [4, 5]. In most of the previous studies, a bulk material was laser processed and thin film coated metals were almost completely ignored. However, laser processing of thin film coated materials can open new

doors to biomedical engineers. Coating the surface with a different material to improve the electrical properties for potential use as a biosensor or coating the laser processed surface with a polymeric layer to further improve the biocompatibility are some examples. In this project, laser processing of the thin film coated metals is studied through a numerical analysis. Also, a series of experimental tests were carried out that shows how coating a laser processed surface by a thin electrospun fibrous film can make further improvement in biocompatibility of the surface.

Additionally, laser processing of thin film multilayer structures can have many applications in other branches of engineering. For example, one of the methods to fabricate poly-Si thin film transistors (TFTs) is based on laser processing of thin films. In this method, a thin film of amorphous silicon (a-Si) is deposited on a glass substrate and it is processed by a UV laser beam. Since a-Si has a very high absorption at UV spectrum, it can be recrystallized into poly-Si by the laser beam without causing any considerable temperature change in the substrate [8-10]. There are also various laser doping techniques such as spin coating the Si layer with a phosphorus or boron containing liquid before the laser processing the surface for n and p type TFTs respectively [11]. Controlling the grain size of the resulting poly-Si layer is vital in this process [9, 10]. This can be only obtained by controlling the temperature of the thin film and its cooling rate during laser processing. As the process occurs at a very short time it's extremely difficult to measure the temperature and a proper thermal model can be the most useful tool for controlling the temperature.

Despite the necessity of the thermal modeling of laser processing of thin film multilayer structures, there have been very few efforts in this area so far. In the previous works, only simple one dimensional models were used to calculate the temperature of different thin film structures without considering the phase change [12, 13].

1.1.1 Biomaterials and biocompatibility

Biomedical engineering is one of the fastest growing branches of science and engineering, which had a great impact over our lives recently. Use of almost any biomaterial requires a direct contact between an external object and human body (skin, tissue, bone, etc.). Obviously, it is critical to make sure that this external object doesn't trigger an aggressive response from the immune system and also it doesn't cause any irritation, inflammation, disease or other undesirable side effects. For this reason, the study of biomaterials has attracted many attentions recently to find the best artificial or natural materials that are less prone to rejection. This concept is usually addressed as biocompatibility, which is an ambiguous term that has different definitions in the literature [14, 15]. The term appeared in the literature for the first time in the 70s and the most accepted definition of biocompatibility is "the ability of a material to perform with an appropriate host response in a specific application" [14, 15]. This definition clearly shows that a "desirable" response is expected and the biomaterials should be thoroughly examined, to make sure all the biological interactions are beneficial for the specific application we have in mind.

1.1.2 Bone implants

There are many different types of medical devices that make extensive use of biomaterials for different applications. The most common ones are scaffolds for tissue engineering and bone implants. Scaffolds are usually made of a biodegradable polymer, and play the role of the Extracellular Matrix (ECM) and provide the structural support required for tissue growth and remodeling [16]. Bone implants are usually made of a metal and are used for mechanical support to an injured bone or they can be used to replace a bone permanently [17]. The most common types of bone implants are hip replacement implants and dental implants. Desirable implants should have mechanical properties close to those of bone. Titanium has strength, corrosion resistance and low density besides good chemical stability and biocompatibility, which makes it the most popular material for fabrication of bone implant. It is of crucial importance to enhance the biocompatibility of titanium as much as possible in order to minimize the risk of implant rejection. This is usually done by modifying the surface, where direct contact with tissue or bone occurs.

Clinical hip replacement surgeries were performed as early as 60s [18] and rejection has always been an issue. Since the surgery is very painful and requires a long recovery time, rejection can be a serious problem. Many surface modification techniques were proposed and studied since then to prevent implant rejection as much as possible. Thanks to those studies, the bone implants are now cheaper, more easily accessible and more efficient compared to a few decades ago. However, rejection is still happening. The rejection rate of dental implants, which are one of the simplest and most common types of bone implants is still as high as 1.6% [19].

As we age, our bone density will drop and it cannot perform well inside the body anymore. Since life expectancy has been increased significantly during the past few decades, this issue has become even more important. It means more implants are needed every year around the world. An enormous increase in the number of hip (137%) and knee (607%) replacement surgeries has been predicted between the years 2005 and 2030 [20], which shows there is a promising market for improved biomaterials with better biocompatibility.

1.1.3 Biological, chemical and physical requirements for bone implants

As explained in section 1.1.1, the term biocompatibility, usually implies some sort of desirable biological responses inside the body. For bone implants, the most important biological response is osseointegration.

Osseointegration is defined as “A direct structural and functional connection between ordered, living bone and the surface of a load-carrying implant” [21]. This means a direct and strong contact between the bone and implant is required in order to achieve a successful implantation. In some cases, a fibrous capsule will be formed around the implant, which may cause inflammation and can lead to rejection.

On the other hand, the material must have a high corrosion resistance. Otherwise, non-biocompatible ions will be released in the body as a result of contact with extracellular body fluid [17]. The physical properties such as density and thermal conductivity should be as close as possible to the bone and obviously, it must have a high yield strength.

1.1.4 Different categories of biomaterials

There are three main categories of biomaterials based on their interaction with human tissue:

1. Biotolerant materials, that form a very thin connective tissue capsule (0.1-10 μm) after a while. However, the bonding between the surface and tissue is very poor.
2. Bioactive materials promote a strong biological response and bone-like tissue will be formed and strongly adhered to their surface.
3. Bioreabsorbable materials are the ones that will be degraded inside the body after a certain amount of time.

Obviously, none of the materials from the first category are suitable for implant fabrication and bioreabsorbable materials can only be used for surface coating or absorbable implants and scaffolds, whereas bioactive materials are widely used in fabrication of medical implants.

1.1.5 Surface modification for biocompatibility enhancement

Metallic implants are usually subjected to surface modification in order to increase their biocompatibility and reduce the rejection rate. Since all the biological interactions happen on the surface of the implant [22], the biocompatibility will be enhanced only by modifying the surface without causing any considerable changes in the bulk properties. These modifications include surface chemistry, topography, roughness and surface energy [17]. Microscale surface roughness has been proven to have a positive effect on biocompatibility. Generally, by increasing the surface roughness the osseointegration is

more likely to happen. Increasing the porosity is another way to enhance the biocompatibility. This is mainly done by tissue growth inside the pores [23]. Increasing the surface energy can also help the osseointegration process, since the material has a better wettability and it's more likely to be accepted by the body [24]. Jayaraman et al. showed that grooved surfaces are more biocompatible than randomly rough surfaces [25].

In some methods, the material is coated by a more biocompatible material such as hydroxyapatite, in order to increase the biocompatibility. Heat treatment and thermal oxidation are the other method that improve the biocompatibility. Moreover, different methods have been introduced to increase the surface roughness and make a porous structure on the surface. Sand blasting, polishing and acid etching are some examples [17, 23].

These methods are time consuming and expensive in some cases. Laser processing is another method for modifying surface texture and increasing biocompatibility; it is faster and the whole surface can be patterned in few seconds. Laser processing can also improve biocompatibility in other ways. Surface temperature will be increased drastically after laser irradiation, and this causes surface oxidation [24]. Titanium is the most common material used in fabrication of bone implants and it is known that TiO_2 is a bioactive layer on the surface of Ti that can improve cell attachment and osseointegration [26]. In addition, a high-temperature plasma plume will be formed due to laser ablation. As soon as the laser beam is turned off, suspended particles will collide and form an interwoven fibrous structure that increases porosity on the surface and consequently enhances the

biocompatibility [24]. Radmanesh and Kiani showed that patterning the Ti surface using a low-cost nanosecond laser system would be enough for a considerable increase in cell adhesion and biocompatibility of Ti sheets [2]. Colpitts and Kiani used the same nanosecond laser system to turn silicon into a biocompatible material [4].

1.1.6 Thermal models for laser processing

With recent developments in MEMS/NEMS device fabrication, there is an inevitable demand for new machining methods, since the conventional methods cannot be used in micro/nanoscale. Laser processing is one of the most popular methods used in micro/nano manufacturing. It is widely used for cutting, drilling and heat treatment as well as for texturing a solid material.

Processing the surface of a material, which is the main focus of this study, has various applications in small scale device fabrication and biomedical engineering [1, 27, 28]. Mathematical modeling of this process can provide us with useful information about heat affected zones, molten zones and topology of the surface after laser processing. Almost the whole process can be explained by laws of thermodynamics and heat transfer, except when the pulse duration is extremely small (e.g. when it is in femtosecond range), where we are in the domain of cold ablation [29, 30]. Ultra short pulses can be modeled using different techniques such as two-temperature model [31] or molecular dynamics [32]. There have been numerous efforts in the past to propose a proper thermal model for the interaction between a solid surface and laser beam in hot ablation domain. These works can be categorized in three different groups [33].

In the first category, the 1D or 2D heat conduction equation was analytically solved to calculate the temperature distribution around the irradiated zone. Hendow and Shakir used an analytical solution of the 2D heat conduction equation to calculate the temperature distribution and predict the ablation zone [34]. Ho et al. solved the 2D heat conduction equation and considered the shape of interface between solid and vapor in their equation to predict the ablated zone [35]. Chen et al. analytically solved the 2D equation for repetitive laser pulses [36]. The problem with these analytical solutions is that, a wide range of simplifying assumptions must be made to make the equation solvable. For instance all the thermal properties are considered to be constant.

The second category consists of numerical solutions of the heat conduction equation. Ren et al. Solved the 2D equation using ANSYS CFX without considering ablation [37]. Shukla and Lawrance used NX 5.0 to solve the 3D conduction equation, considering phase change [38]. Weidmann et al. solved the 2D equation for calculating the temperature distribution and used the Arrhenius equation to estimate the speed of ablation and predict the ablated zone [39]. Sinha solved the 2D equation and took phase changes in his model to predict the ablation zone. In this model the size of computational cells was decreased when their temperature exceeded boiling point to model evaporation [40]. Marla et al. presented another model that solved the 1D equation considering temperature-dependent thermal properties. In their model, ablation was modeled using Knight's theory of vaporization [41] and plasma shielding was also considered in the equations [42]. Foroozmehr et al. simulated laser processing of the powder bed considering optical penetration depth of the powder and using a simple porous media model in ANSYS CFX

[43]. In some models, a two-phase model is used by solving the Navier-Stokes equations and heat conduction equation simultaneously to model the ablation process. An example can be seen in the work of Zhang et al. [44].

In the third category, non-physical Artificial Intelligence (AI)-based methods such as Artificial Neural Network (ANN), Fuzzy Expert System (FES) and Extreme Learning Machine (ELM) are used, which are beyond the scope of this project [33, 45]. Although a wide range of methods have been proposed which fall into these three categories, they still suffer from lack of accuracy, long processing time and limited capability.

1.1.7 Thin film deposition techniques

Thin film deposition is a cost-efficient method to alter the physical and chemical properties of a surface without changing the bulk material's properties. In this method, just a minimal amount of the additive material is needed, because the thickness of the layer doesn't exceed a few micrometers in most cases. It enables us to make use of extremely expensive materials such as gold, platinum or silver for a reasonable price. For example, since gold is a very biocompatible material and also has a very high electrical conductivity making it a very interesting candidate for biosensor fabrication [46, 47].

There are countless techniques for thin film deposition. Most of these techniques fall within one of the two following categories: Physical Vapor Deposition (PVD) and Chemical Vapor Deposition (CVD) [48].

In PVD methods, thin film deposition happens through purely physical processes. The desired source material is evaporated and then it will be condensed as a thin film on the

surface of the substrate. There are plenty of different PVD methods that can be classified based on the energy source used for the evaporation process. The most simple method is thermal evaporation which is usually done in vacuum [48]. Arc-PVD is another method, where the material is evaporated by an electric arc. The apparatus, usually consists of a vacuum pump, an anode, the arc ignitor, the arc power supply, the substrate and the source material which plays the role of the cathode in the circuit [49]. In Electron Beam PVD (EB-PVD), electron beams are used to evaporate the source material in a vacuum. In this process the substrate is usually heated to gain better fusion between the substrate and thin film [50]. Sputtering is another method which is very similar to EB-PVD, where the surface is bombarded by ions instead of electron beam [48]. Pulsed laser deposition is another PVD technique, where the material is evaporated using a laser beam [48].

The high temperatures needed in PVD techniques to evaporate the source material may affect the chemical and physical properties of the substrate. If the boiling temperature of the source material is very high, PVD can be completely impossible. On the other hand, CVD techniques mostly rely on chemical reactions on the surface and they don't alter the properties of the substrate. Therefore, they can be used for a much wider range of materials. Also, since chemical reactions are involved the bonding would be stronger than thin films deposited by PVD techniques. Moreover, the quality of the deposited film is usually better in CVD techniques and a better step coverage can be achieved. In this method, gaseous chemical compounds are diluted with an inert gas, which passes over the surface of the substrate and will be deposited on the surface as chemical reactions are happening between the gas and the surface. CVD techniques are categorized based on the

conditions in their reaction chamber. The most common ones are Atomic Pressure CVD (APCVD), Low-Pressure CVD (LPCVD) and Plasma-Enhanced CVD (PECVD) [48].

1.1.8 Electrospinning technique

Electrospinning is one of the most popular methods to generate micro/nanoscale polymeric fibers. In this method, the electrostatic forces are manipulated to generate small-scale fibers. The electrospinning apparatus has four main parts: needle, pumping system, high voltage supply and collector (Figure 1). The polymer should be in liquid phase for a successful electrospinning process. Therefore, it must be dissolved in a proper solvent. The polymeric solution should be pumped to the needle at a constant flow rate. If the flow rate is adjusted properly, a big droplet will be formed at the tip of the needle due to surface tension. After applying a high voltage to the needle, collector or both, and gradually increasing it, the droplet will be deformed to a cone because of electrostatic forces. This cone is known as Taylor cone [51]. By further increasing the voltage, at a certain point, the electrostatic forces will overcome surface tension and fibers will be generated at the tip of the needle. The solvent will be evaporated before the fibers reach the collector. By aiming these fibers to a substrate, a thin fibrous layer will be deposited on the surface.

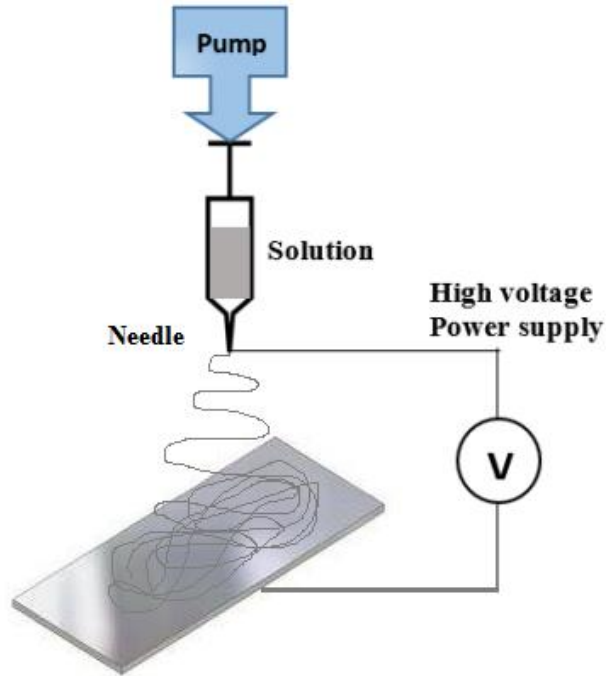


Figure 1 - Electrospinning setup

The electrospinning process can be controlled through different parameters. Flow rate is an important parameter that directly affects the size and quality of the fibers. Usually higher flow rates will result in fabrication of larger fibers [52]. The distance between the needle and collector is another easy parameter to control. Usually by increasing the distance, the fibers become smaller. However, this is not true for all the polymer [53]. If the distance is shorter than a minimum amount, no fibers will be generated, because the solvent does not have enough time to evaporate [54]. On the other hand, if the distance is too long, there would be lots of beads and junctions in the fibers [53]. The other controllable parameter is voltage. Even though it has no considerable effect on the size [53], it can control the quality of fibers. Generally, if the voltage is too low or too high, the fiber web is more prone to form junctions and beads [52, 55]. Concentration of the solution also plays an important role. Usually larger fibers are obtained by increasing the

concentration [53]. Each polymer is electrospinnable only in a limited concentration range. The concentration should be higher than a minimum amount called the entanglement concentration (c_e). Also, it was reported that for most polymers, bead-less electrospinning only happens at a concentration approximately 2-2.5 times higher than c_e [56].

Solution's properties can also be manipulated by adding an additive material to control the process. However, it is difficult to isolate the effect of adding the additive material on a single parameter without affecting the other physical and chemical properties of the solution. Increasing the solution's conductivity can reduce the beading in the fiber web. This is usually done by adding salt or alcohol to the solution. The fiber size is also increased by making the solution more conductive [53]. Surface tension is another parameter that can affect the size and quality of fibers [53]. However, different materials do not behave the same after increasing or decreasing the surface tension [57, 58]. Molecular weight of the polymer is the other parameter. Some polymers are only spinnable in a certain range of molecular weights. Although, increasing the molecular weight usually improves the quality of fibers [59], it does not have a significant effect on the size [60]. The shape and composition of the needle and collector can also have a significant effect on the process. Additionally, ambient conditions such as room temperature and humidity can affect the quality of the fibers [53].

Compared to metals, biopolymers have more resemblance to biological media. For this reason, a layer of electrospun fibers of suitable biopolymers can considerably enhance the biocompatibility. Additionally, the high porosity of the fibrous structure and its

significantly higher wettability in comparison with metals will further increase the biocompatibility. Using a nanofiber coating, even with man-made polymers such as poly(lactic acid)-co-poly(glycolic acid) (PLGA), was proven to increase adhesion of Mesenchymal Stem Cells (MSC) on a titanium plate and alloy [61]. Chen et al. investigated the effect of fiber diameter on cell adhesion. Their results show that smaller fibers have better cell adhesion in nanoscale regions whereas increasing the diameter in the microscale region had no effect on cell adhesion [62]. Some special components can be also added to fibers to enhance the integration. For instance, collagen is often used for this purpose [61, 63]. Li et al. [64] and Zhang et al. [65] added gentamicin and vancomycin to their polymeric solutions to fabricate antibacterial electrospun fibers that can prevent implant-related infections. Electrospun fibers are recently used in fabrication of dental implants and it was shown that, the contact between gingival tissue and implant is significantly improved using collagen nanofibers [66].

1.1.9 Implant-related infection

Implant infection is a serious problem that can cause pain, implant rejection or even death if remains untreated. On the other hand, the only effective treatment in these cases is removing the implant and redoing the surgery [64]. The main cause of implant infection is bacterial contamination and it can be prevented by adding antibiotics or other antibacterial agents to the surface of the implant. A few studies have been conducted on adding antibiotics to electrospun fibers in order to prevent implant-related infections. Li et al. added gentamicin to PLGA/PEO fibers and the fibers showed a significant antibacterial activity [64]. Zhang et al. studied the effect of adding Vancomycin to PLGA

fibers. They showed that the Vancomycin has a very slow release rate and the fibers were still able to kill the bacteria even after 28 days [65]. Silver nanospheres and ampicillin were used as antibacterial agents in this study. By adding these agents to the fibers, we can decrease the risk of infection.

1.2 Research objectives

The main goal of this thesis is to study the application of laser processed and thin film coated surfaces to enhance their biocompatibility for their potential use as biomedical devices.

The main objectives of this research are listed as follows:

- 1- To study the physical properties of the material and laser parameters that can affect the topography and chemical composition of the surface during the laser processing process.
- 2- To develop a numerical model for nanosecond laser pulses in order to gain a better understanding of the physical processes occurring during the laser processing of single or multilayer surfaces.
- 3- To examine the feasibility of combining laser processing and electrospinning as two different surface modification methods for better implant fabrication.
- 4- To study the effect of coating an implant by electrospun fibers on its thermal properties.
- 5- To examine the possibility of adding antibacterial agents to the fibrous layer to prevent implant infection.

Chapter 2

Methodology

2.1 Experimental methods and equipment

2.1.1 Laser processing

In this project, the material is processed using an Nd:YAG nanosecond laser system (Bright Solutions SOL-20). Frequency of laser pulses can be selected and power can be controlled by changing the level of emission. Also, the pattern, line distance and scanning speed are controlled by EZCAD© software. The wavelength is 1064 nm and pulse duration is in the range of 6-60 ns and is read from performance curves provided by the manufacturer for each power and frequency. The diameter of the circular output beam is reduced from 9 mm to 8mm using an iris diaphragm. The galvo scanner (JD2204 by Sino-Galvo) has an input aperture of 10 mm and beam displacement of 13.4 mm. In order to

focus the normal beam onto the surface of the samples, a scan lens with a focal length of 63.5 mm was used along with the galvo scanner system. The theoretical focused beam spot diameter was calculated to be around 20 μm .

2.1.2 Electrospinning

The system chosen for carrying out electrospinning tests was the YFlow[®] StartUp Electrospinning Lab Device, “addressed for process design of core-shell nanofibers and nanospheres.” The electrospinning technique was performed with polycaprolactone as the spun polymer in solution and titanium as the target substrate.

Polycaprolactone (PCL) is a semi-crystalline, aliphatic polymer with known biodegradability, good biocompatibility, and mechanical strength [67]. Acetone was used to dissolve the polymer as it is an environmentally benign and non-toxic solvent. Previous studies indicate acetone to be a reliable electrospinning solvent and state that it should be given greater consideration when selecting polymer/solvent systems [68]. Polymeric solutions were made via the weighing out of a known concentration of PCL and acetone into a beaker that was tightly sealed and placed into an Ultrasonic Cleaner set at 110°F and monitored to determine proper dissolution. A thermoclyne was also used to further mix the solution to a desired endpoint with low heat and high spin, as well as successive additions of acetone to the original weight due to its evaporation.

2.1.3 Three-dimensional (3D) optical microscopy

This study used the Zeta-20 Optical Profiler (Zeta Instruments) to obtain surface profile of the laser treated samples for quantitative topography measurements. This optical

profiler can capture 2D and 3D images of a surface, which allows us to see the profile of laser treated grooves and holes at different points. This equipment can also be used to find the roughness and measure the size of small features on the surface.

2.1.4 Scanning Electron Microscopy (SEM)

SEM was invented in early 30s. A conventional SEM consists of the electron column and a console. The specimen is placed inside a vacuum specimen chamber. The electron gun inside the column will emit an electron beam which scans the target surface using a condenser and objective lenses. The focal length of the objective lens is usually quite long, which keeps the picture in focus while zooming in and out. When the electron beam is interacting with the surface, various signals are generated that can be processed and displayed as an image (Figure 2). In most SEMs, secondary electrons are collected above the sample and turned into images [69].

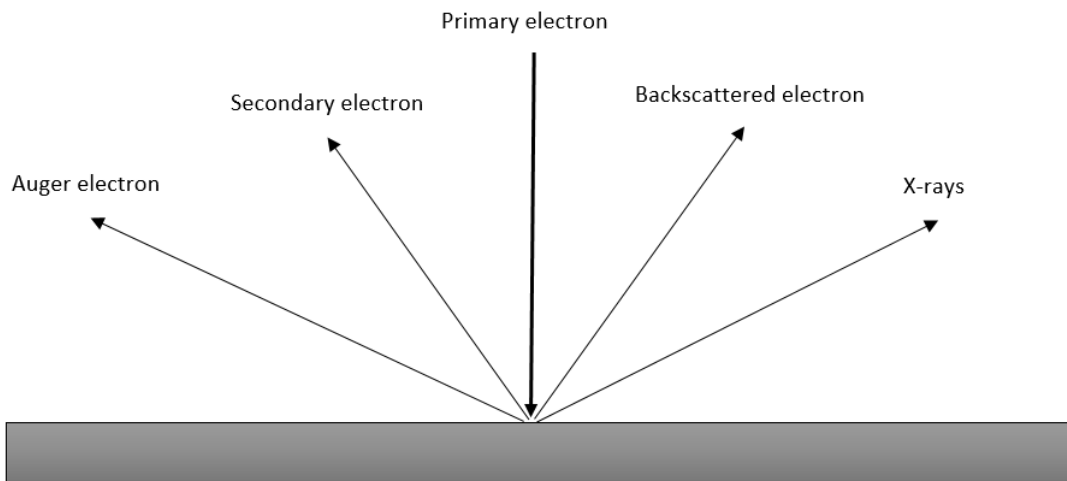


Figure 2 – Various signals generated as a result of interaction between electron beam and the surface

In this study, all the SEM images were taken using JEOL 6400 Digital SEM located in Microscopy and Microanalysis center at UNB-Fredericton campus. This equipment can visualize features as small as 100 nm.

2.1.5 Energy Dispersive X-ray (EDX)

EDX is one of the most common spectroscopy methods for elemental analysis. In this method presence of a specific element on the surface can be detected, however the exact chemical formula cannot be understood. The principles of this method are very simple. In this method, the surface is excited by the primary electrons, which results in X-ray emission (Figure 2). The energy of the emitted X-ray is unique for each element. Therefore, by collecting the emitted X-ray from surface and measuring its energy all the elements can be easily detected [70]. Usually, SEM and EDX are combined into a single instrument, since X-ray beam is already emitted from sample during SEM (Figure 2). In this study, again JEOL 6400 Digital SEM was used for EDX analysis.

2.1.6 X-Ray Diffraction (XRD)

XRD is a very common crystallography technique in which X-rays will be targeted at the surface and it will be diffracted to many different directions as it interacts with the crystal structure. By collecting the diffracted beams at different angles and measuring the intensities a few characteristic peaks can be determined which are unique for each material and crystal structure.

In this study the XRD analysis was conducted by Bruker AXS D8 XRD located at the Department of Earth Sciences on UNB-Fredericton campus [71].

2.1.7 Simulated Body Fluid (SBF) Immersion

The main concern about bone implants is to have proper bonding between bone and implant. SBF immersion is a widely used in-vitro method to assess this bonding. In this method samples are soaked in SBF for a few weeks and if bone-like Hydroxyapatite (HA) was formed on the surface, a proper fusion between bone and the surface can be expected after placing the implant inside the body. Hydroxyapatite is the main mineral component of hard tissues and is widely used in biomedical applications due to its excellent bioactivity and biocompatibility [72].

Table 1 – SBF ingredients [73]

Order	Material	Amount (gr)
1	NaCl	8.035
2	NaHCO ₃	0.355
3	KCl	0.225
4	K ₂ HPO ₄ .3H ₂ O	0.231
5	MgCl ₂ .6H ₂ O	0.311
6	HCl	0.039
7	CaCl ₂	0.292
8	Na ₂ SO ₄	0.072
9	Tris	6.118
10	HCl	0-0.005

SBF is a water based liquid that has similar inorganic ion concentrations to those of human blood plasma [74]. SBF is prepared by using chlorides, carbonates, oxides, and sulphates of alkali metals as extensively researched and performed using the Kokubo Method [75]. In this study, the SBF was prepared based on Kokubo's recipe, which involves dissolving different materials in a water based system, step by step while controlling the temperature and pH. The ingredients are listed in Table 1 for making 1000 ml of SBF [73].

In this study, samples were immersed in SBF and kept inside an incubator for four weeks and the temperature was kept constant at 37°C.

2.1.8 Antibacterial testing

The antibacterial activity of silver nanospheres and ampicillin was assessed using the agar diffusion test. In these tests, ampicillin resistant and wild type gram-negative E.coli was cultured overnight inside the incubator at 37 °C. Then 5 µl of the bacterial culture was added to the lysogeny broth (LB) and overlaid a LB agar plate. The samples were placed inside the plate and were incubated for 24 hours at 37 °C. If a circular clear zone (zone of inhibition) was formed around a sample, it means that the sample had antibacterial activity and killed all the bacteria inside the zone.

2.1.9 Thermal conductivity measurement

A Hot Disk TPS instrument was used to obtain a temperature difference curve after applying a constant heat flux on the surface. In this instrument, thermal properties are calculated by applying the Transient Plane Source (TPS) technique on measured temperature curves. With this technique, both thermal conductivity and thermal capacity

can be measured in a single shot. However, in this technique samples are assumed to be large enough in all directions, because heat transfer equations are analytically solved for an infinite solid. Therefore, a thin film multilayer sheet that is the subject of this study is not an ideal sample for Hot Disk. For this reason, only the temperature curve was extracted from this instrument and a numerical model customized for the same samples was used to find the thermal conductivity.

In this study, two multilayer sheets were placed on stainless steel cylinders with known thermal properties. The experiment was conducted in double-sided mode and the sensor was fitted between layers. In this mode, the sensor is placed between two similar samples and the heat flux is applied on the surface of the both samples. Samples were placed inside the cell and were left there for 60 minutes before turning on the Hot Disk to achieve thermal equilibrium. The power was 200 mW and was applied for a very short period of time of around one second. Each experiment was repeated three times (with 30 minutes waiting time to achieve equilibrium); however, the extracted temperature trend was almost the same at each trial.

2.2 Numerical methods

In this study, the heat conduction equation was numerically solved in 2D and 3D forms using ADI and Douglas-Gunn method respectively. In both cases the numerical code was written in C++.

2.2.1 2D heat equation and ADI method

The heat conduction equation (Eq. 1) is directly derived from writing the energy balance equation for a small volume control.

$$\rho c_p \frac{\partial T}{\partial t} = \nabla \cdot (k \nabla T) \quad (1)$$

In this study, this equation was solved in a two-dimensional cylindrical form for constant thermal conductivity (chapter 5). This can be written as:

$$\rho c_p \frac{\partial T}{\partial t} = \frac{k}{r} \frac{\partial}{\partial r} \left(r \frac{\partial T}{\partial r} \right) + k \frac{\partial^2 T}{\partial x^2} \quad (2)$$

After discretizing this equation using the finite difference method, ADI technique was used to solve Eq. 2 numerically [76]. Each time step is divided into two sub-steps. In the first sub-step, the temperature is solved implicitly in the axial direction and explicitly in the radial direction (Eq. 3). In the second sub-step, the solution is implicit at radial direction and explicit at axial direction (Eq. 4).

$$\rho c_p \frac{T_{ij}^* - T_{ij}^n}{\Delta t / 2} = k \left[\frac{T_{i+1j}^n - 2T_{ij}^n + T_{i-1j}^n}{(\Delta r)^2} + \frac{1}{r} \frac{T_{i+1j}^n - T_{i-1j}^n}{2\Delta r} \right] + k \frac{T_{ij+1}^* - 2T_{ij}^* + T_{ij-1}^*}{(\Delta x)^2} \quad (3)$$

$$\rho c_p \frac{T_{ij}^{n+1} - T_{ij}^*}{\Delta t / 2} = k \left[\frac{T_{i+1j}^{n+1} - 2T_{ij}^{n+1} + T_{i-1j}^{n+1}}{(\Delta r)^2} + \frac{1}{r} \frac{T_{i+1j}^{n+1} - T_{i-1j}^{n+1}}{2\Delta r} \right] + k \frac{T_{ij+1}^* - 2T_{ij}^* + T_{ij-1}^*}{(\Delta x)^2} \quad (4)$$

By writing these equations for each node, a tridiagonal system will be generated. If the number of grids at axial and radial directions are N_x and N_r , at each time step, there will be N_r tridiagonal matrices for the first sub-step and N_x matrices for the second sub-step. Each matrix is in the form presented in Eq. 5 and will be solved using Thomas algorithm.

$$\begin{aligned}
T_{ijk}^{n+2/3} - T_{ijk}^n &= \frac{\kappa_{ijk}^x \delta_x^2}{2} \left(T_{i+1/3}^{n+1/3} + T_{ijk}^n \right) + \frac{\kappa_{ijk}^y \delta_y^2}{2} \left(T_{i+2/3}^{n+2/3} + T_{ijk}^n \right) + \\
&\kappa_{ijk}^z \delta_z^2 T_{ijk}^n + \frac{\kappa_{i+1jk}^x - \kappa_{i-1jk}^x}{8} \left(T_{i+1/3}^{n+1/3} + T_{i+1jk}^n - T_{i-1/3}^{n+1/3} - T_{i-1jk}^n \right) + \\
&\frac{\kappa_{ij+1k}^y - \kappa_{ij-1k}^y}{8} \left(T_{ij+2/3}^{n+2/3} + T_{ij+1k}^n - T_{ij-2/3}^{n+2/3} - T_{ij-1k}^n \right) + \frac{\kappa_{ijk+1}^z - \kappa_{ijk-1}^z}{4} \left(T_{ijk+1}^n - T_{ijk-1}^n \right).
\end{aligned} \tag{8}$$

$$\begin{aligned}
T_{ijk}^{n+1} - T_{ijk}^n &= \frac{\kappa_{ijk}^x \delta_x^2}{2} \left(T_{i+1/3}^{n+1/3} + T_{ijk}^n \right) + \frac{\kappa_{ijk}^y \delta_y^2}{2} \left(T_{i+2/3}^{n+2/3} + T_{ijk}^n \right) + \\
&\frac{\kappa_{ijk}^z \delta_z^2}{2} \left(T_{ijk}^{n+1} + T_{ijk}^n \right) + \frac{\kappa_{i+1jk}^x - \kappa_{i-1jk}^x}{8} \left(T_{i+1/3}^{n+1/3} + T_{i+1jk}^n - T_{i-1/3}^{n+1/3} - T_{i-1jk}^n \right) + \\
&\frac{\kappa_{ij+1k}^y - \kappa_{ij-1k}^y}{8} \left(T_{ij+2/3}^{n+2/3} + T_{ij+1k}^n - T_{ij-2/3}^{n+2/3} - T_{ij-1k}^n \right) + \\
&\frac{\kappa_{ijk+1}^z - \kappa_{ijk-1}^z}{8} \left(T_{ijk+1}^{n+1} + T_{ijk+1}^n - T_{ijk-1}^{n+1} - T_{ijk-1}^n \right).
\end{aligned} \tag{9}$$

$$\delta_x^2 T_{ijk}^n = T_{i+1jk}^n - 2T_{ijk}^n + T_{i-1jk}^n \tag{10}$$

$$\kappa_{ijk}^x = \frac{k_{ijk}^n \Delta t}{\rho c_p \Delta x^2} \tag{11}$$

At each sub-step the whole domain is scanned in two spatial directions, and tridiagonal matrices are written and solved in the other direction. For instance, tridiagonal matrices for the first sub-step at each scanned point (j,k) are written similar to Eq. 12 and solved at x direction (for varying i).

2.4 Validity and reliability of the measurements

All the data (diameter, depth and width of the grooves, roughness or porosity) are collected from at least 10-20 different spots on the surface and mean values and standard deviations are calculated.

2.5 Assumptions

1. Temperature and humidity of the lab are almost constant while running the electrospinning machine.
2. Laser beam profile does not change considerably at each run.
3. In computer simulation, thermal properties of molten Titanium are assumed to be constant.
4. Computer simulations will only be carried for solid or liquid Titanium and Navier-Stokes equations will not be solved for the air.

Chapter 3

Thermal modeling of laser processing on a metallic surface¹

In this chapter, a 3D model is presented to solve the heat conduction equation which considers phase change and temperature-dependent thermal properties. The main purpose of this model is to provide a fast and yet accurate model that can be used to find the laser parameters for any desired application and texturing pattern. It can provide us with useful information about ablation depth and temperature trend at any point, which can be manipulated to choose the laser parameters. We believe the running time shouldn't exceed a couple of minutes for estimation of ablation depth. Otherwise, there is almost no point in using the model, because laser processing is a fast method and the actual value can be

¹ The results presented in this chapter were published in *AIP Advances* Naghshine, B. B., & Kiani, A. (2017). 3D transient model to predict temperature and ablated areas during laser processing of metallic surfaces. *AIP Advances*, 7(2), 025007.

measured in a shorter amount of time. The 3D equation is solved in order to have both the groove profile and temperature distribution at any section and also be able to define scanning speed as an important laser parameter in the code. On the other hand, Navier-Stokes equations are not solved in this model, to reduce the computation time and make the model as fast as possible. This opens up new possibilities such as optimization. For instance, the laser parameters can be optimized for the largest or smallest heat affected zone (HAZ) and thus higher or lower level of oxidation.

3.1 Temperature calculations

In the present model, heat conduction equation (Eq. 13) is solved in Cartesian coordinates for a thin metallic sheet. The domain is discretized into interactive cubic cells. The cells can shrink in z direction during the ablation process. Thermal conductivity, specific heat and absorption are considered as functions of temperature. These properties are updated at each time step in the numerical algorithm, which makes them a function of space (Eq. 14). Thermal properties are plotted as a function of temperature for titanium (Figure 3). Furthermore, the properties are considered to be constant after the melting point due to lack of data.

$$\rho c_p \frac{\partial T}{\partial t} = k \left(\frac{\partial^2 T}{\partial x^2} + \frac{\partial^2 T}{\partial y^2} + \frac{\partial^2 T}{\partial z^2} \right) + \frac{\partial k}{\partial x} \frac{\partial T}{\partial x} + \frac{\partial k}{\partial y} \frac{\partial T}{\partial y} + \frac{\partial k}{\partial z} \frac{\partial T}{\partial z} \quad (13)$$

$$k = k(T) \xrightarrow{\text{for each time step}} k = k(x, y, z) \quad (14)$$

Eq. 13 is solved using the method described in section 2.2.2.

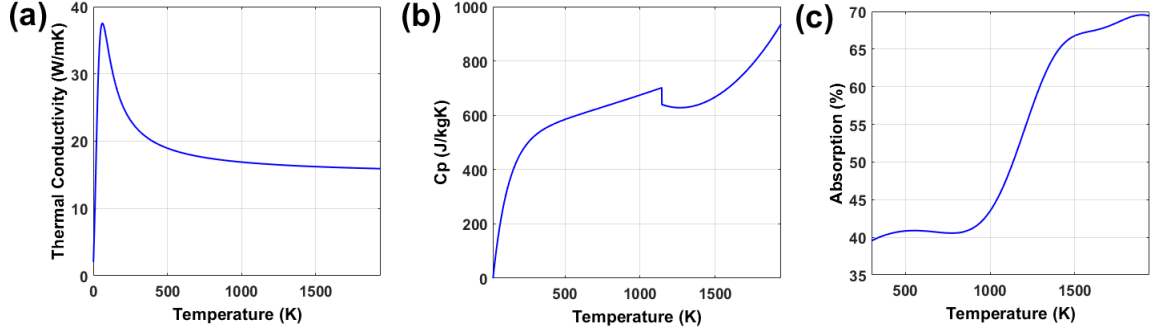


Figure 3 – (a)Thermal conductivity [78], (b)specific heat [78] and (c)Absorption [79] as a function of temperature

3.2 Boundary conditions

The boundary conditions at the surface ($k=0$) are convection, radiation and laser irradiation (Eq. 15). A Gaussian profile is considered for the laser beam and the center of the beam is moving on the surface with scanning speed. For the back side ($k=N_z$), insulation boundary conditions are written and for the other sides, boundary conditions are convection, radiation and laser pulse.

$$-k \frac{\partial T}{\partial z} = h(T_{air} - T_{surface}) + \sigma \varepsilon (T_{air}^4 - T_{surface}^4) + \alpha q_{laser}'' \quad (15)$$

3.3 Phase change and ablation

Phase change and ablation are considered only in the last sub-step (z direction). Also, all the calculated temperatures that are above boiling point at the first and second sub-steps will be set at the boiling temperature.

In the last sub-step, if the calculated temperature of one or more cells at each i and j is larger than boiling temperature, the ablative energy will be calculated using Eq. 16, where N is the number of cells with a temperature higher than boiling point.

$$\begin{aligned}
\text{Ablative Energy} &= \sum_{k=1}^N \rho \Delta x \Delta y \Delta z c_p (T_{ijk}^{n+1} - T_{boiling}) / (\Delta x \Delta y \Delta t) \\
&= \sum_{k=1}^N \rho c_p \Delta z (T_{ijk}^{n+1} - T_{boiling}) / \Delta t
\end{aligned} \tag{16}$$

If this energy was sufficient to ablate the first cell on the surface, then that cell is taken out and its boundary conditions are transferred to the next cell and boundary conditions are updated for all the neighboring cells. Also, q''_{laser} is reduced by the amount of energy needed to vaporize that cell which is $\rho \Delta z L_v / \Delta t$. Otherwise, if the energy is not high enough to ablate the top cell completely, the Δz is reduced by $\text{Ablative Energy} \times \Delta t / (\rho L_v)$ and q''_{laser} is decreased by ablative energy. Then the third sub-step is repeated until convergence, when all the temperatures are below boiling point or the ablative energy is zero.

The phase of each cell can be solid, liquid or a combination of both. If the temperature of a cell is calculated to be greater than its melting point and the cell is completely or partially in solid phase, or the calculated temperature was less than melting point and it was fully or partially in liquid phase, the laser pulse flux will be modified using a similar algorithm considering the latent heat of fusion (L_f).

The flowchart of the computational code is shown in Figure 4. As can be seen, whenever the temperature is passing the melting point or boiling point, the phase change algorithms are called. Figure 5 shows the phase change flowchart for evaporation. Similar algorithms are considered for melting and solidification.

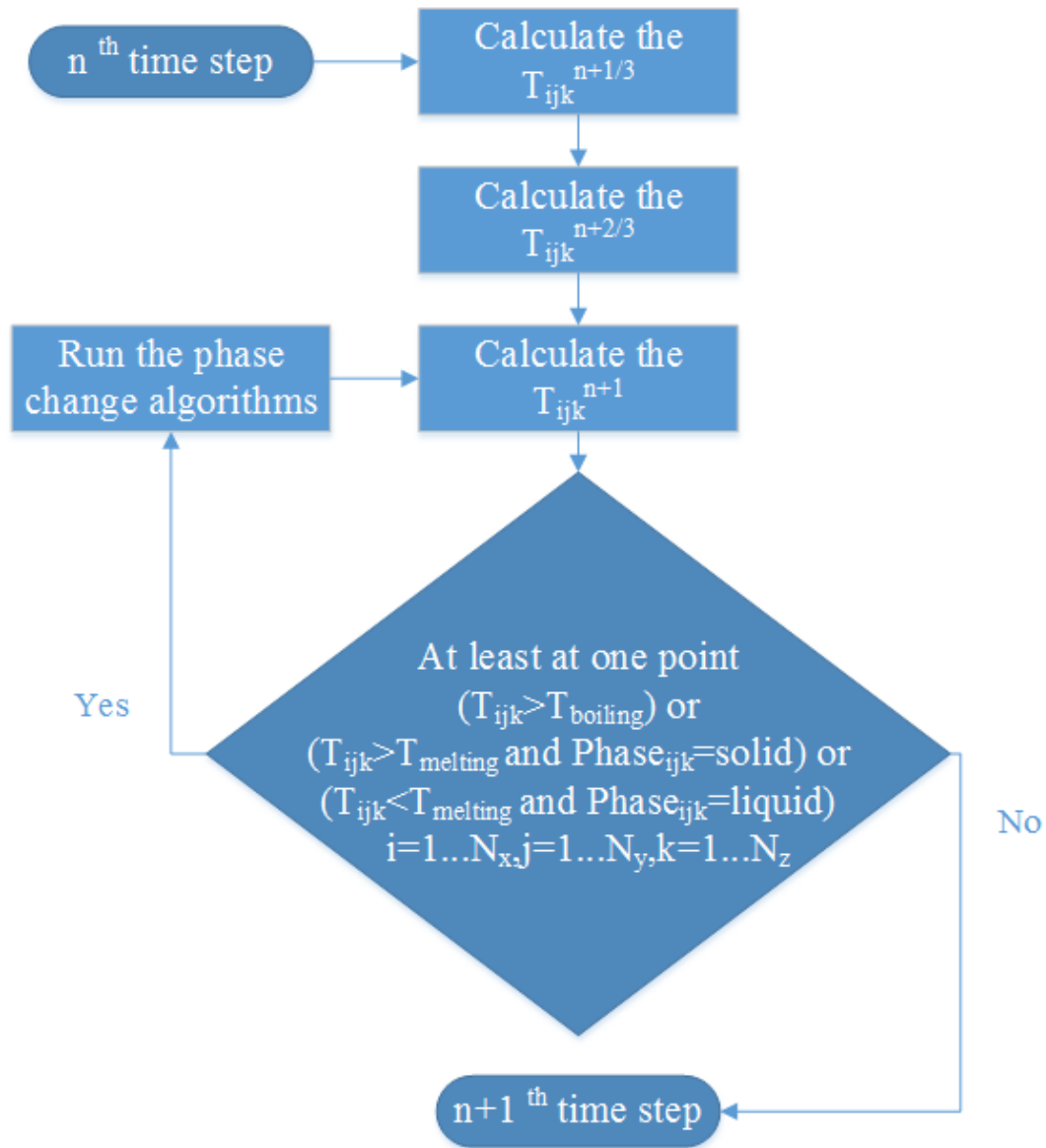


Figure 4 – The computational flowchart at each time step

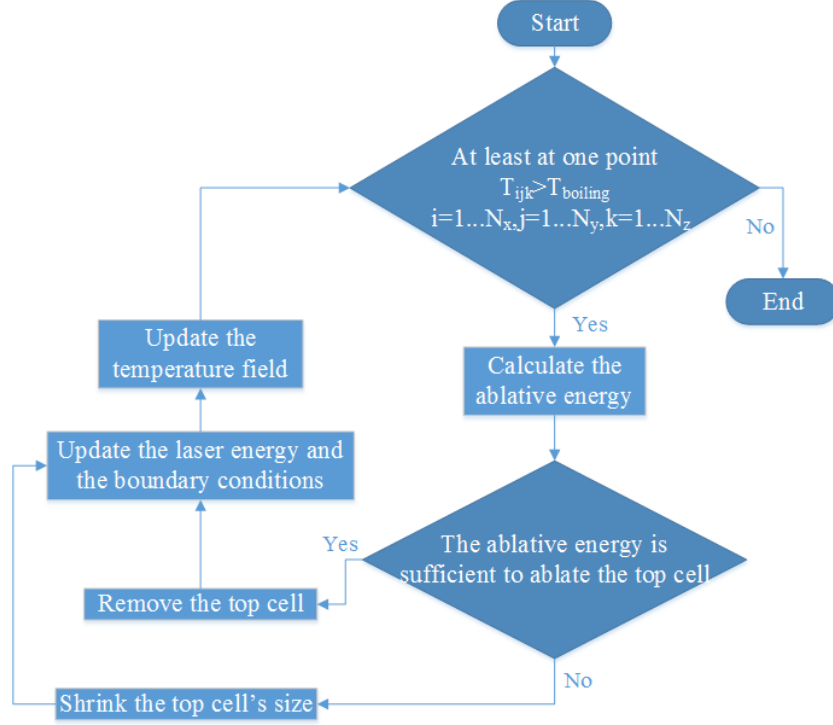


Figure 5 – The flowchart of evaporation

Enthalpy-based method also offers a different approach for phase change modeling [80].

In this method, Eq. 13 is rewritten as:

$$\frac{\partial(\rho H)}{\partial t} = k \left(\frac{\partial^2 T}{\partial x^2} + \frac{\partial^2 T}{\partial y^2} + \frac{\partial^2 T}{\partial z^2} \right) + \frac{\partial k}{\partial x} \frac{\partial T}{\partial x} + \frac{\partial k}{\partial y} \frac{\partial T}{\partial y} + \frac{\partial k}{\partial z} \frac{\partial T}{\partial z} \quad (17)$$

Where $H = c_p + \Delta H$ and ΔH is defined in Eq. 18.

$$\Delta H = \begin{cases} L_f & , T > T_l \\ f_l L_f & , T_s \leq T \leq T_l \\ 0 & , T < T_s \end{cases} \quad (18)$$

T_l and T_s are the liquidus and solidus temperatures respectively and f_l is the liquid fraction.

3.4 Plasma shielding and power loss

During laser processing plasma will be formed in the material's plume, which can absorb the energy of laser beam. This cannot be neglected in the model, because the plasma plume may have a large optical thickness and cause a considerable decrease in the laser intensity that reaches the surface of the material. For instance, plasma absorption in helium is 70% at a power density of 10^9 W/cm² and pulse duration of 30 ns [81].

Based on experimental studies, plasma absorption is a function of power density of laser pulses and it will increase as power density goes up [82]. A simple model for plasma absorption has been used in previous works [83, 84]. Plasma absorption can be written as Eq. 19 based on this model:

$$\alpha_{plasma} = 1 - \exp(-\Lambda(t)) \quad (19)$$

Where $\Lambda(t)$ is optical thickness of the plasma and it can be estimated as Eq. 20:

$$\Lambda(t) = ah_{ablation}(t) + bE_a(t) \quad (20)$$

E_a is the energy absorbed by the plasma, $h_{ablation}$ is the ablation depth and a and b are calculated based on experimental results.

In this study, a new method is proposed to predict the plasma shielding effect without solving a separate differential equation for plasma. This method is inspired by Eq. 19 and 18. Plasma absorption is assumed to be constant over time (steady state) and since E_a and $h_{ablation}$ are both a function of laser pulse power, a linear correlation between optical thickness and pulse power is assumed. Also, a limit is introduced for plasma absorption, since it can never absorb the whole energy. The resulting formula can be seen in Eq. 21:

$$\alpha_{plasma} = \alpha_{max} (1 - \exp(-c\psi)) \quad (21)$$

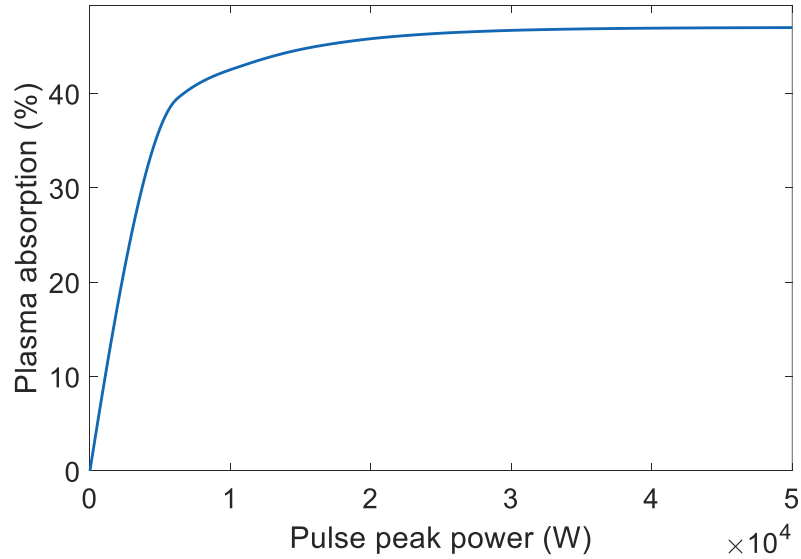


Figure 6 – Plasma absorption for laser processing of titanium sheets used in this study

α_{max} is the maximum absorption that happens at the highest pulse power. ψ is non-dimensionalized pulse power, which is calculated by dividing the pulse peak power to the highest possible peak power that can be generated by the laser beam. α_{max} and c are determined by experimental results. The plasma absorption as a function of the peak power of the laser pulses is shown in Figure 6 for titanium. On the other hand, a 10% power loss was considered for the galvo scanner based on our measurements.

3.5 Numerical and experimental results for laser processing of a titanium sheet

Ablation depth was measured using the 3D optical profiler at 10-15 points for eleven different sets of laser parameters and maximum, minimum and average values were calculated. The same values were calculated from model's results along the line (at the

center of the line) and the numbers were compared to each other. As Figure 7 shows, there is a strong correlation between numerical and experimental results ($r=0.96$ and $p<10^{-5}$ for average depth and $r=0.92$ and $p<10^{-4}$ for maximum depth).

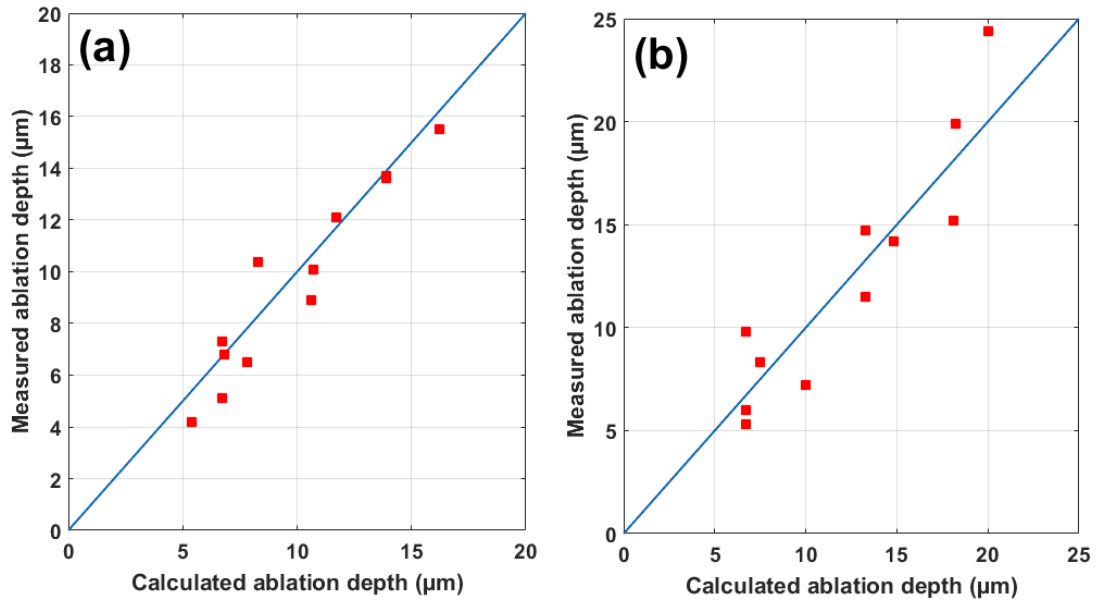


Figure 7 – (a) Average calculated ablation depth vs. average measured depth (b) Maximum calculated ablation depth vs. maximum observed depth

Figure 8 and 9 show that the model can successfully predict the effect of changing each laser parameter on the ablation depth with a good precision. Figure 10 shows how ablation depth is increasing as the surface is irradiated at different frequencies and scanning speeds. When there are 300 pulses per millimeter (power=10 W, frequency=60 kHz, pulse duration=35 ns, scanning speed=200 mm/s at Figure 10a) four consecutive pulses caused ablation. However, the ablation was mainly caused by only two pulses. It can be compared to another case (power=10 W, frequency=50 kHz, pulse duration=29 ns, scanning speed=700 mm/s at Figure 10b) where the number of pulses was as low as 70 pulses per

millimeter and the surface was processed only by one pulse at each point. As can be seen, the ablation rate is almost constant during a single pulse and is zero between pulses.

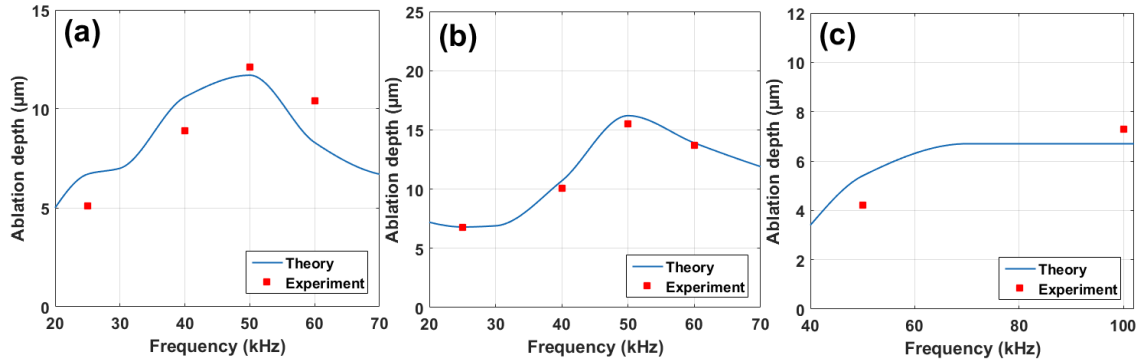


Figure 8 – Ablation depth vs. frequency at (a) power=5 W, scanning speed=200 mm/s (b) power=10 W, scanning speed=200 mm/s (c) power=10 W, scanning speed=700 mm/s

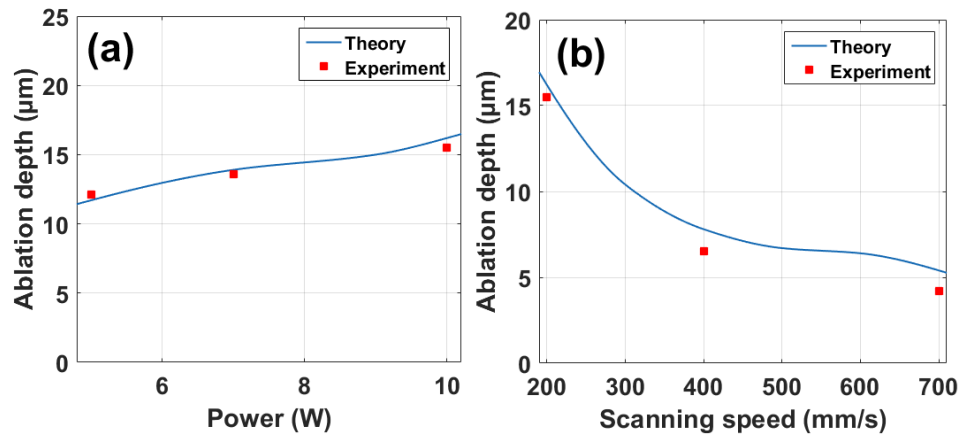


Figure 9 – (a) Ablation depth vs. power at frequency=50 kHz, scanning speed=200 mm/s (b) Ablation depth vs. scanning speed at power=10 W, frequency=50 kHz

Maximum surface temperature was recorded during the process and the results are shown in Figure 11 at cross section for three different frequencies. Since the pulse energy is higher at low frequencies, we can see that a larger area was affected by laser pulse as the frequency is decreasing. However, because the thermal conductivity of titanium is

relatively low and the process happens in a very short time, we cannot see a significant difference.

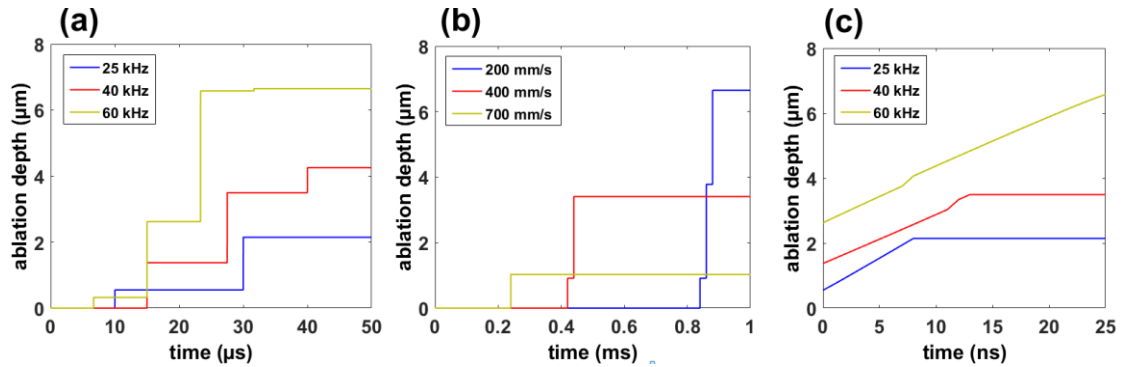


Figure 10 – (a) Variations of ablation depth of a single point during the process for different frequencies at power=10 W, scanning speed=200 mm/s (b) Variations of ablation depth of a single point during the process for different scanning speeds at power=10 W, frequency=50 kHz (c) Ablation depth during a single pulse at power=10 W, scanning speed=200 mm/s

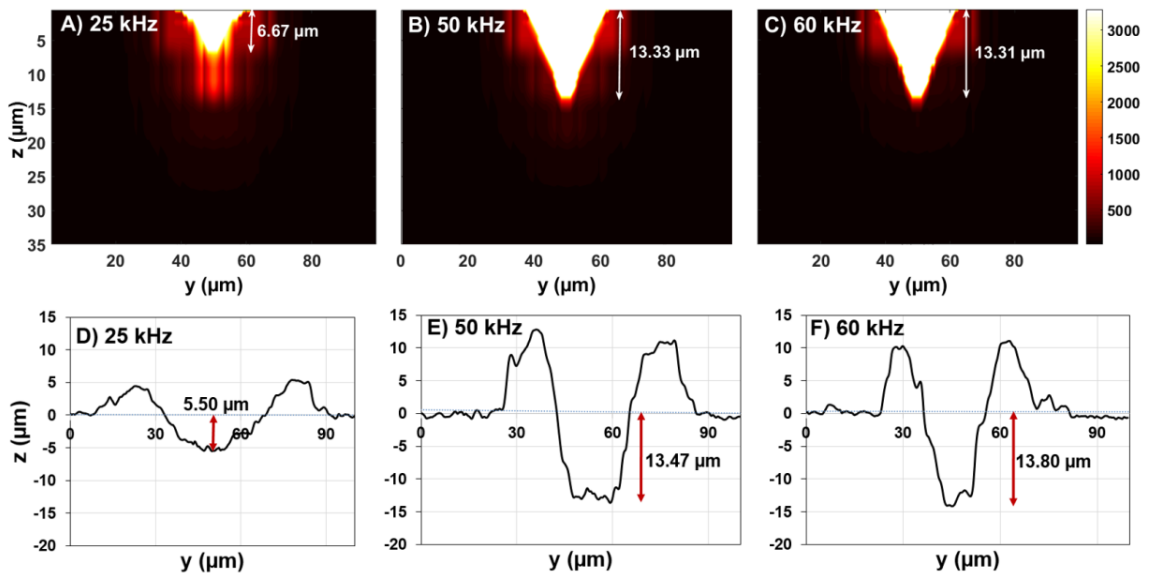


Figure 11 – Cross section of the ablated zone and maximum temperature at power=5 W, scanning speed=200 mm/s and (a) frequency=25 kHz, pulse duration=22 ns (b) frequency=50 kHz, pulse duration=36 ns (c) frequency=60 kHz, pulse duration=42 ns and measured groove profile at the same power and scanning speed and (d) frequency=25 kHz (e) frequency=50 kHz (f) frequency=60 kHz.

Maximum surface temperature is shown at Figure 12. The surface temperature was almost the same at different laser parameters and as can be seen, the surface temperature was

increased only around 25 μm away from the edge of the groove and the rest of the surface was not affected by the laser beam. This can be confirmed by experimental results. We can see a color change around 28 μm away from the edge of grooves (Figure 12), which shows this area was affected by the laser. We can see a slightly larger affected zone in experimental results because the surface was also affected by the plasma inside the material plume, which was not modeled in this study. This distance is almost constant in all cases in both numerical and experimental results. Moreover, it can be seen that, the width of grooves is smaller in numerical results (Figure 11). This can be explained by actual chaotic beam profile, which is different from the Gaussian profile considered in the model. The other reason can be the flow of molten material at the surface. On the other hand, thermal properties of molten titanium are unknown and are assumed to be constant in this model, which can affect the prediction of the ablation zone.

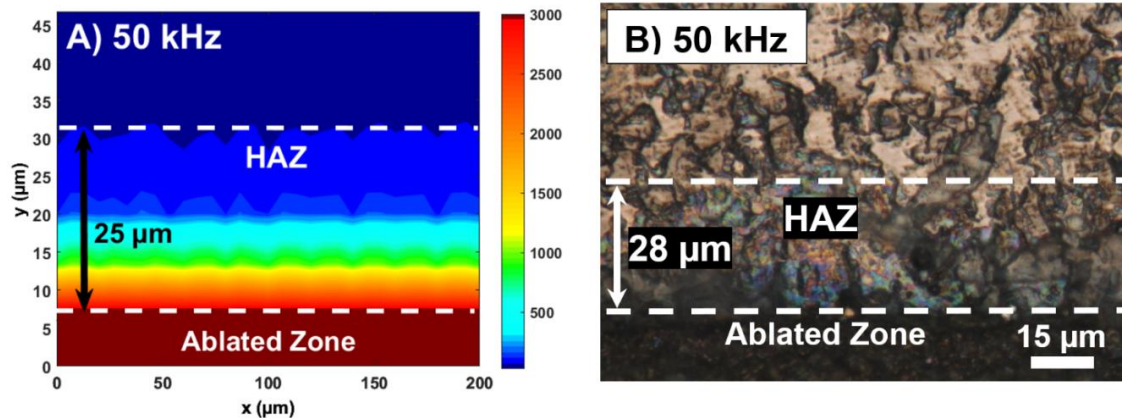


Figure 12 – (a) Maximum surface temperature at power=5 W, frequency=50 kHz and scanning speed=200 mm/s (b) Color change on the surface for the same laser parameters

Chapter 4

Laser processing of a thin film coated surface²

4.1 Materials and sample preparation

The numerical model introduced in chapter 3 is modified for a thin film coated structure in this chapter. A pure silicon sheet, a silicon sheet coated by an aluminum layer with the thickness of 1 μm and a silicon sheet coated by a very thin gold layer with a thickness around 100 nm were processed by laser at different powers and repetition rates. The thin films were deposited using PVD technique on the surface of the samples. The samples were purchased with thin film coating and were directly used for laser processing.

² The results presented in this chapter were submitted to Beilstein Journal of Nanotechnology.

The plasma absorption was estimated using the method explained in section 3.4. As three different materials were studied, three sets of plasma absorption coefficients were calculated from experimental results. The plasma absorption functions are plotted in the following pages for each material. All the numerical analysis and experiments in this chapter were carried out on single pulses. The laser pulses cannot be easily isolated due to limitations of the equipment. To isolate the single pulses, the scanning speed was set at its maximum value (around 1000 mm/s). In this case, if the repetition rate is relatively low, the distance between the location of two consecutive pulses on the surface will be long enough to remove the effect of the neighboring pulses. Therefore, a dotted pattern will be created on the surface and each dot can be considered as the result of laser processing by a single pulse on the surface (Figure 13).

The samples were processed with different laser parameters (power and frequency) and the hole profiles were captured using the 3D optical profiler from at least ten different points.

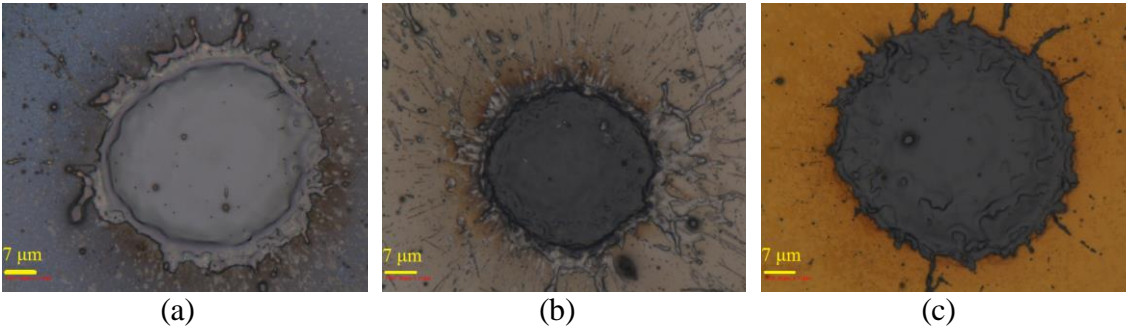


Figure 13 – (a) Isolated pulse on the surface of silicon, (b) Isolated pulse on the surface of aluminum, (c) Isolated pulse on the surface of gold

4.2 Laser processing of bare silicon sheets

Physical and optical properties of silicon are plotted as a function of temperature in Figure 14. The properties at higher temperatures, where the values are unknown, were assumed to be constant and equal to the closest known point. The melting and boiling points of silicon are 1414 °C and 3538 °C respectively and the heats of fusion and vaporization are 1788 and 13637 kJ/kg [85].

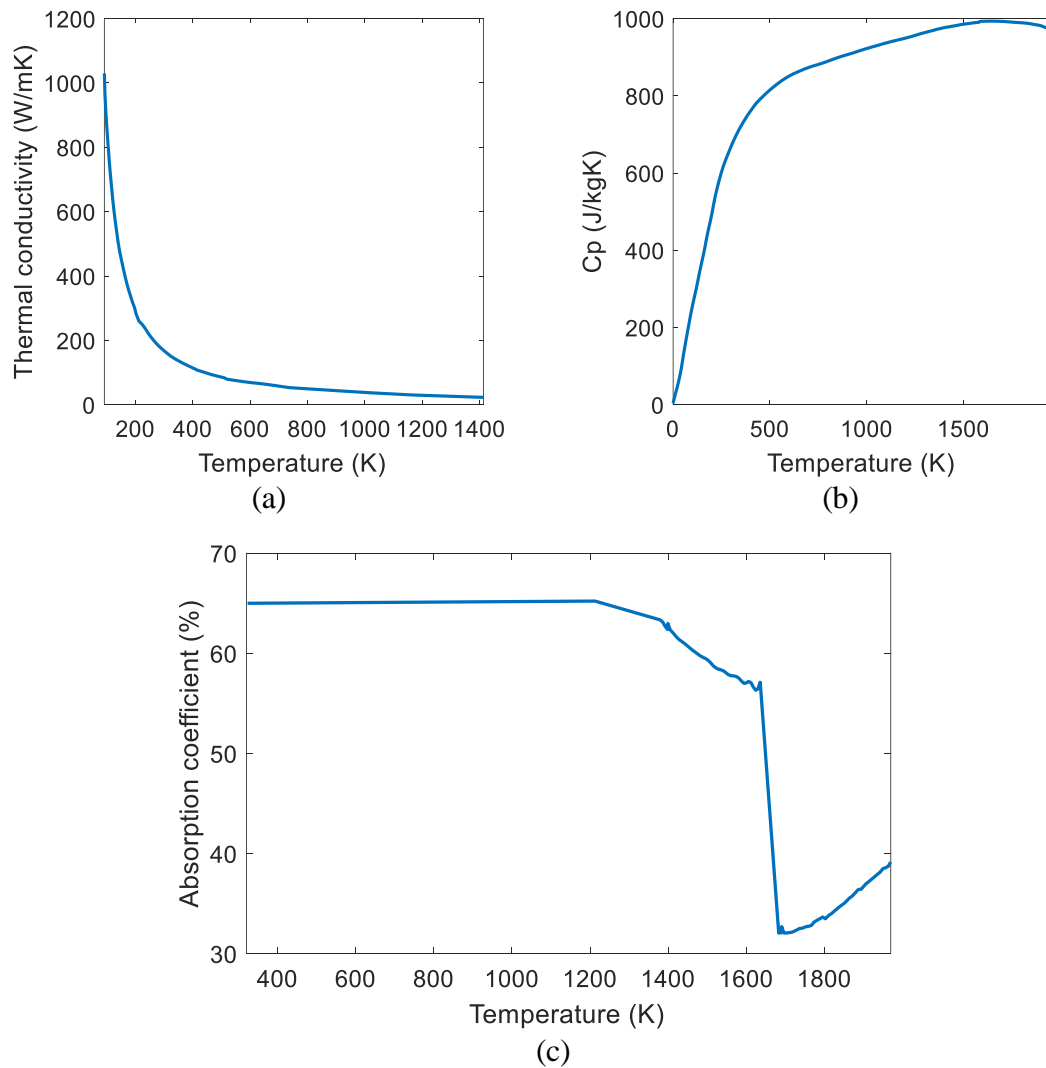


Figure 14 – (a) Thermal conductivity of silicon [86], (b) specific heat of silicon [86], (c) absorbance of silicon [87].

Figure 15 shows the plasma absorption for laser processing of uncoated silicon samples. After introducing all these functions, the numerical analysis was carried out.

The results for varying frequencies at 5 W are presented in Figure 16. As can be seen in Table 2, the numerical and experimental results are in good agreement. The holes on the surface of the specimen that was processed at 75 kHz and 5 W were very shallow and it was difficult to capture a precise profile using the 3D optical profiler. It was mainly due to the noise captured by the equipment (there were some fluctuations around 0.2-0.3 μm on the surface). However, 2D images of the sample's surface verifies the formation of these shallow holes (Figure 17). This is in agreement with the calculated depth (0.4 μm).

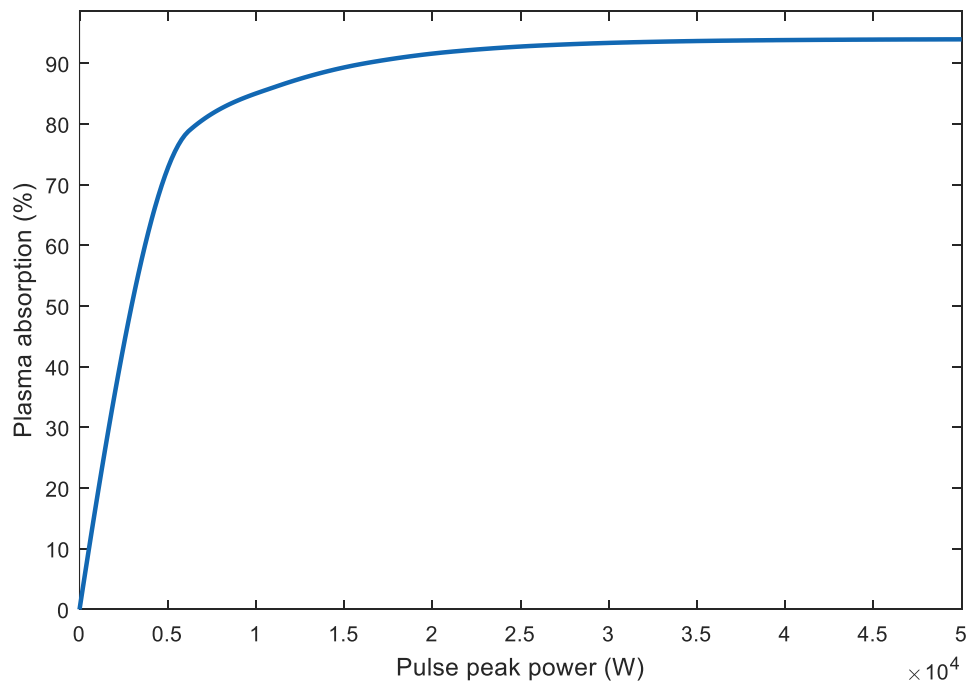


Figure 15 - Plasma absorption for laser processing of silicon sheets obtained from experimental results

Table 2 – Measured and calculated ablation depths

Power (W)	Frequency (kHz)	Averaged measured depth (μm)	Calculated depth (μm)	Accuracy (%)
5	25	1.6	1.8	87.5
5	50	1.4	1.5	92.9
5	75	-	0.4	-
10	50	2.2	2.1	95.6
15	50	1.9	1.9	100
Standard deviation		0.35	0.25	3.87

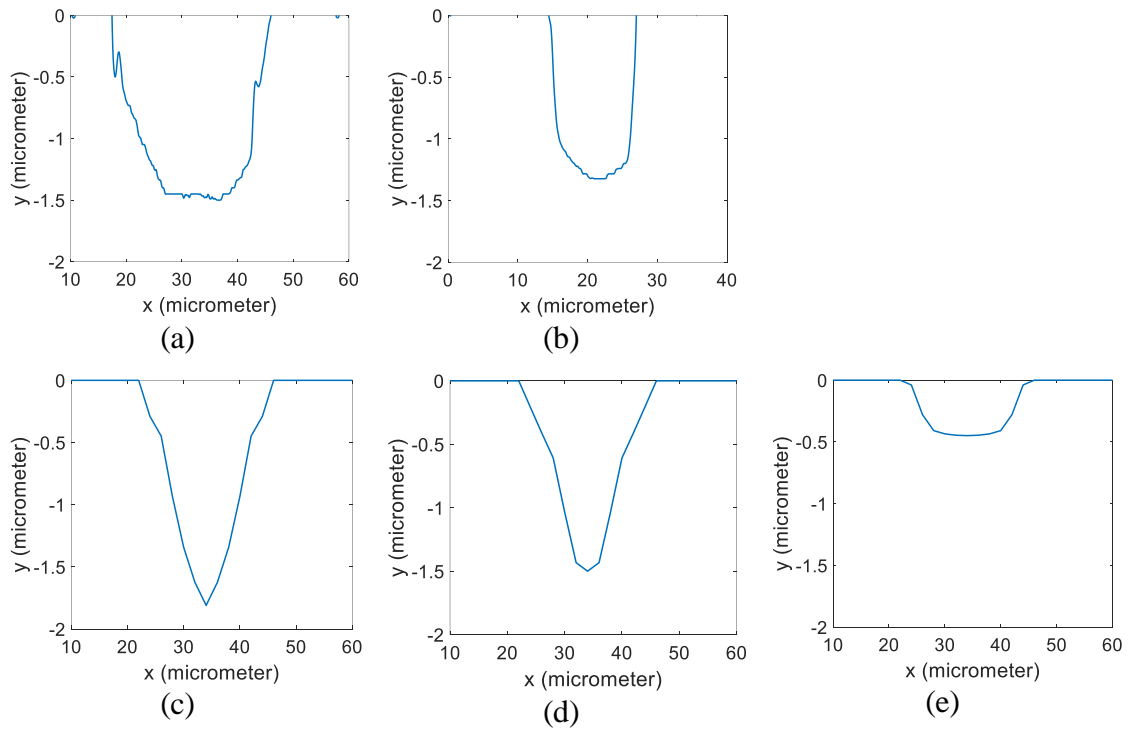


Figure 16 – (a) Measured profile at 5 W and 25 kHz, (b) measured profile at 5 W and 50 kHz, (c) calculated profile at 5 W and 25 kHz, (d) calculated profile at 5 W and 50 kHz, (e) calculated profile at 5 W and 75 kHz.

Figure 18 shows the profiles for different laser powers at the repetition rate of 50 kHz. The hole profiles were successfully calculated and are in accordance with experimental results.

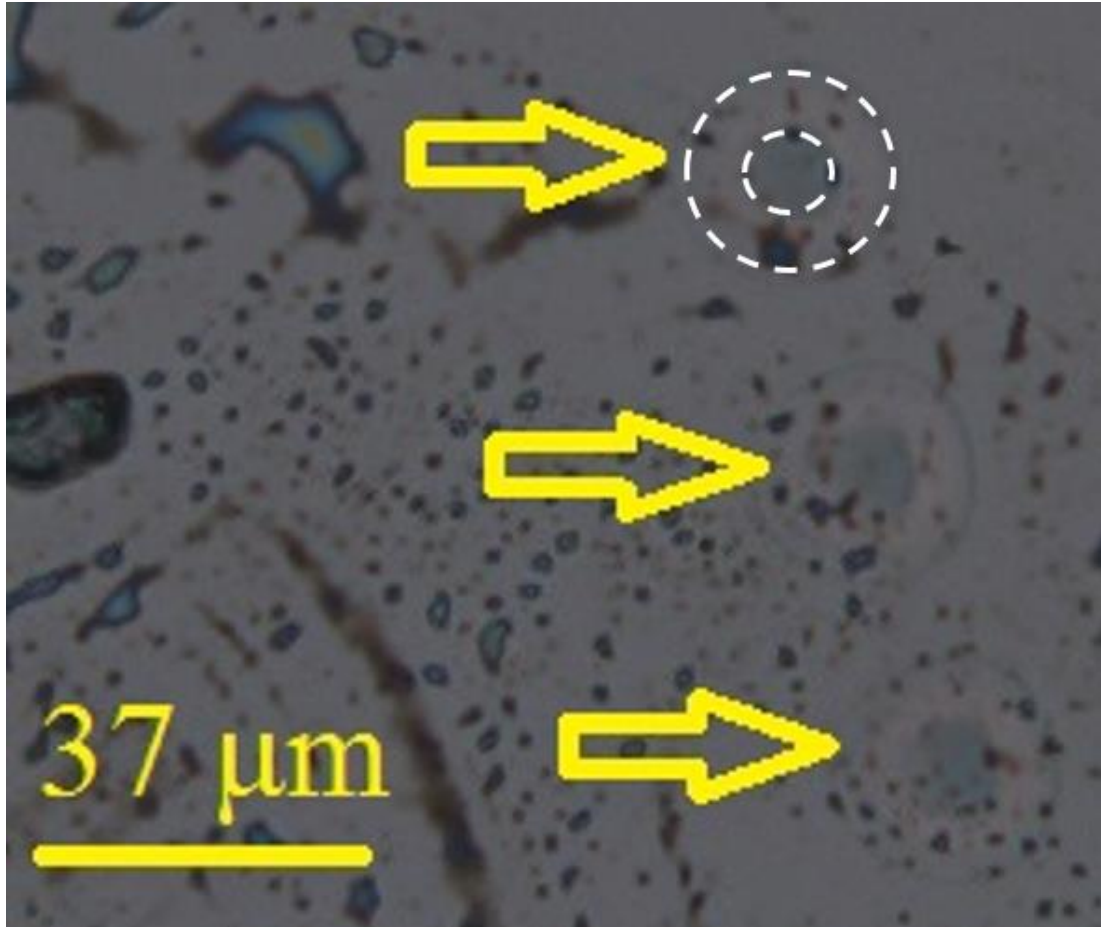


Figure 17 – Shallow holes formed on the surface of the silicon sample at 75 kHz and 5 W. The diameters of the holes at low frequencies and high powers are slightly larger in the experimental results. The laser-driven shock wave and the flow of the molten silicon can explain the smaller calculated hole diameter. Figure 19 shows the temperature contour at the end of the pulse at the surface and cross-section of the silicon sheet for the repetition rate of 25 kHz and the power of 5 W. The melting point is highlighted and it shows a molten zone was formed around the ablated area. The pressure difference caused by the shock wave can push away the molten material and make both molten and ablated zones slightly larger. At low frequencies and high powers, the peak power of the laser pulses is higher, which results in a stronger shock wave. The fluid dynamics of the molten material

is not in the scope of this study and was not considered in the model. Therefore, the predicted diameters are slightly smaller than the actual values, at high pulse energies.

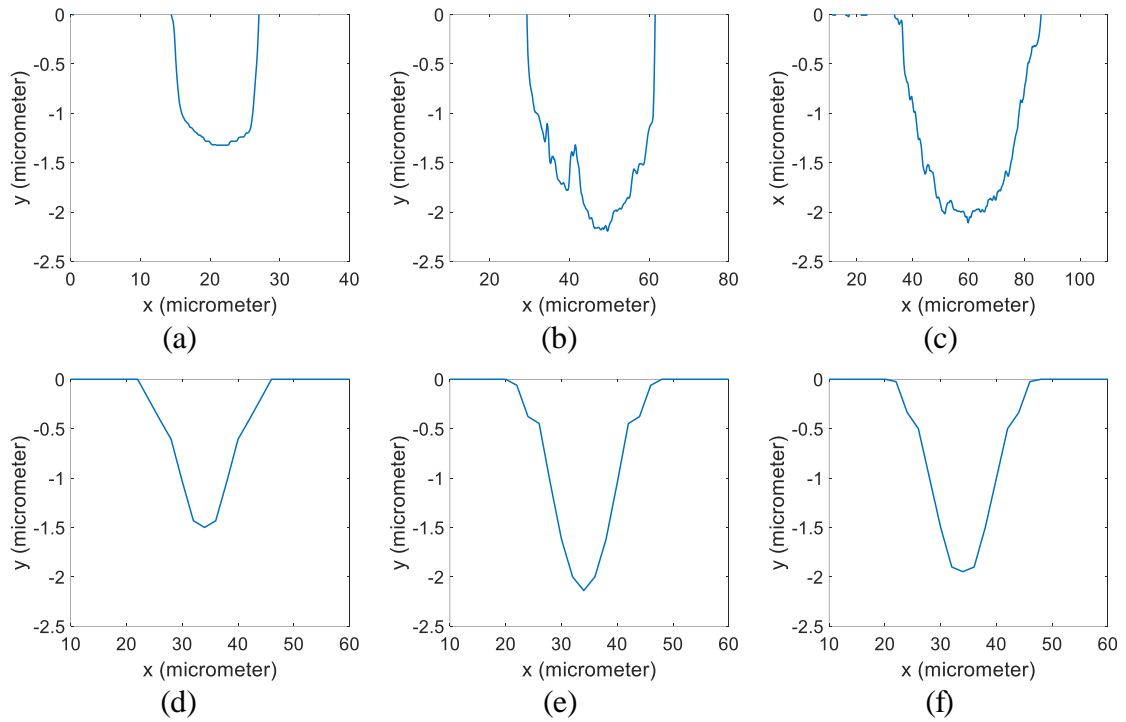


Figure 18 – (a) Measured profile at 5 W and 50 kHz, (b) measured profile at 10 W and 50 kHz, (c) measured profile at 15 W and 50 kHz, (d) calculated profile at 5 W and 50 kHz, (e) calculated profile at 10 W and 50 kHz, (f) calculated profile at 15 W and 50 kHz.

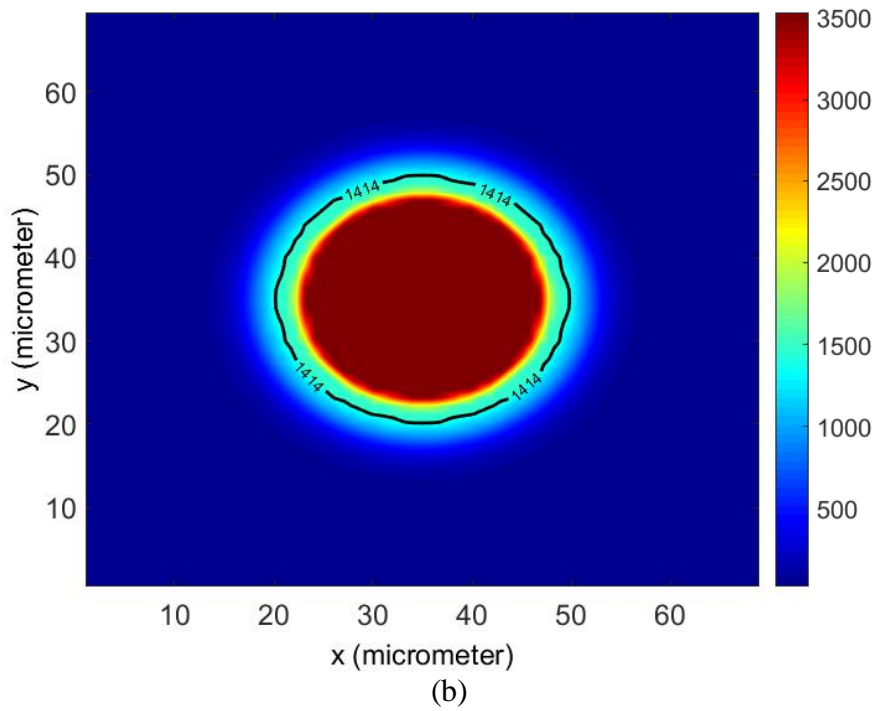
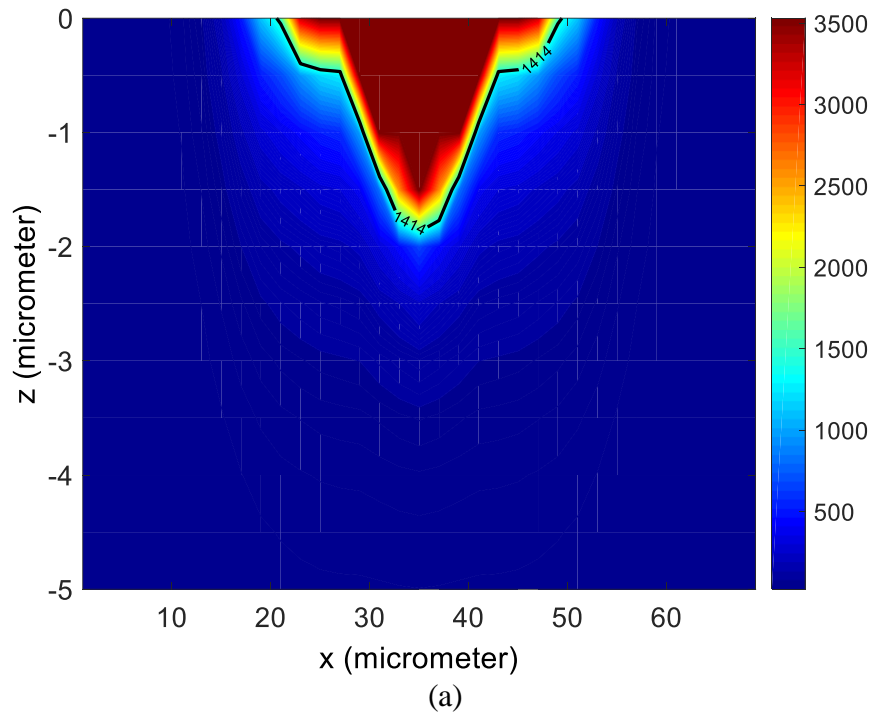


Figure 19 – Temperature contour at the end of the pulse at 25 kHz and 5 W for (a) cross-section (b) surface

4.3 Laser processing of aluminum coated silicon sheets

Physical and optical properties of aluminum are shown in Figure 20. Similarly to the previous section, the properties were assumed to be constant at unknown ranges. The melting and boiling points are 660 °C and 2470 °C respectively and aluminum has a latent heat of fusion of 397 J/kg and a latent heat of vaporization of 10800 kJ/kg [85]. Figure 21 shows the plasma absorption of aluminum, which extracted from experimental results.

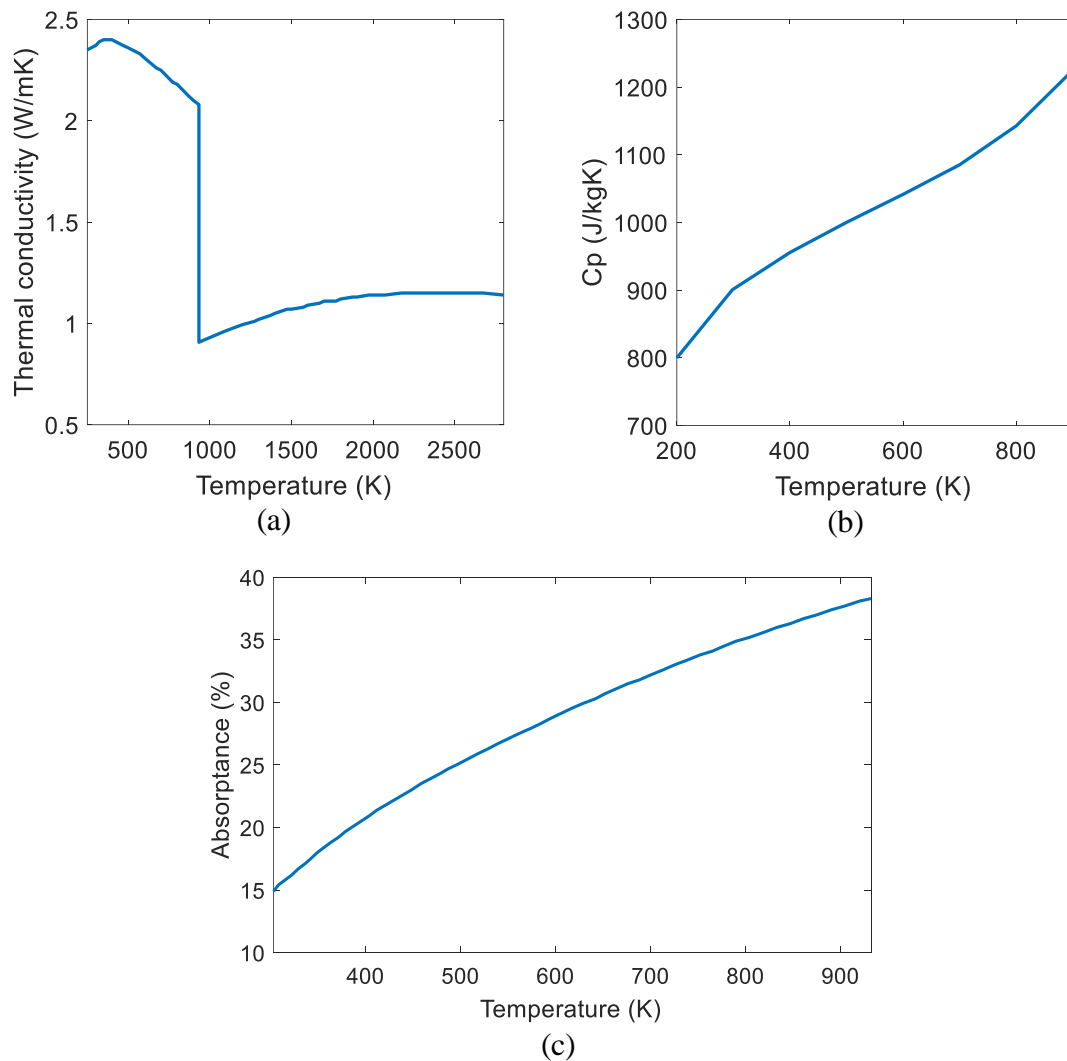


Figure 20 – (a) Thermal conductivity of aluminum [88], (b) specific heat of aluminum [88], (c) absorbance of aluminum [87].

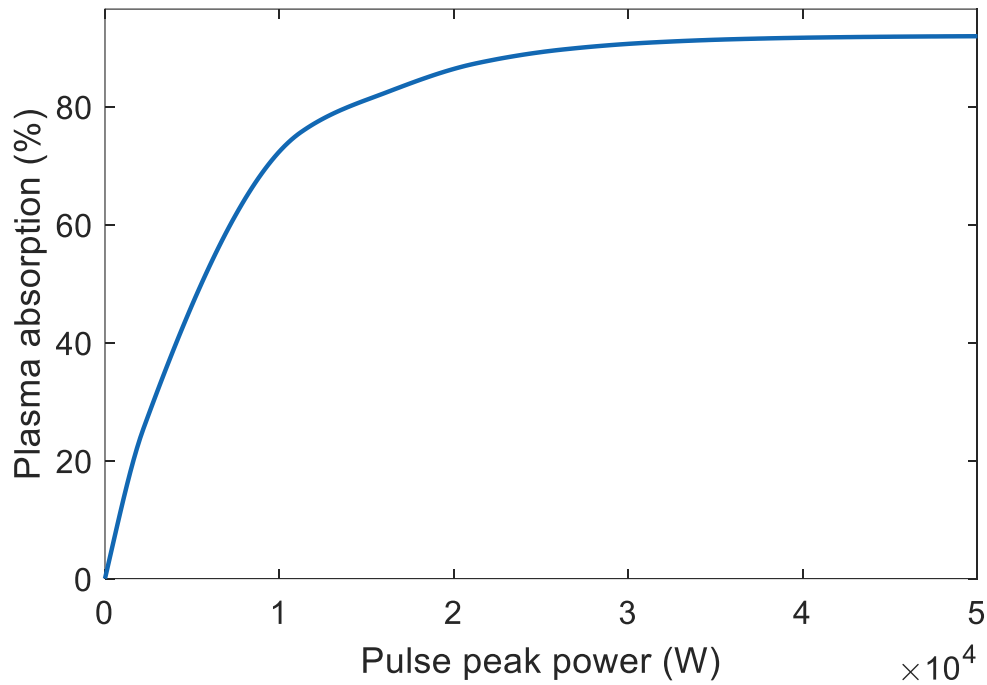


Figure 21 - Plasma absorption for laser processing of aluminum obtained from experimental results

Table 3 – Measured and calculated ablation depths

Power (W)	Frequency (kHz)	Averaged measured depth (μm)	Calculated depth (μm)	Accuracy (%)
5	25	2.1	2	95.2
5	50	2	2	100
5	75	1.5	1.6	93.3
10	50	2.4	2.5	95.8
15	50	3.7	4.1	89.2
Standard deviation		0.82	0.98	3.96

The measured and calculated ablation depths are presented in Table 3. Surface profiles at different frequencies and 5 W are shown in Figure 22. By applying a thin aluminum film on the surface, the ablation depth was significantly increased at 75 kHz compared to bare silicon samples. This can be explained by the smaller latent heat of vaporization and lower boiling temperature of aluminum, which means more material can be ablated by

consuming the same amount of energy. This can be further verified by the deeper holes at 25 and 50 kHz. The other reason is the lower plasma absorption of aluminum compared to silicon (Figure 15 and 21). Similar conclusion can be made from Figure 23 and the holes are generally deeper in aluminum coated samples. Furthermore, the predicted hole diameters are smaller than the actual values at low frequencies and high powers. This is because of the stronger shock waves which pushes the molten material away to the edges, and is not considered in the model.

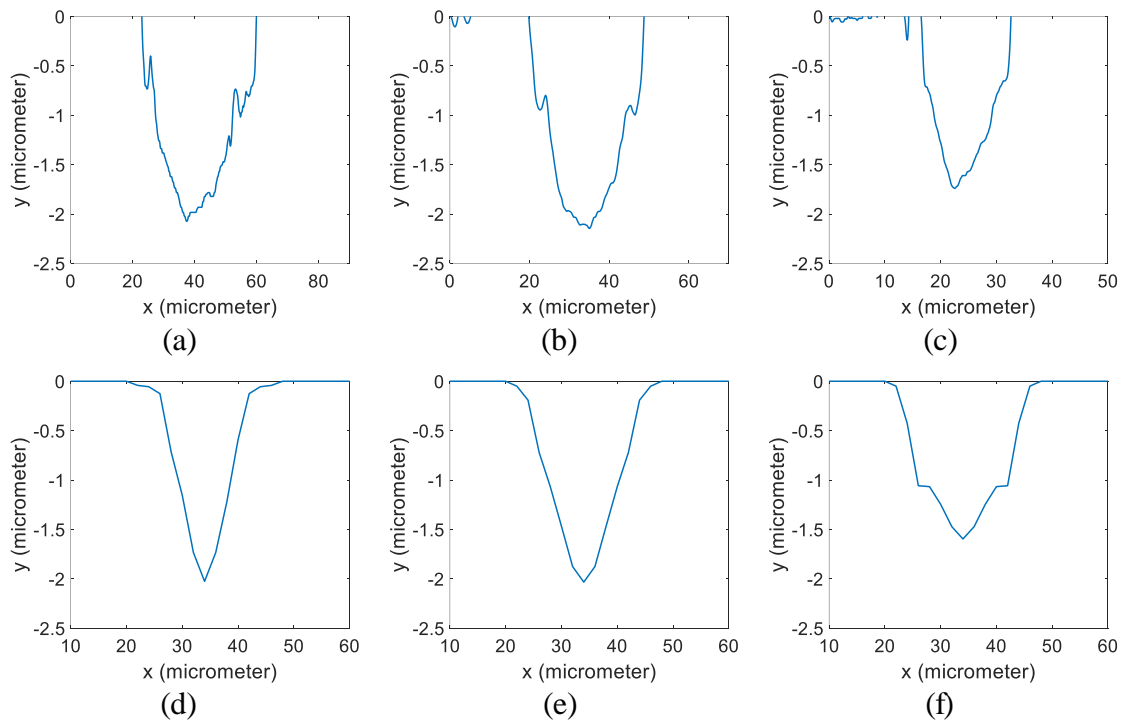


Figure 22 – (a) Measured profile at 5 W and 25 kHz, (b) measured profile at 5 W and 50 kHz, (c) measured profile at 5 W and 75 kHz, (d) calculated profile at 5 W and 25 kHz, (e) calculated profile at 5 W and 50 kHz, (f) calculated profile at 5 W and 75 kHz.

At the interface of the two layers (1 μm away from the surface), a sudden change in the diameter of the hole can be seen and it is suddenly decreasing in the silicon layer. This diameter change was apparent in the numerical results however, it's not as obvious as the

diameter changes in the experimental data. It can be explained by the results shown in Figure 24, which shows the maximum temperature at the end of the pulse on the surface and cross section of the sample at 50 kHz and 5 W. In these contours, the melting points of aluminum and silicon are highlighted (660 and 1414 °C). It can be clearly seen that, the molten zone in aluminum is slightly larger than silicon. Consequently, the molten aluminum was pushed away to the edges by the laser-driven shock wave. As mentioned in the previous section, the shock wave and fluid dynamics of the molten material are not considered in this model, which makes the predicted diameter reduction smaller, compared to the actual profile at high pulse energies.

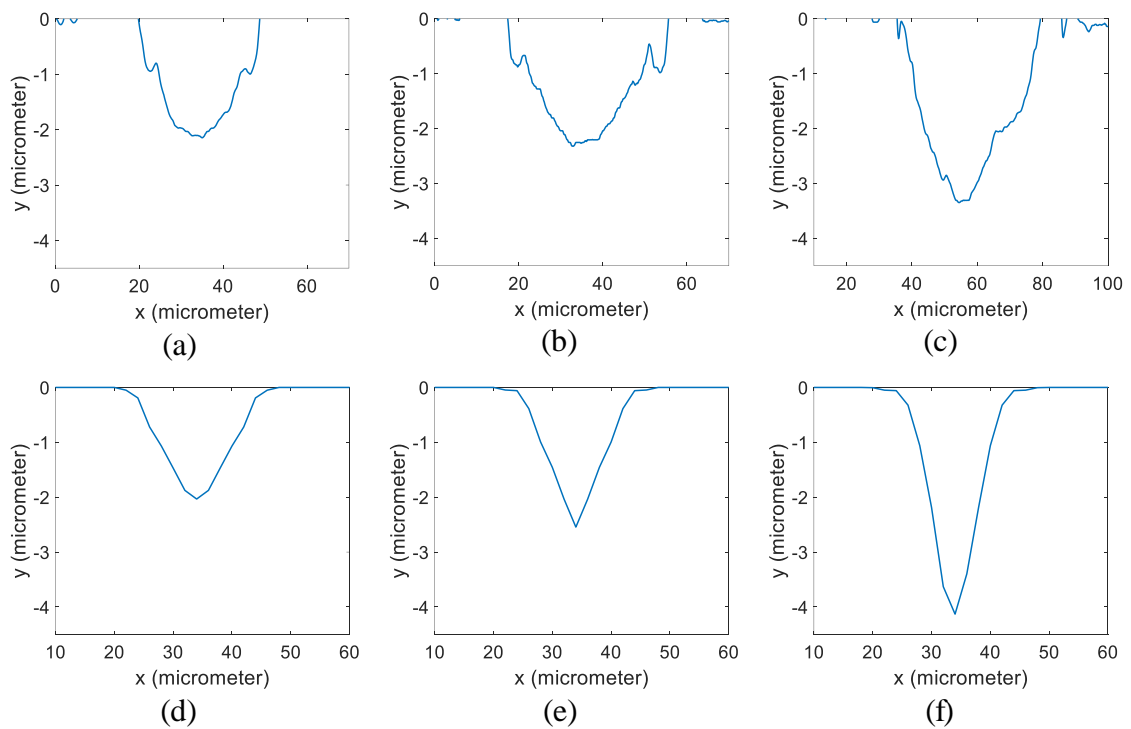


Figure 23 – (a) Measured profile at 5 W and 50 kHz, (b) measured profile at 10 W and 50 kHz, (c) measured profile at 15 W and 50 kHz, (d) calculated profile at 5 W and 50 kHz, (e) calculated profile at 10 W and 50 kHz, (f) calculated profile at 15 W and 50 kHz.

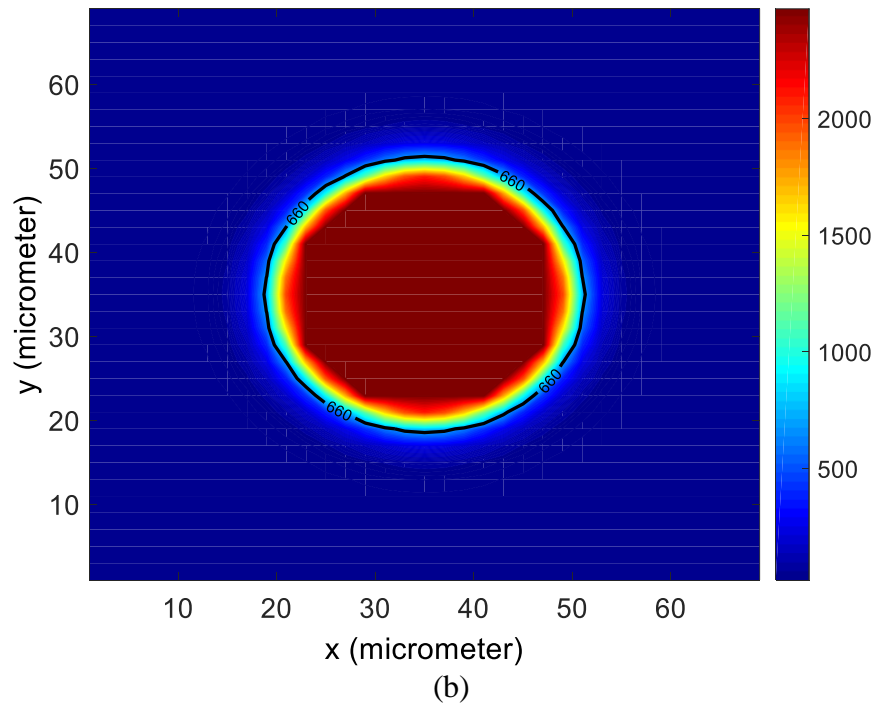
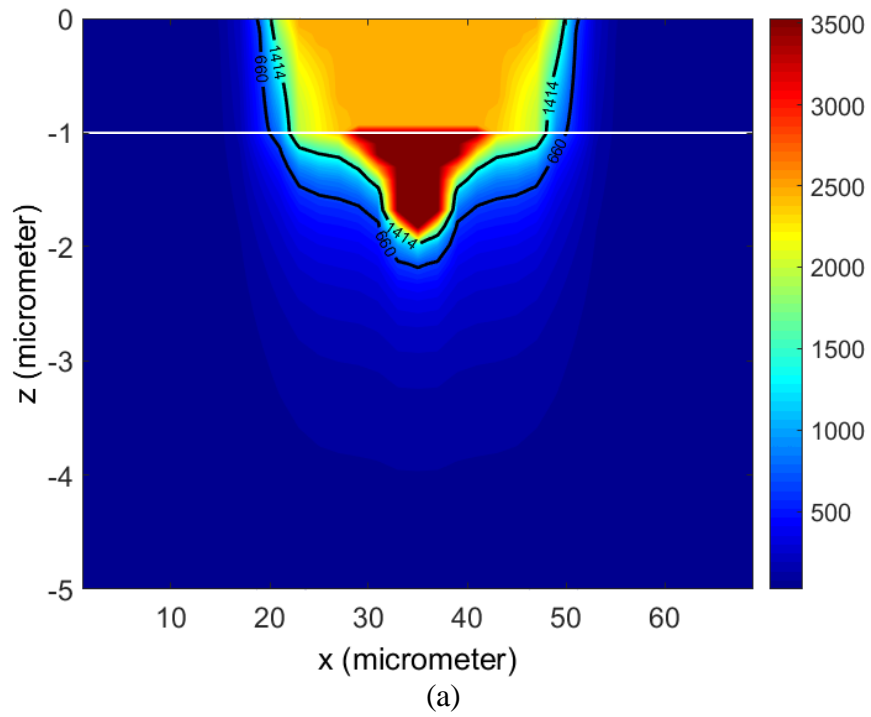


Figure 24 – Temperature contour at the end of the pulse at 50 kHz and 5 W for (a) cross-section (b) surface

4.4 Laser processing of gold coated silicon sheets

Figure 25 shows the thermal conductivity and absorbance of the gold. The variations of the specific heat with temperature are unknown. Consequently, c_p was kept constant at 129 J/kgK in the model. The melting point, boiling point, latent heat of fusion and latent heat of vaporization are 1064 °C and 2970 °C, 64 kJ/kg and 1736 kJ/kg respectively [85].

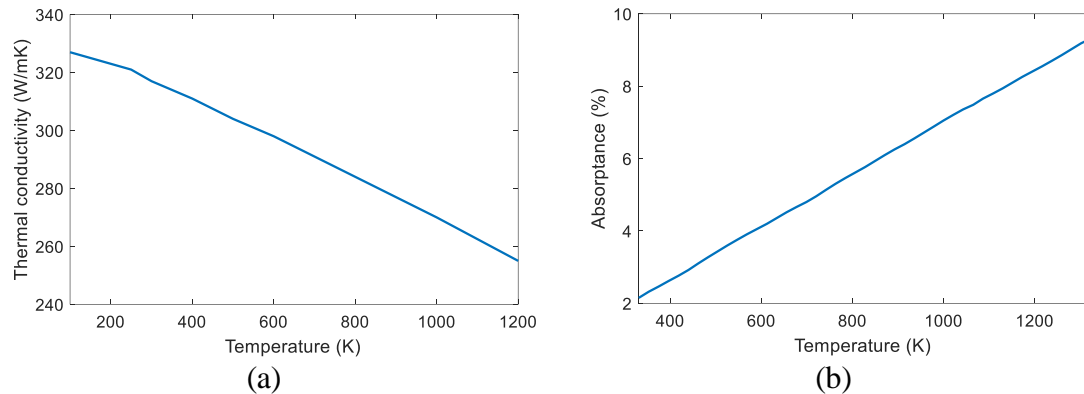


Figure 25 – (a) Thermal conductivity of gold [89], (b) absorbance of gold [87]

Figure 26 shows the plasma absorption, calculated from experimental results for gold coated samples. The calculated and measured hole profiles are shown in Figure 27 and 28 and measured and calculated depths are shown in Table 4. It is evident that the holes became slightly deeper at high powers compared to bare silicon samples. It can be explained by the reasons stated in the previous section. A quick comparison between Figure 15 and 26 shows that the plasma absorption is lower for gold coated samples and again the shock wave could have pushed away the molten material (Figure 29), which results in deeper and wider holes. However, the molten zone is very small for gold coated samples, which means the deeper holes created on the gold coated surfaces are mainly because of the lower plasma absorption.

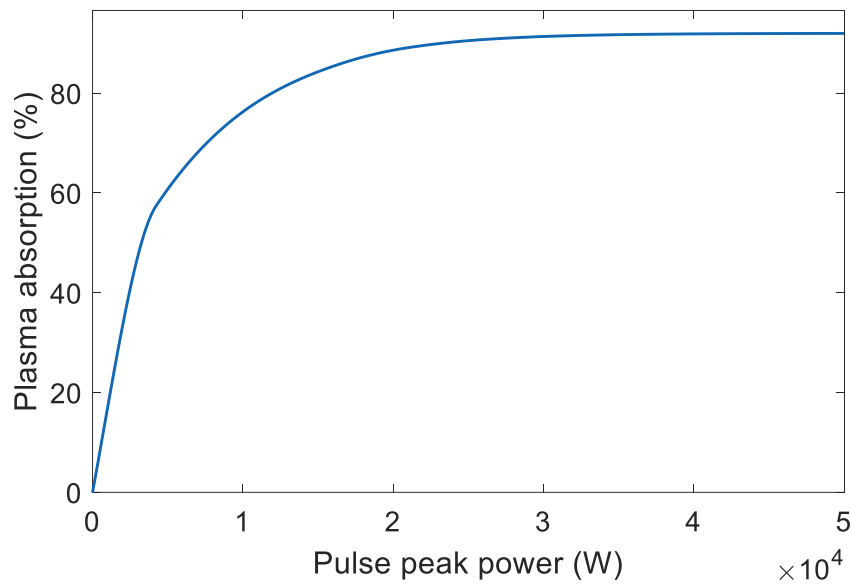


Figure 26 - Plasma absorption for laser processing of gold obtained from experimental results

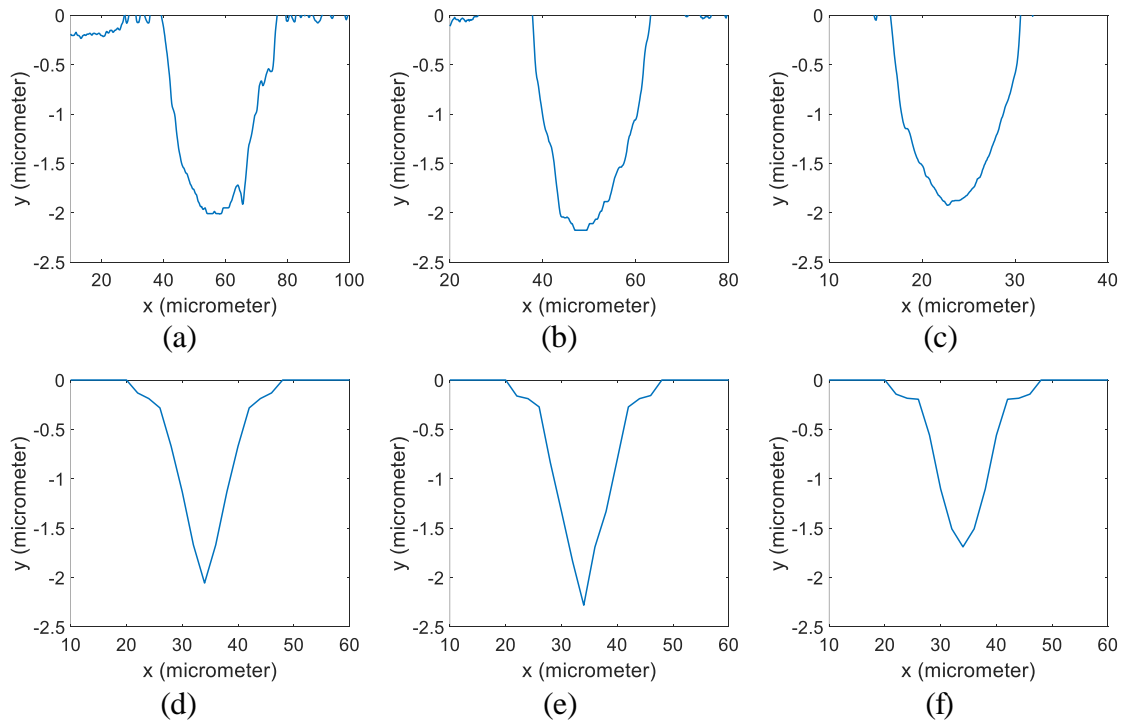


Figure 27 – (a) Measured profile at 5 W and 25 kHz, (b) measured profile at 5 W and 50 kHz, (c) measured profile at 5 W and 75 kHz, (d) calculated profile at 5 W and 25 kHz, (e) calculated profile at 5 W and 50 kHz, (f) calculated profile at 5 W and 75 kHz

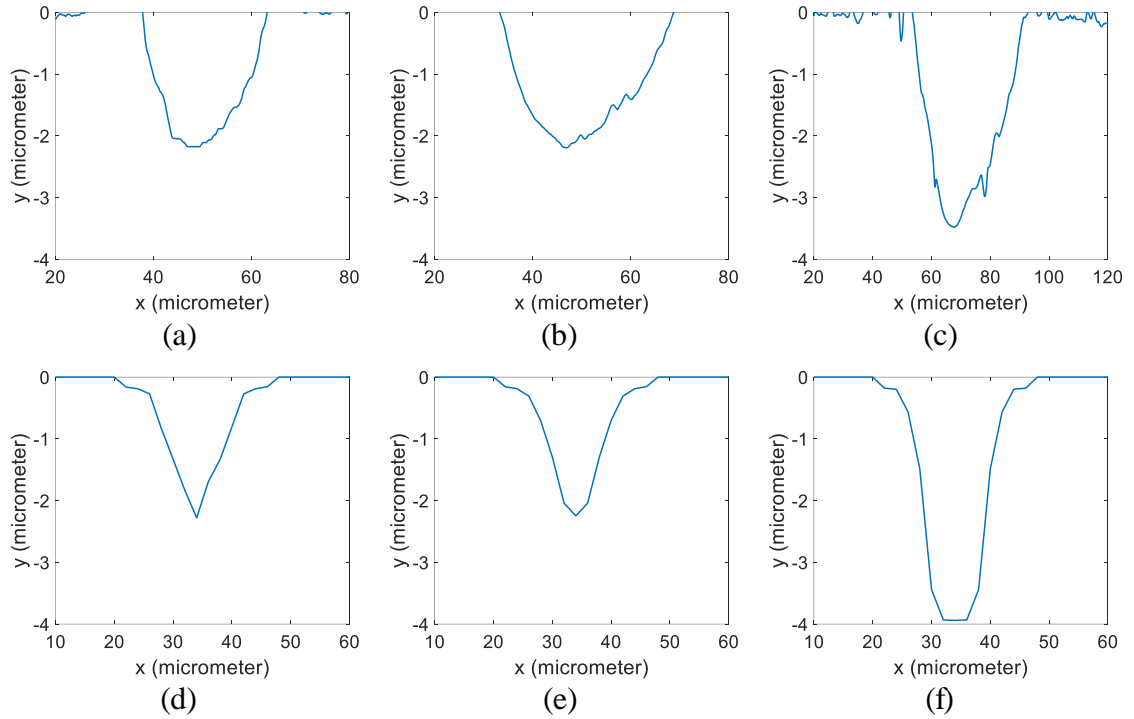


Figure 28 – (a) Measured profile at 5 W and 50 kHz, (b) measured profile at 10 W and 50 kHz, (c) measured profile at 15 W and 50 kHz, (d) calculated profile at 5 W and 50 kHz, (e) calculated profile at 10 W and 50 kHz, (f) calculated profile at 15 W and 50 kHz.

Table 4 – Measured and calculated ablation depths

Power (W)	Frequency (kHz)	Averaged measured depth (μm)	Calculated depth (μm)	Accuracy (%)
5	25	2.1	2.1	100
5	50	2.2	2.3	95.5
5	75	1.8	1.7	94.4
10	50	2.1	2.2	95.2
15	50	3.6	3.9	91.7
Standard deviation		0.71	0.85	3

The results presented in this chapter can be utilized to fabricate better biomedical devices. For instance, in the HAZ, a residual stress zone will be formed on the surface and it has been proven that living cells will avoid this area and they won't adhere to the surface. This concept can be used for cell programming which has numerous applications in

biomedical engineering. By comparing Figure 19b, 24b and 29b, we can see that the HAZ can be altered significantly by applying a thin film on the surface. Therefore, the size of the residual stress zone can be easily controlled which makes this concept even more attractive for cell programming applications.

Single pulses were studied in this chapter because, if there is more than one pulse at a certain point, the plume will contain particles from two different materials. This makes the estimation of plasma absorption extremely difficult and the process becomes too complicated for modeling. On the other hand, another issue may arise if a specific point on the surface is irradiated by multiple pulses (which happens during either laser drilling processes or patterning the sample at extremely slow scanning speeds). As the groove or hole becomes deeper, the laser beam will go out of focus. This will dramatically decrease the ablation rate and after the first two or three pulses, the laser beam will be completely out of focus and it can only melt down some material inside the hole or groove rather than removing the material and making the hole deeper or cutting the material. Since there is not enough information about the out of focus beam profile, it is impossible to model the process for multiple pulses.

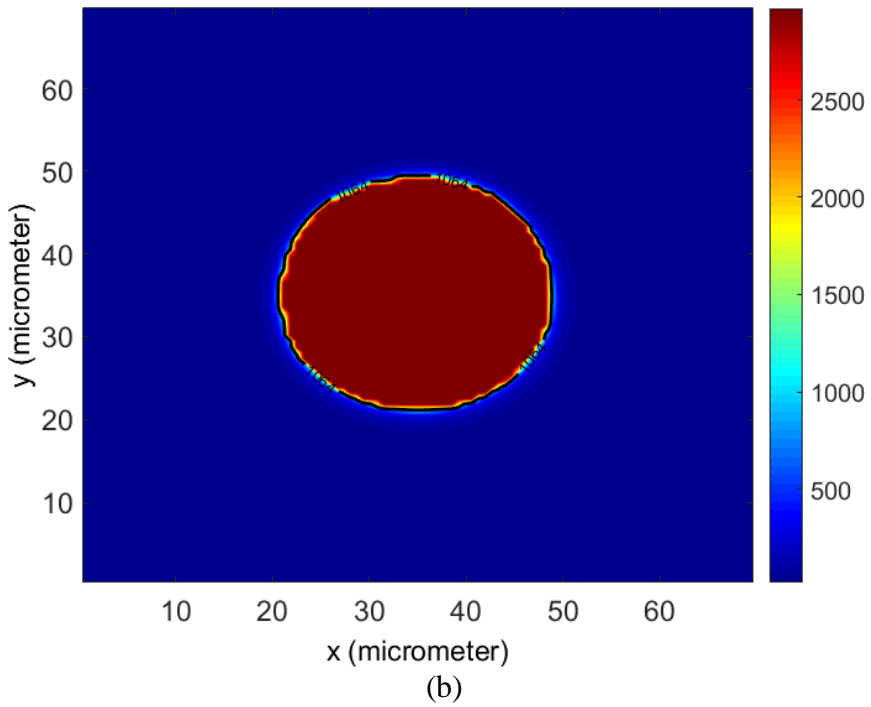
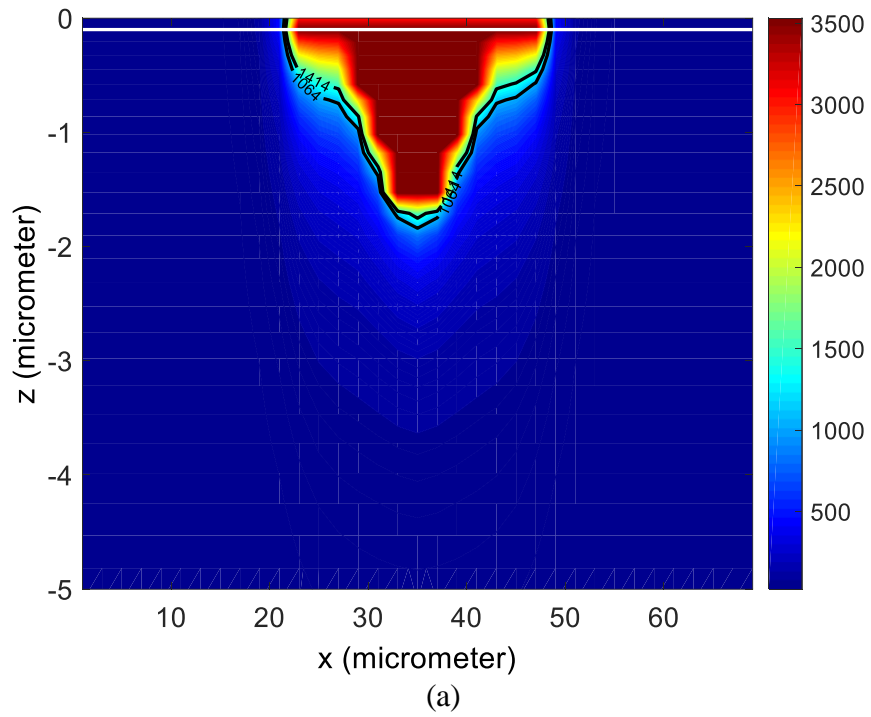


Figure 29 – Temperature contour at the end of the pulse at 50 kHz and 5 W for (a) cross-section (b) surface

Chapter 5

Potential use of laser treated metallic surfaces coated by a thin layer of electrospun fibers for implant fabrication³

This chapter shows an example of laser processed thin film multilayer structure that can be potentially used for biomedical applications. Moreover, a thermal analysis has been carried out on a dental implant that shows that applying the proposed method on a dental implant not only can improve its biocompatibility, but also can enhance its thermal properties.

³ The results presented in this chapter were published in the Journal of Applied Physics. Naghshine, B. B., Cosman, J. A., & Kiani, A. (2016). Synthesis of polycaprolactone-titanium oxide multilayer films by nanosecond laser pulses and electrospinning technique for better implant fabrication. *Journal of Applied Physics*, 120(8), 084304.

5.1 The proposed method

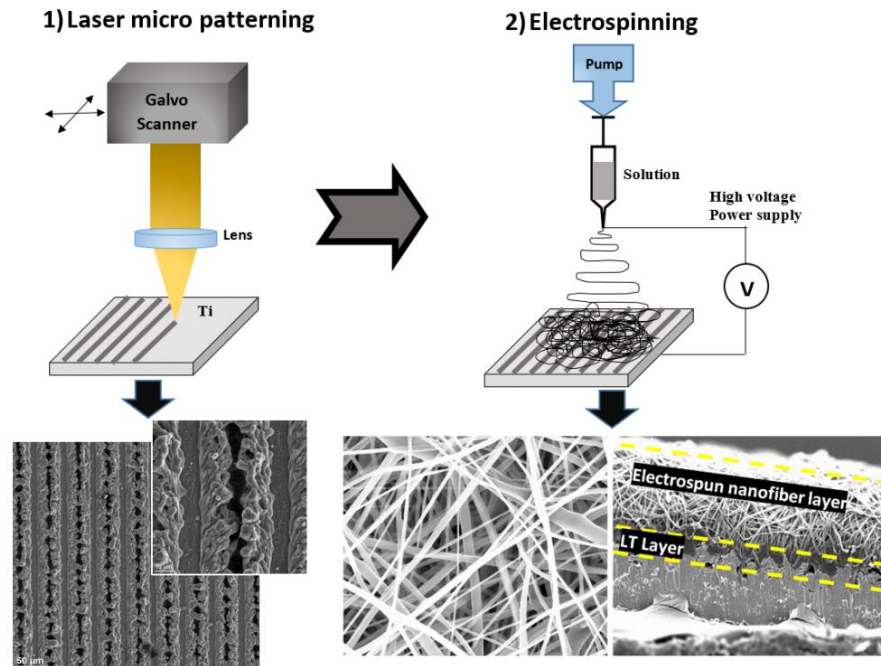


Figure 30 - Combination of laser processing and electrospinning

Although both electrospinning and laser processing have been widely studied separately as effective methods of surface modification for biomedical applications, nothing could be found about simultaneous use of both methods. In the current study, a combination of the two methods mentioned here was applied to a Ti surface as a new approach for increasing the biocompatibility of metal implants. Electrospun fibers of polycaprolactone (PCL) were aimed at a laser treated Ti surface (Figure 30). The main advantage of this new method is better short-term biocompatibility (before degradation of electrospun fibers), due to the highly porous structure and better wettability of fibers compared to bare Ti, while maintaining a rough and porous laser treated surface, even when fibers are completely absorbed by body. Therefore, we can benefit from both short-term and long-

term biocompatibility provided by two different methods. The method can be used in the fabrication of any kind of implant for various parts of the body, including dental implants or any bone implant used for hip or knee replacement.

5.2 Sample preparation

The titanium sheet was processed at a repetition rate of 100 kHz and a power of 10 W with a scanning speed of 200 mm/s. These are the optimized parameters for the same laser system to increase the biocompatibility of Ti which are taken out from previous works [2, 3].

Table 5 - Chosen parameters for electrospinning process

	Concentration (%)	Needle to collector distance (cm)	Voltage (kV)	Flow rate (ml/hr)
Nanoscale fiber	5	10	15	1
Microscale fiber	15	18	20	5

Table 5 shows the chosen parameters used to fabricate the nanoscale and microscale fibers. Microscale and nanoscale fibers were successfully generated on the titanium sheets with chosen favorable parameters. SEM images of electrospun PCL fibers on the surface of the samples prior to being immersed in SBF are shown in Figure 31. The average diameter of the fibers was calculated to be 185 nm for nanoscale fibers and 843 nm for microscale fibers. Also, image processing of SEM images shows that porosity is 17% for nanoscale fibers and 38% for microscale fibers. Although Figure 31 and 33 may indicate higher porosity for nanoscale fibrous structures at first glance, it should be noted that SEM

images are two-dimensional and as the diameter of the fibers increases, fibers from deeper layers can be seen in the image. On the other hand, deeper layers seem darker and they are filtered based on color to keep only the first two or three layers. Porosity is calculated using those filtered images. Moreover, the microscale samples had higher thicknesses despite consuming the same amount of PCL solution for fabrication of all the samples, which proves that microscale fibrous structures had higher porosities.

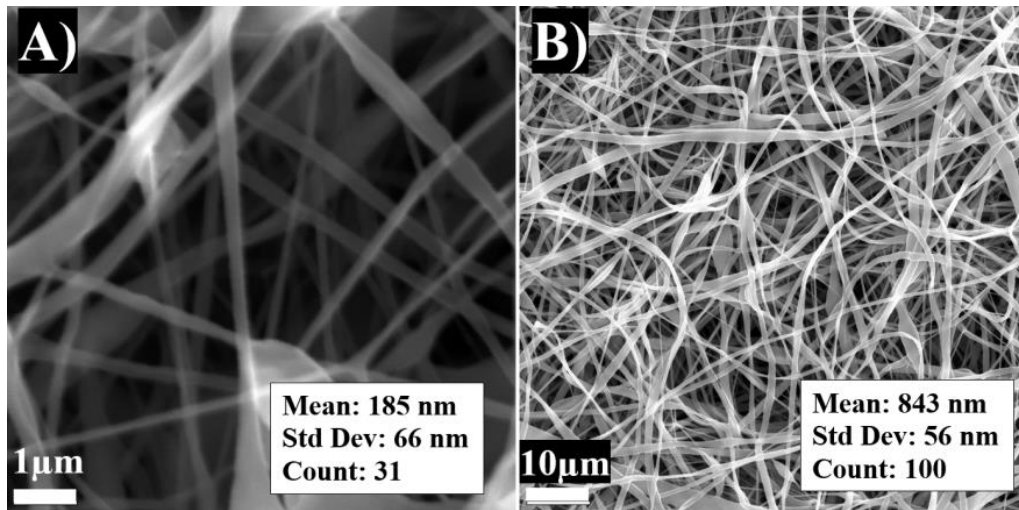


Figure 31 - SEM images of sample surfaces before SBF immersion. A) nanofibers B) microfibers

5.3 Biocompatibility assessment

For SBF immersion tests, laser and non-laser-processed samples for both nanofibers and microfibers results were recorded and compared. Samples were soaked in SBF and kept inside an incubator for four weeks, and the temperature was kept constant at approximately 37 °C. SEM images of these samples are shown in Figure 32 and 33, and it is evident that more HA is formed on the surface of nanofiber, laser-processed samples.

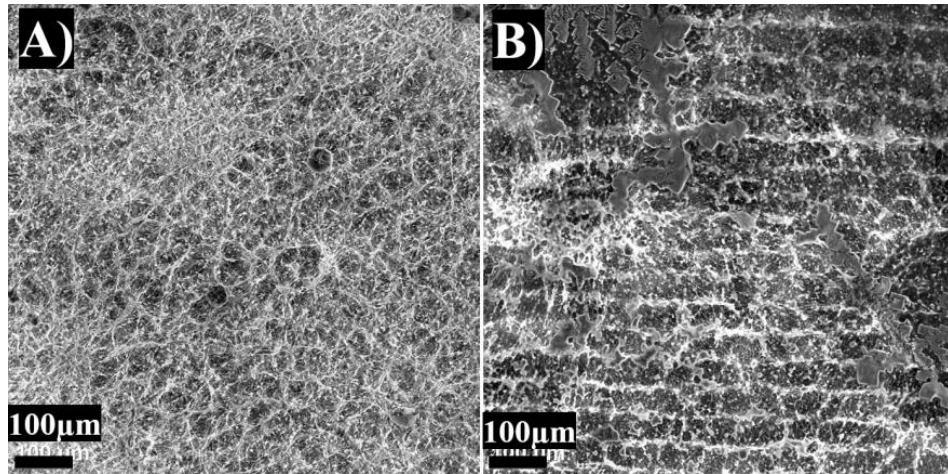


Figure 32- SEM images of samples with microscale fibers after SBF immersion. A) unprocessed sample, 5000X magnification B) laser-processed sample, 5000X magnification

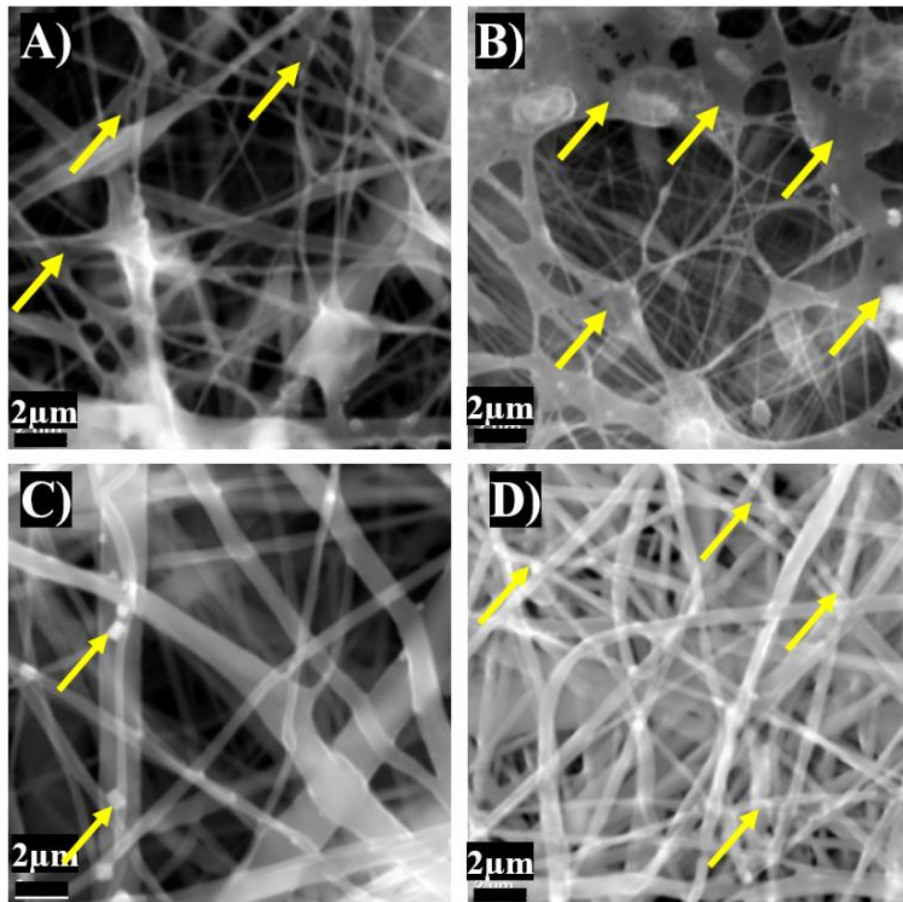


Figure 33 - SEM images of samples with nanoscale fibers after SBF immersion. A) Unprocessed sample, 100X magnification; B) laser-processed sample, 100X magnification; C) unprocessed sample, 5000X magnification; D) laser-processed sample, 5000X magnification

In analyzing EDX results, more of the emerging HA components, calcium and phosphorous, can be found in the greatest amounts in the laser-processed nanofiber sample as compared to their lowest amounts in the unprocessed, microfiber sample (Figure 34). By comparing Figure 34 to the previously published EDX analysis of the uncoated titanium sheets processed by the same laser system [90], it is evident that calcium and especially phosphorous peaks are much stronger when the sample is coated by electrospun fibers.

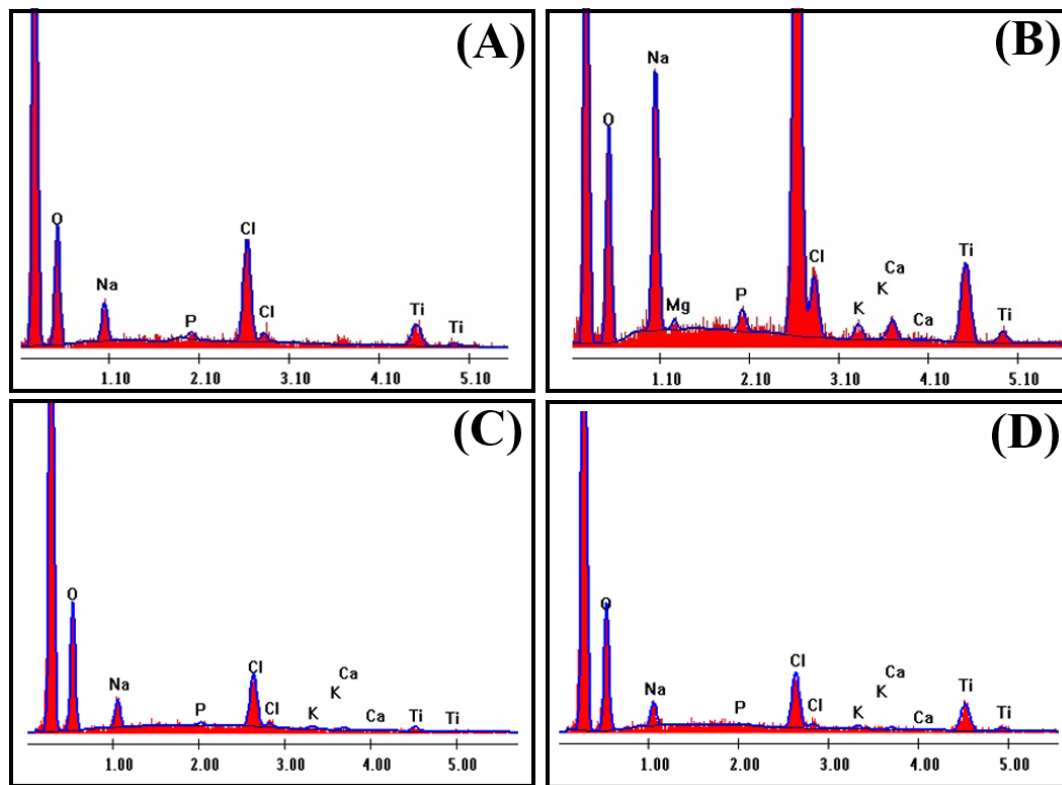


Figure 34 - EDX analysis of A) unprocessed nanoscale sample B) processed nanoscale sample C) unprocessed microscale sample D) processed microscale sample

XRD results are depicted in Figure 35. The X-ray source was a sealed 2.2 kW Cu X-ray tube and the operating voltage and current were 40 kV and 30 mA. The X-ray optics was based on the Bragg-Brentano para-focusing geometry. Samples were scanned in the range

of $2\theta=5-80^\circ$. As it can be seen, the presence of HA is confirmed in nanoscale samples by appearance of five characteristic peaks at $2\theta=26^\circ, 31.6^\circ, 32^\circ$ and 32.8° [91] and the intensity is higher in the laser-processed samples. However, no HA can be seen in the microscale samples. Some other peaks are also visible in Figure 35 at $2\theta=21.5^\circ, 22.5^\circ, 24^\circ, 26.5^\circ$ and 27.5° which are not among the characteristic peaks of HA. Moreover, a peak corresponding to CaCO_3 can be seen at $2\theta=26.5^\circ$ for some samples and also another peak at $2\theta=22.5^\circ$ is visible in nanoscale samples which is related to PCL.

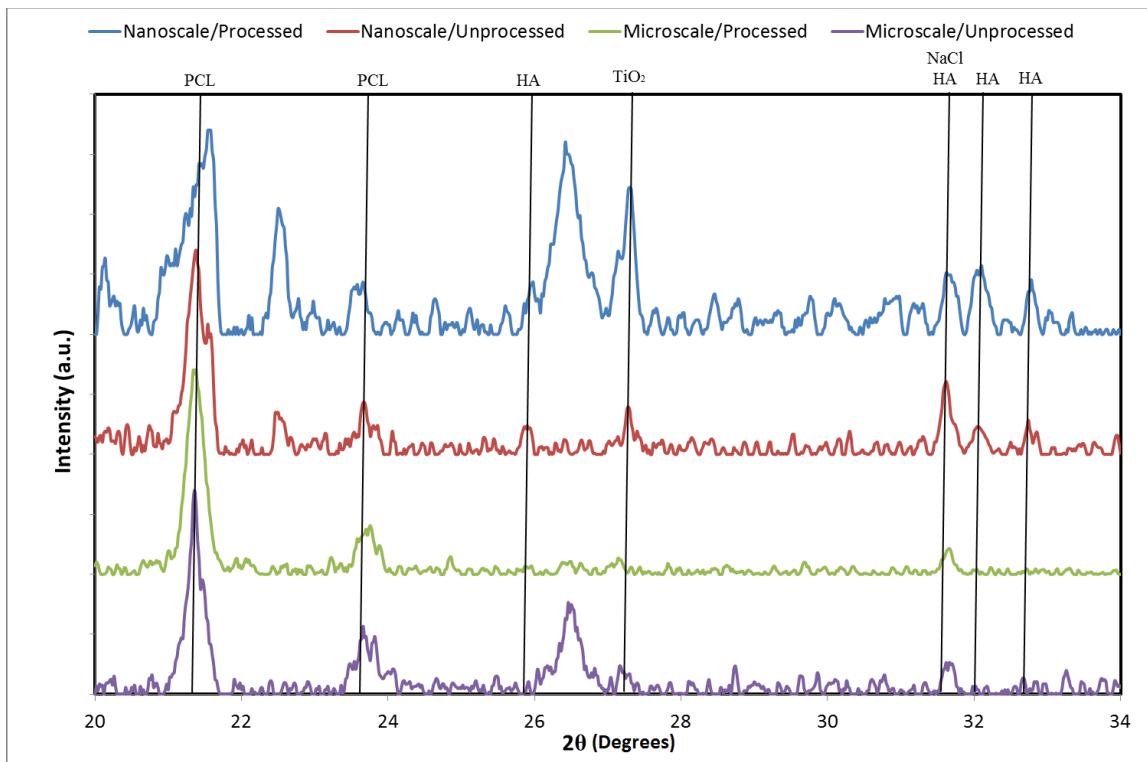


Figure 35 - XRD analysis of samples

Overall, the generated nanofibers, in comparison with microfibers, were shown to have more HA formation following SBF immersion, as shown in Figure 32 and 33. The gaps between fibers that appear in both micro and nano SEM images prove this as nanofibers

have gaps consistently filled with HA, whereas microfibers have inconsistent and small portions of developing HA. This can be attributed to the fact that nanofibers have a higher surface area which results in steady HA accumulation.

When referring to these same figure with samples representing processed and unprocessed conditions, surface treatment of materials with laser radiation also resulted in an increased surface area due to the formation of a rough, columnar surface topography. Thus, like the comparison of nanofibers to microfibers, the increased surface area in laser-processed samples resulted in more favorable conditions. With this higher surface area, nanofiber samples are the most apt to HA generation following the immersion in SBF.

Regarding EDX results, more oxygen was found to be present after laser processing as compared to the non-processed samples. The biocompatibility of Ti is attributed to the existence of the thin TiO_2 layer, and this layer was more profound for laser-processed samples. There is a strong correlation between the increase of oxygen and an increase of HA components calcium and phosphorous. Similarly, nanoscale results were more significant for the presence of these elements as well, as compared to microscale (Figure 34).

5.4 Thermal analysis of a dental implant coated by electrospun fibers while drinking a hot beverage

For dental implants, an additional factor should be taken in account, which is the significant mismatch between Ti and bone in terms of thermal properties. A relatively large heat flux can be conducted through the implant while drinking a hot beverage, which can cause damage to recently formed cells during the healing period. The temperature

increase caused by drinking a hot beverage can be quite significant. Wong et al. showed that a 47°C increase in temperature can be detected 3 mm away from a heat stimulus of 60°C through a simple analytical solution to a heat transfer equation inside the dental implant [92]. Feuerstein et al. recorded temperatures as high as 76.3°C when they measured tooth-gum interface temperatures of 14 volunteers while they drank very hot beverages [93]. Patel and Geerts performed similar experiments. They reported that in 58% of their tests the $47^{\circ}\text{C}/\text{min}$ threshold of bone injury was reached [94]. Ashtiani and Imani solved a three-dimensional heat transfer equation using a commercial numerical solver to calculate root, crown, and mandible temperature. Their results show that a maximum temperature of 55°C occurs at the bone-implant interface while it is exposed to a liquid at a temperature of 67°C [95].

Since the thermal conductivity of most polymers is very low, applying an electrospun layer of PCL fibers to the surface can have positive effects on the thermal properties of the dental implant during the healing period.

Heat transfer equations were solved to calculate the temperature around a dental implant while being exposed to a hot beverage to make sure that electrospun fibers can act as a proper insulator layer. Crown, root, and bone were considered to have a cylindrical shape (Figure 36). For this geometry, a two-dimensional heat conduction equation in cylindrical coordinates (Eq. 22) was solved [96].

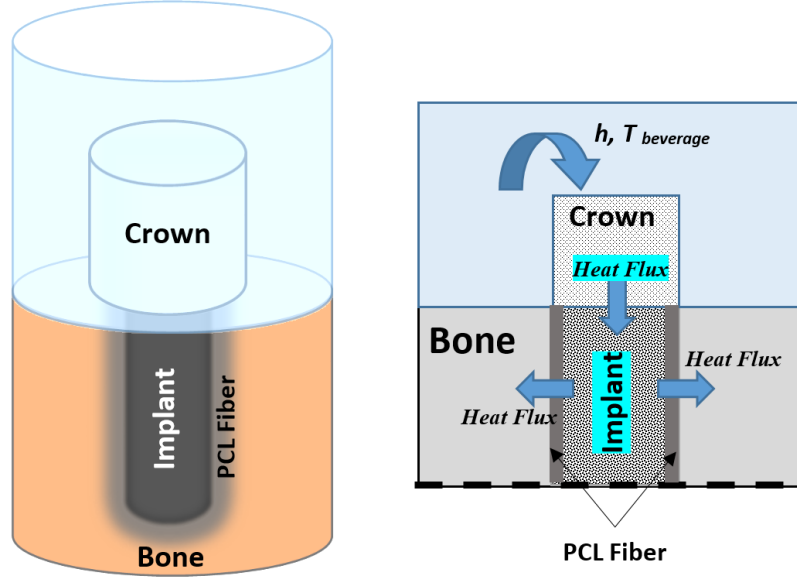


Figure 36 - Cross-sectional view of crown, implant, fibers and bone

$$\rho c_p \frac{\partial T}{\partial t} = \frac{k}{r} \frac{\partial}{\partial r} \left(r \frac{\partial T}{\partial r} \right) + k \frac{\partial^2 T}{\partial x^2} \quad (22)$$

For the electrospun layer, a simple porous media model was used (Eq. 23), where $\overline{\rho c_p}$ and \overline{k} are calculated through Eq. 24 and 25 [96].

$$\overline{\rho c_p} \frac{\partial T}{\partial t} = \frac{\overline{k}}{r} \frac{\partial}{\partial r} \left(r \frac{\partial T}{\partial r} \right) + \overline{k} \frac{\partial^2 T}{\partial x^2} \quad (23)$$

$$\overline{\rho c_p} = (1-P)(\rho c_p)_{fiber} + P(\rho c_p)_{fluid} \quad (24)$$

$$\overline{k} = (1-P)k_{fiber} + Pk_{fluid} \quad (25)$$

In these equations P is the porosity of fibrous structure. Additionally, Pennes' equation [97] was written for the bone (Eq. 26). In this equation ω is blood perfusion rate and $q''_{metabolism}$ is metabolism heat generation. Their values are 1 ml/min/100g and 136 W/m³ respectively for cancellous bones [98]. T_{blood} is also set at 37 °C.

$$\rho c_p \frac{\partial T}{\partial t} = \frac{k}{r} \frac{\partial}{\partial r} \left(r \frac{\partial T}{\partial r} \right) + k \frac{\partial^2 T}{\partial x^2} + q''_{metabolism} + \omega(\rho c_p)_{blood} (T_{blood} - T) \quad (26)$$

Material properties are assumed to be constant and are listed in Table 6.

Table 6 - Mechanical and thermal properties of materials

Material	Density (kg/m ³)	Thermal Conductivity (W/mK)	Specific Heat (J/kgK)
Bone [98]	1210	0.29	2290
Root (Ti)	4510	11.4	523
Crown [95]	2400	1.5	1070

These equations were solved using the ADI method described in section 2.2.1. Additional terms in Eq. 26 were added as source terms. The bone cylinder was considered larger than the root and crown. Consequently, a symmetry boundary condition was written on the outer surface of the bone cylinder. A convective boundary condition was written for the crown due to its exposure to the hot beverage. Moreover, because of the interfacial continuity condition among all the cylinders, equal heat flux was considered in the interfaces. A C++ program was developed to solve these equations.

The Hot Disk TPS Thermal Analyser was used to evaluate this model and measure the thermal conductivity of the electrospun fibers. In the TPS technique, thermal conductivity and specific heat are calculated based on an analytical solution of the heat equation for an infinitely thick solid sample, and temperature changes measured after applying heat on the surface of the sample. The Hot Disk cannot be used directly to measure the thermal

properties of electrospun fibers, since they have a porous structure and are very thin; which is very different from assumptions made in the TPS technique. Therefore, the Hot Disk was only used to extract the temperature curve after applying the power on the surface of the fibrous layer.

The samples were placed on a thick stainless steel cylinder with known thermal properties and a 200 mW heat source was applied to the fibrous layer through a Hot Disk sensor in the shape of a double spiral with a diameter of 4.002 mm. The sensor also measures the temperature. The temperature trend on the surface of the fibrous layer was then extracted using the Hot Disk Thermal Analyser. The same equations (Eq. 22-25) were numerically solved for the same geometry, including a thick stainless steel layer, a thin Ti sheet, and a thin fibrous layer filled with air. A concentric ring shape was considered for the heat sources to mimic the spiral shape of the sensor. The thermal conductivity is estimated from the temperature curve through this model.

The thickness of the Ti sheet was 100 μm and the thickness of the fibrous layer was measured to be 80 μm for microscale fibers and 50 μm for nanoscale fibers using cross-sectional SEM images. As mentioned in section 5.2, porosity was estimated by image processing of the SEM images. Specific heat of the PCL is 1400 J/kgK [99] and its density is 1145 kg/m³. The code was run multiple times with different thermal conductivity values for PCL. As is shown in Figure 37, a good agreement can be seen at $k=0.1$ W/mK which is a reasonable number since k is usually less than 0.3 for most polymers. Hence, \bar{k} is 0.072 W/mK and 0.087 W/mK for microscale and nanoscale fibrous layers respectively when they are filled with air. However \bar{k} will be 0.25 W/mK (microscale fibers) and 0.17

W/mK (nanoscale fibers) when the fibrous layer is filled with extracellular fluid inside the body.

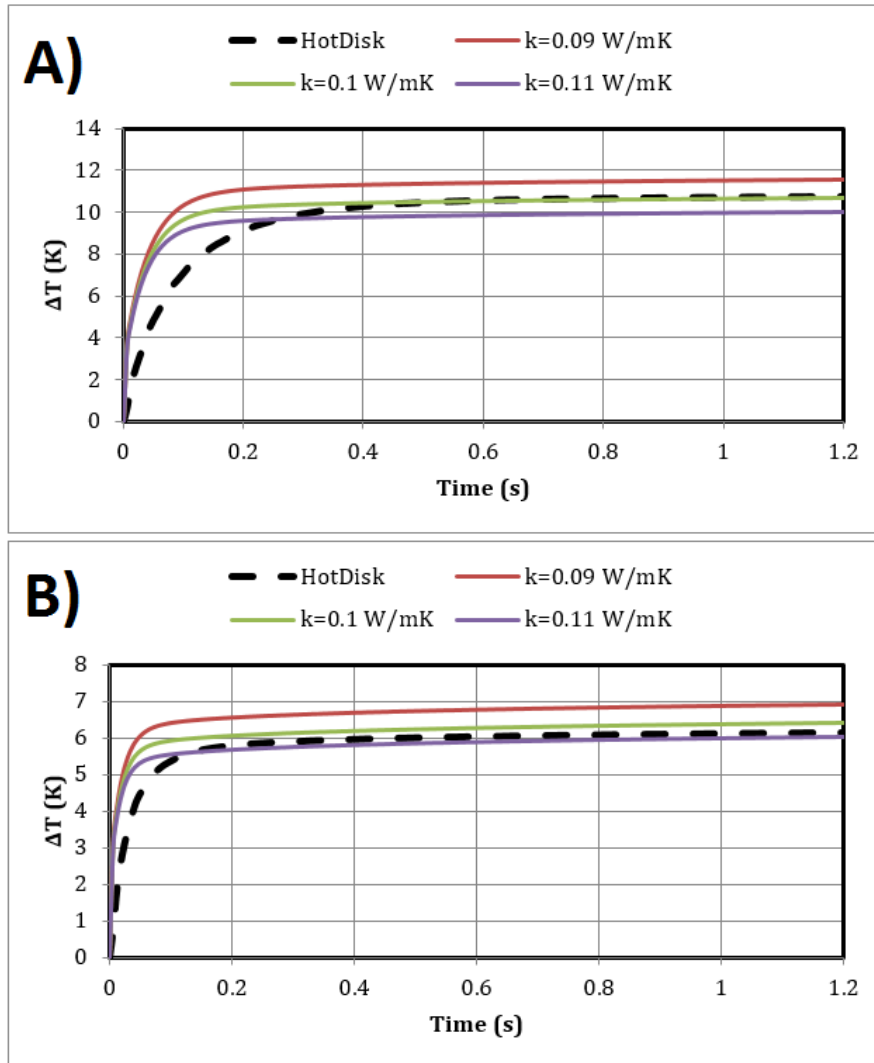


Figure 37 - Temperature rise of fibrous layer after applying a 200 mW heat source for A) microscale sample B) nanoscale sample

Solving the heat transfer equation for the geometry shown in Figure 36 indicates that the presence of a 1 mm thick electrospun layer of the same nanoscale PCL fibers fabricated in this study can decrease the temperature rise of bone by about 10 °C after one minute of

exposure to a hot beverage (Figure 38). Beverage (coffee) temperature is assumed to be 85 °C for the worst-case scenario [100] and convective heat transfer coefficient is 5000 W/m²K [95, 101]. The flowchart of the computational code is shown in Figure 39.

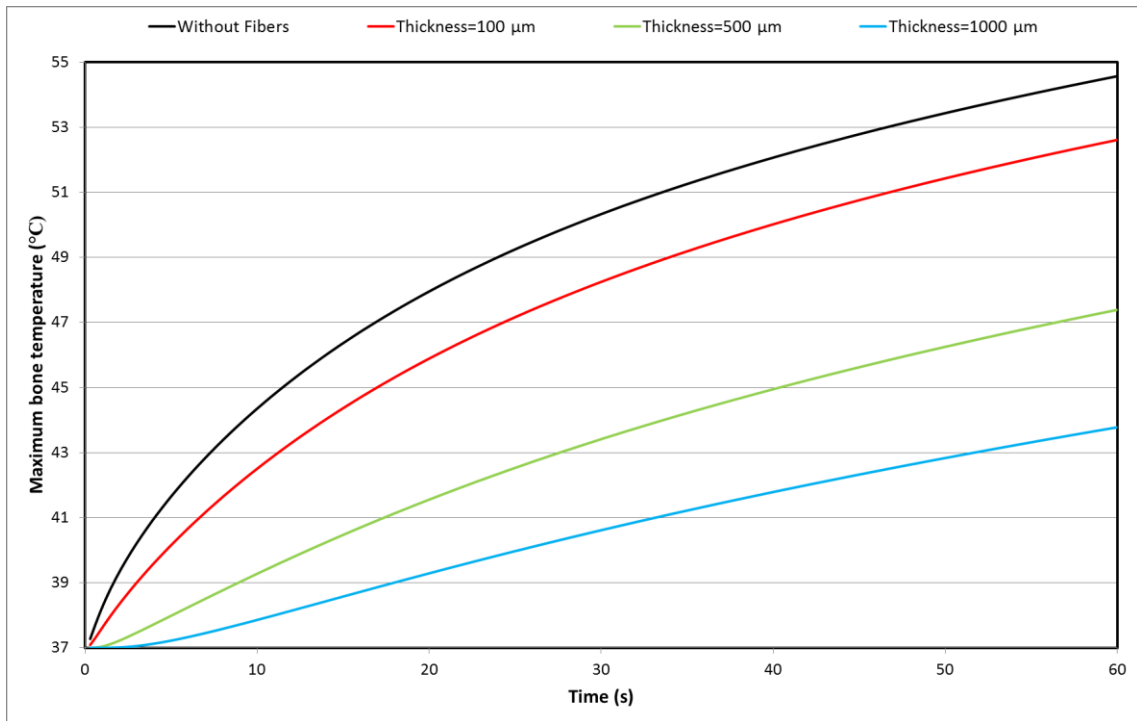


Figure 38 - Maximum bone temperature while drinking hot coffee, considering an implant without any fiber and implants covered with a layer of electrospun nanoscale fibers with three different thicknesses.

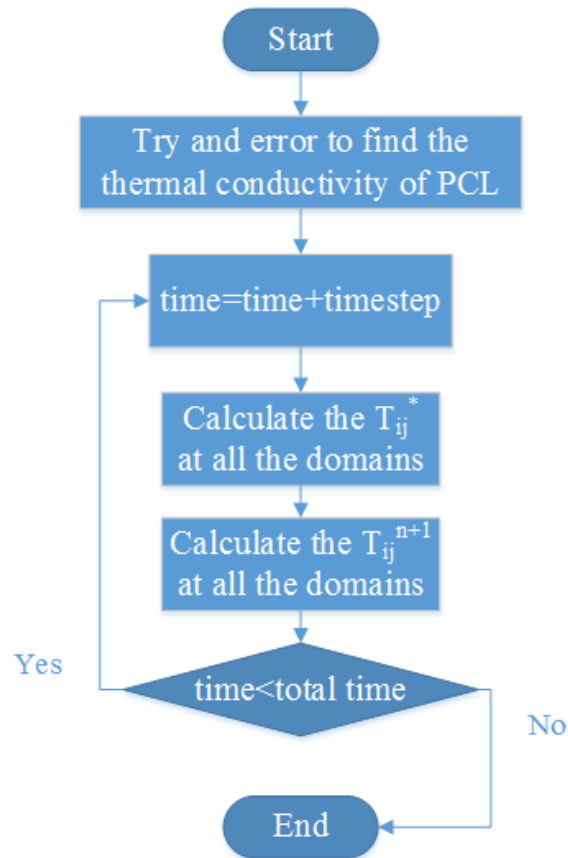


Figure 39 – The flowchart of the computational code

5.5 Adding antibacterial agents to the fibers

In this study, silver nanospheres and ampicillin were added to the fibers to make them antibacterial and prevent the implant-related infections as explained in section 1.1.9. The silver suspension and ampicillin powder were directly added to the electrospinning solution at different concentrations. After covering the titanium sheet with the fibers, they were placed inside the LB agar dishes containing ampicillin resistant and wild type *E. coli*, and were incubated for 24 hours at 37 °C.

Silver is a very strong bacteriostatic material, which means it can stop the bacteria from reproduction without killing them. The main advantage of silver over antibiotics is that,

bacteria cannot become resistant to it. That's why it has recently been considered for clinical applications. The only issue is the toxicity of silver. However, the high surface to volume ratio of silver nanoparticles allows them to effectively stop the bacteria from reproduction even at very small doses that are not toxic to human body [102, 103]. The silver nanospheres at three different sizes (20, 40 and 80 nm) were suspended in water at the concentration of 0.02 mg/ml. The silver suspension was added to the electrospinning solution at 1 wt% and 5 wt%. It should be noted that, at higher concentrations, the solution was not electrospinnable. No zone of inhibition was observed for wild type and ampicillin resistant *E. coli* at different sizes and concentration (Figure 40). That's mainly because of the low concentration of silver nanospheres in the suspension and the limit for adding the suspension to the solution. Adding the particles to the fibers by a different method can be considered in future studies.



Figure 40 – Antibacterial testing of the fibers containing silver nanospheres against wild type *E. coli*.

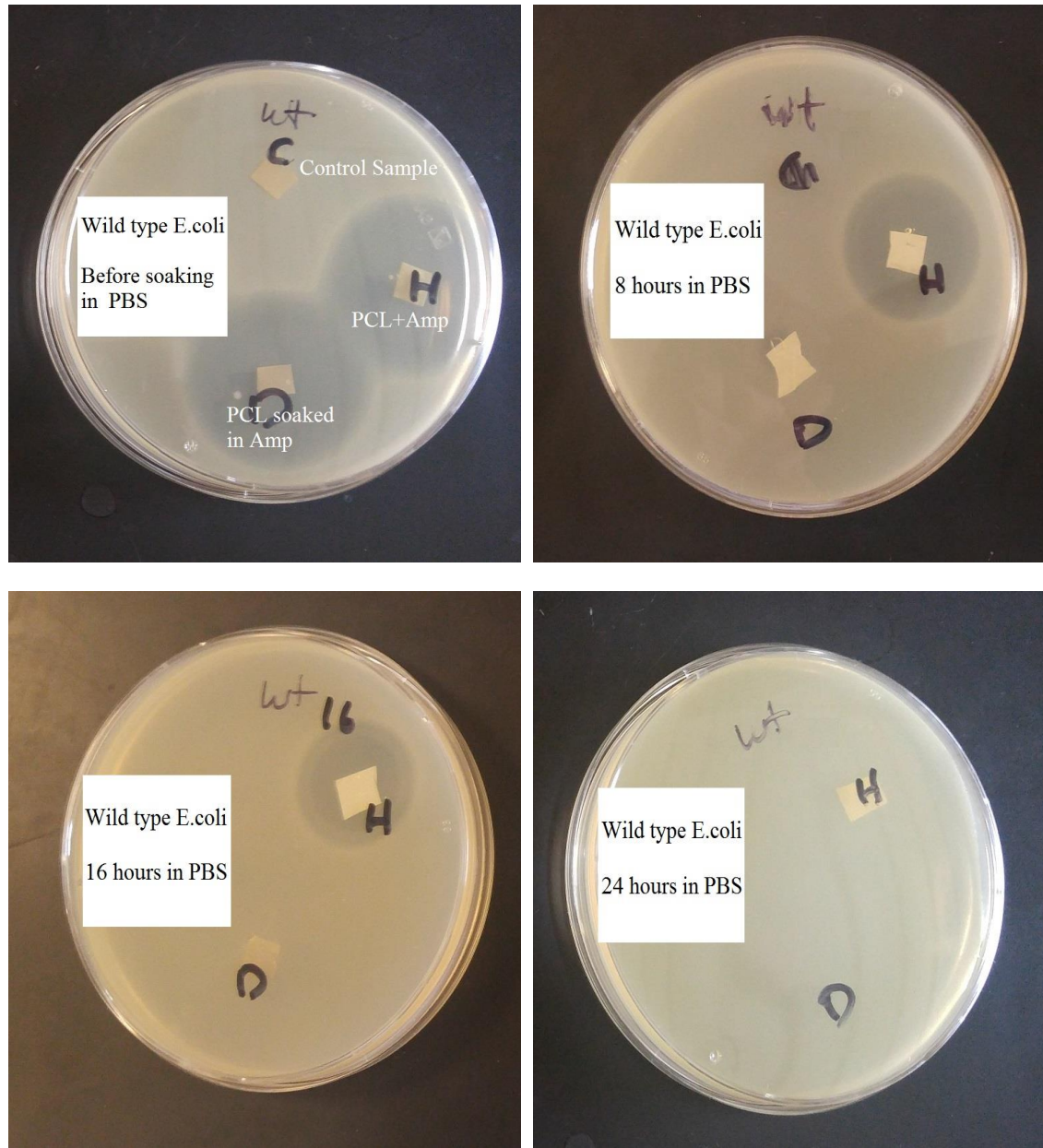


Figure 41 - Antibacterial testing of the ampicillin loaded fibers (labeled as "H" in the images) and fibers soaked in ampicillin (labeled "D" in the images) against wild type E. coli.

In the second phase, ampicillin powder was added to the solution at the highest possible concentration which is 16 wt%. The samples were placed inside the LB agar dishes. A control sample without ampicillin was placed at each plate and also, another sample was

soaked in a high concentration ampicillin solution (100 mg/ml) and was placed in each dish. The samples were soaked in PBS for different time spans (8, 16 and 24 hours) to assess the release rate of the ampicillin. As predicted no zone of inhibition was observed for ampicillin resistant E. coli. However, a clear zone of inhibition was observed around the ampicillin loaded fibers and the soaked samples. After soaking the samples in PBS, no zone was observed around the soaked sample. On the other hand, there was still a zone of inhibition around the ampicillin loaded sample after 8 and 16 hours, which shows the release rate was much slower when the ampicillin was added to the solution (Figure 41).

Chapter 6

Summary and future work

6.1 Summary

In this thesis, laser processing of thin film coated metals for biomedical applications was studied. This study shows how applying a thin film on the surface can affect the laser processing and how we can control the surface properties. This can provide us with new possibilities that can be useful for designing new and better biomedical devices.

In this thesis, a very thorough model was introduced for laser processing of metallic surfaces. In this model, many factors including varying thermal properties, plasma shielding and laser beam profile were taken into account. The model is three-dimensional,

which enables us to model the movement of the laser beam and therefore add scanning speed as a very important laser parameter to the model. This model can return the groove profile and temperature field for any given laser parameters, including power, repetition rate and scanning speed. The results were verified by experimental measurements and a very strong correlation was observed between numerical and experimental results.

This model was modified for laser processing of a thin film coated sample by a single pulse. The results were validated by experimental measurements on a silicon sheet coated by aluminum and gold thin films. It has been shown that, applying a thin film can completely alter the temperature field and surface profile mainly through altering the plasma absorption coefficient.

Thin film coating of laser processed materials was also introduced as a new method for surface modification of the bone implants. In the introduced method, a laser treated titanium sheet was coated by a thin film of PCL micro/nano fibers generated through electrospinning process. PCL is an excellent biocompatible and biodegradable polymer that provides a more favorable environment for cell proliferation compared to a piece of metal. On the other hand, PCL will be degraded after a while and if it is coated on a laser treated surface, the cells can easily adhere to the laser processed surface, which improves the long-term biocompatibility of the implant. A SBF test was carried out to assess the short-term biocompatibility of the laser treated titanium sheets coated by nanoscale and microscale PCL fibers. The specimens were analyzed through SEM, EDX and XRD and the bone-like hydroxyapatite was successfully identified on the surface of the samples and

the highest amount of hydroxyapatite was found on the laser treated samples that were coated by nanoscale PCL fibers. This shows that, the presence of a laser processed surface underneath the electrospun fibers can enhance the short-term biocompatibility. It was also proven that, the electrospun layer can act as a thermal insulator which makes it even more biocompatible when this method is applied to a dental implant that is under a large heat flux during the hot beverage intake. Furthermore, Ampicillin was successfully mixed with the electrospun fibers. In vitro tests were carried out that shows that the ampicillin will be gradually released inside the body within the first 24 hours, which can reduce the risk of infection.

6.2 Future work

The following are suggestions for future studies to explore the full potential of the techniques introduced in this thesis:

- Estimation of the out of focus laser beam profile to model the laser processing at slow scanning speeds and laser drilling process.
- Modeling the laser processing of polymers.
- Conducting in vivo tests to assess the long-term biocompatibility of the laser treated titanium coated by electrospun fibers.
- Replacing PCL with a hydrophilic polymer such as chitosan for electrospinning process to further improve the biocompatibility.
- Replacing ampicillin with a hydrophilic antibiotic such as tetracycline to obtain a slower release rate.

- Laser processing of the electrospun fibers and assess their biocompatibility.
- Adding silver nanoparticles to the fibers by a different method.

References

- [1] M. Radmanesh, A. M. Ektesabi, R. A. Wyatt, B. D. Crawford, and A. Kiani, "Mouse embryonic fibroblasts accumulate differentially on titanium surfaces treated with nanosecond laser pulses," *Biointerphases*, vol. 11, p. 031009, 2016.
- [2] M. Radmanesh and A. Kiani, "Effects of laser pulse numbers on surface biocompatibility of titanium for implant fabrication," *Journal of Biomaterials and Nanobiotechnology*, vol. 6, p. 168, 2015.
- [3] M. Radmanesh and A. Kiani, "Bioactivity enhancement of titanium induced by Nd: Yag laser pulses," *Journal of applied biomaterials & functional materials*, pp. 0-0, 2015.
- [4] C. Colpitts and A. Kiani, "Synthesis of Bioactive Three-dimensional Silicon-oxide Nanofibrous Structures on the Silicon Substrate for Bionic Devices' Fabrication," *Nanomaterials and Nanotechnology*, 2016.
- [5] C. Colpitts, A. M. Ektesabi, R. A. Wyatt, B. D. Crawford, and A. Kiani, "Mammalian fibroblast cells show strong preference for laser-generated hybrid amorphous silicon-SiO₂ textures," *Journal of Applied Biomaterial & Functional Materials*, vol. 15, pp. 1-106, 2017.
- [6] W. Xue, B. V. Krishna, A. Bandyopadhyay, and S. Bose, "Processing and biocompatibility evaluation of laser processed porous titanium," *Acta biomaterialia*, vol. 3, pp. 1007-1018, 2007.
- [7] V. K. Balla, S. Banerjee, S. Bose, and A. Bandyopadhyay, "Direct laser processing of a tantalum coating on titanium for bone replacement structures," *Acta biomaterialia*, vol. 6, pp. 2329-2334, 2010.
- [8] S. Jin, Y. Choe, S. Lee, T.-W. Kim, M. Mativenga, and J. Jang, "Lateral grain growth of amorphous silicon films with wide thickness range by blue laser annealing and application to high performance poly-Si TFTs," *IEEE Electron Device Letters*, vol. 37, pp. 291-294, 2016.
- [9] J. Boyce, P. Mei, R. Fulks, and J. Ho, "Laser Processing of Polysilicon Thin-Film Transistors: Grain Growth and Device Fabrication," *physica status solidi (a)*, vol. 166, pp. 729-741, 1998.
- [10] H. Kuriyama, S. Kiyama, S. Noguchi, T. Kuwahara, S. Ishida, T. Nohda, *et al.*, "Enlargement of poly-Si film grain size by excimer laser annealing and its application to high-performance poly-Si thin film transistor," *Japanese journal of applied physics*, vol. 30, p. 3700, 1991.
- [11] A. Ogane, K. Hirata, K. Horiuchi, Y. Nishihara, Y. Takahashi, A. Kitiyanan, *et al.*, "Laser-doping technique using ultraviolet laser for shallow doping in crystalline silicon solar cell fabrication," *Japanese Journal of Applied Physics*, vol. 48, p. 071201, 2009.
- [12] J. Bovatsek, A. Tamhankar, R. Patel, N. Bulgakova, and J. Bonse, "Thin film removal mechanisms in ns-laser processing of photovoltaic materials," *Thin Solid Films*, vol. 518, pp. 2897-2904, 2010.

- [13] J. Kim and S. Na, "Metal thin film ablation with femtosecond pulsed laser," *Optics & Laser Technology*, vol. 39, pp. 1443-1448, 2007.
- [14] D. F. Williams, "On the mechanisms of biocompatibility," *Biomaterials*, vol. 29, pp. 2941-2953, 2008.
- [15] B. D. Ratner, "The biocompatibility manifesto: biocompatibility for the twenty-first century," *Journal of cardiovascular translational research*, vol. 4, pp. 523-527, 2011.
- [16] M. I. Sabir, X. Xu, and L. Li, "A review on biodegradable polymeric materials for bone tissue engineering applications," *Journal of Materials Science*, vol. 44, pp. 5713-5724, 2009.
- [17] M. Geetha, A. Singh, R. Asokamani, and A. Gogia, "Ti based biomaterials, the ultimate choice for orthopaedic implants—a review," *Progress in materials science*, vol. 54, pp. 397-425, 2009.
- [18] J. G. DELEE and J. Charnley, "Radiological demarcation of cemented sockets in total hip replacement," *Clinical orthopaedics and related research*, vol. 121, pp. 20-32, 1976.
- [19] S. Vervaeke, B. Collaert, J. Cosyn, E. Deschepper, and H. De Bruyn, "A Multifactorial Analysis to Identify Predictors of Implant Failure and Peri-Implant Bone Loss," *Clinical implant dentistry and related research*, vol. 17, pp. e298-e307, 2015.
- [20] S. Kurtz, K. Ong, E. Lau, F. Mowat, and M. Halpern, "Projections of primary and revision hip and knee arthroplasty in the United States from 2005 to 2030," *J Bone Joint Surg Am*, vol. 89, pp. 780-785, 2007.
- [21] T. Albrektsson and B. Albrektsson, "Osseointegration of bone implants: A review of an alternative mode of fixation," *Acta Orthopaedica Scandinavica*, vol. 58, pp. 567-577, 1987.
- [22] A. Kurella and N. B. Dahotre, "Review paper: surface modification for bioimplants: the role of laser surface engineering," *Journal of biomaterials applications*, vol. 20, pp. 5-50, 2005.
- [23] S. Bauer, P. Schmuki, K. von der Mark, and J. Park, "Engineering biocompatible implant surfaces: Part I: Materials and surfaces," *Progress in Materials Science*, vol. 58, pp. 261-326, 2013.
- [24] A. Tavangar, B. Tan, and K. Venkatakrisnan, "Synthesis of bio-functionalized three-dimensional titania nanofibrous structures using femtosecond laser ablation," *Acta biomaterialia*, vol. 7, pp. 2726-2732, 2011.
- [25] M. Jayaraman, U. Meyer, M. Bühner, U. Joos, and H.-P. Wiesmann, "Influence of titanium surfaces on attachment of osteoblast-like cells in vitro," *Biomaterials*, vol. 25, pp. 625-631, 2004.
- [26] K. Das, V. K. Balla, A. Bandyopadhyay, and S. Bose, "Surface modification of laser-processed porous titanium for load-bearing implants," *Scripta Materialia*, vol. 59, pp. 822-825, 2008.
- [27] M. Malinauskas, A. Žukauskas, S. Hasegawa, Y. Hayasaki, V. Mizeikis, R. Buividas, *et al.*, "Ultrafast laser processing of materials: from science to industry," *Light: Science & Applications*, vol. 5, p. e16133, 2016.

- [28] M. Rahmani, B. Lukiyanchuk, T. Tahmasebi, Y. Lin, T. Liew, and M. Hong, "Polarization-controlled spatial localization of near-field energy in planar symmetric coupled oligomers," *Applied Physics A*, vol. 107, pp. 23-30, 2012.
- [29] W. Schulz, U. Eppelt, and R. Poprawe, "Review on laser drilling I. Fundamentals, modeling, and simulation," *Journal of Laser Applications*, vol. 25, p. 012006, 2013.
- [30] A. Kiani, K. Venkatakrishnan, and B. Tan, "Direct laser writing of amorphous silicon on Si-substrate induced by high repetition femtosecond pulses," *Journal of Applied Physics*, vol. 108, p. 074907, 2010.
- [31] L. Jiang and H.-L. Tsai, "Modeling of ultrashort laser pulse-train processing of metal thin films," *International Journal of Heat and Mass Transfer*, vol. 50, pp. 3461-3470, 2007.
- [32] L. J. Lewis and D. Perez, "Laser ablation with short and ultrashort laser pulses: Basic mechanisms from molecular-dynamics simulations," *Applied Surface Science*, vol. 255, pp. 5101-5106, 2009.
- [33] P. Parandoush and A. Hossain, "A review of modeling and simulation of laser beam machining," *International Journal of Machine Tools and Manufacture*, vol. 85, pp. 135-145, 2014.
- [34] S. T. Hendow and S. A. Shakir, "Structuring materials with nanosecond laser pulses," *Optics express*, vol. 18, pp. 10188-10199, 2010.
- [35] C.-Y. Ho, H.-H. Ku, Y.-C. Lee, Y.-H. Tsai, and M.-Y. Wen, "Prediction of ablated region of ultrafast-pulse laser processing for alumina," *Materials Research Innovations*, vol. 19, pp. S5-744-S5-747, 2015.
- [36] G. Chen, Y. Wang, J. Zhang, and J. Bi, "An analytical solution for two-dimensional modeling of repetitive long pulse laser heating material," *International Journal of Heat and Mass Transfer*, vol. 104, pp. 503-509, 2017.
- [37] N. Ren, L. Jiang, D. Liu, L. Lv, and Q. Wang, "Comparison of the simulation and experimental of hole characteristics during nanosecond-pulsed laser drilling of thin titanium sheets," *The International Journal of Advanced Manufacturing Technology*, vol. 76, pp. 735-743, 2015.
- [38] P. Shukla and J. Lawrence, "Examination of temperature distribution and the thermal effects on Si₃N₄ engineering ceramics during fibre laser surface treatment," *Optics and Lasers in Engineering*, vol. 49, pp. 998-1011, 2011.
- [39] P. Weidmann, U. Weber, S. Schmauder, G. Pedrini, and W. Osten, "Numerical calculation of temperature and surface topology during a laser ablation process for ceramic coatings," *Meccanica*, vol. 51, pp. 279-289, 2016.
- [40] S. Sinha, "Thermal model for nanosecond laser ablation of alumina," *Ceramics International*, vol. 41, pp. 6596-6603, 2015.
- [41] C. J. Knight, "Theoretical modeling of rapid surface vaporization with back pressure," *AIAA journal*, vol. 17, pp. 519-523, 1979.
- [42] D. Marla, U. V. Bhandarkar, and S. S. Joshi, "Modeling nanosecond pulsed laser ablation: a focus on temperature dependence of material properties," *Manufacturing Letters*, vol. 2, pp. 13-16, 2014.

- [43] A. Foroozmehr, M. Badrossamay, and E. Foroozmehr, "Finite element simulation of selective laser melting process considering optical penetration depth of laser in powder bed," *Materials & Design*, vol. 89, pp. 255-263, 2016.
- [44] Y. Zhang, Z. Shen, and X. Ni, "Modeling and simulation on long pulse laser drilling processing," *International Journal of Heat and Mass Transfer*, vol. 73, pp. 429-437, 2014.
- [45] O. Anicic, S. Jović, H. Skrijelj, and B. Nedić, "Prediction of laser cutting heat affected zone by extreme learning machine," *Optics and Lasers in Engineering*, vol. 88, pp. 1-4, 2017.
- [46] W. A. El-Said, J.-H. Lee, B.-K. Oh, and J.-W. Choi, "3-D nanoporous gold thin film for the simultaneous electrochemical determination of dopamine and ascorbic acid," *Electrochemistry Communications*, vol. 12, pp. 1756-1759, 2010.
- [47] C.-C. Chang, N.-F. Chiu, D. S. Lin, Y. Chu-Su, Y.-H. Liang, and C.-W. Lin, "High-sensitivity detection of carbohydrate antigen 15-3 using a gold/zinc oxide thin film surface plasmon resonance-based biosensor," *Analytical chemistry*, vol. 82, pp. 1207-1212, 2010.
- [48] H. Frey and H. R. Khan, *Handbook of thin film technology*: Springer, 2010.
- [49] H. Randhawa, "Cathodic arc plasma deposition technology," *Thin Solid Films*, vol. 167, pp. 175-186, 1988.
- [50] J. Singh and D. Wolfe, "Review Nano and macro-structured component fabrication by electron beam-physical vapor deposition (EB-PVD)," *Journal of materials Science*, vol. 40, pp. 1-26, 2005.
- [51] J. D. Schiffman and C. L. Schauer, "A review: electrospinning of biopolymer nanofibers and their applications," *Polymer reviews*, vol. 48, pp. 317-352, 2008.
- [52] X. Zong, K. Kim, D. Fang, S. Ran, B. S. Hsiao, and B. Chu, "Structure and process relationship of electrospun bioabsorbable nanofiber membranes," *Polymer*, vol. 43, pp. 4403-4412, 2002.
- [53] Q. P. Pham, U. Sharma, and A. G. Mikos, "Electrospinning of polymeric nanofibers for tissue engineering applications: a review," *Tissue engineering*, vol. 12, pp. 1197-1211, 2006.
- [54] X. Geng, O.-H. Kwon, and J. Jang, "Electrospinning of chitosan dissolved in concentrated acetic acid solution," *Biomaterials*, vol. 26, pp. 5427-5432, 2005.
- [55] J. M. Deitzel, J. Kleinmeyer, D. Harris, and N. B. Tan, "The effect of processing variables on the morphology of electrospun nanofibers and textiles," *Polymer*, vol. 42, pp. 261-272, 2001.
- [56] M. G. McKee, G. L. Wilkes, R. H. Colby, and T. E. Long, "Correlations of solution rheology with electrospun fiber formation of linear and branched polyesters," *Macromolecules*, vol. 37, pp. 1760-1767, 2004.
- [57] H. Fong, I. Chun, and D. Reneker, "Beaded nanofibers formed during electrospinning," *Polymer*, vol. 40, pp. 4585-4592, 1999.
- [58] C. Zhang, X. Yuan, L. Wu, Y. Han, and J. Sheng, "Study on morphology of electrospun poly (vinyl alcohol) mats," *European polymer journal*, vol. 41, pp. 423-432, 2005.

- [59] P. Gupta, C. Elkins, T. E. Long, and G. L. Wilkes, "Electrospinning of linear homopolymers of poly (methyl methacrylate): exploring relationships between fiber formation, viscosity, molecular weight and concentration in a good solvent," *Polymer*, vol. 46, pp. 4799-4810, 2005.
- [60] B. Duan, C. Dong, X. Yuan, and K. Yao, "Electrospinning of chitosan solutions in acetic acid with poly (ethylene oxide)," *Journal of Biomaterials Science, Polymer Edition*, vol. 15, pp. 797-811, 2004.
- [61] R. Ravichandran, "Biomimetic surface modification of dental implant for enhanced osseointegration," Master of engineering, Bioengineering, ANNA University, 2009.
- [62] M. Chen, P. K. Patra, S. B. Warner, and S. Bhowmick, "Role of fiber diameter in adhesion and proliferation of NIH 3T3 fibroblast on electrospun polycaprolactone scaffolds," *Tissue Engineering*, vol. 13, pp. 579-587, 2007.
- [63] M. Iafisco, I. Foltran, S. Sabbatini, G. Tosi, and N. Roveri, "Electrospun Nanostructured Fibers of Collagen-Biomimetic Apatite on Titanium Alloy," *Bioinorganic chemistry and applications*, vol. 2012, 2012.
- [64] L.-l. Li, L.-m. Wang, Y. Xu, and L.-x. Lv, "Preparation of gentamicin-loaded electrospun coating on titanium implants and a study of their properties in vitro," *Archives of orthopaedic and trauma surgery*, vol. 132, pp. 897-903, 2012.
- [65] L. Zhang, J. Yan, Z. Yin, C. Tang, Y. Guo, D. Li, *et al.*, "Electrospun vancomycin-loaded coating on titanium implants for the prevention of implant-associated infections," *International journal of nanomedicine*, vol. 9, p. 3027, 2014.
- [66] Y. Raita, K. Komatsu, and T. Hayakawa, "Pilot study of gingival connective tissue responses to 3-dimensional collagen nanofiber-coated dental implants," *Dental materials journal*, vol. 34, pp. 847-854, 2015.
- [67] A. Rezaei and M. Mohammadi, "In vitro study of hydroxyapatite/polycaprolactone (HA/PCL) nanocomposite synthesized by an in situ sol-gel process," *Materials Science and Engineering: C*, vol. 33, pp. 390-396, 2013.
- [68] L. A. Bosworth and S. Downes, "Acetone, a sustainable solvent for electrospinning poly (ϵ -caprolactone) fibres: effect of varying parameters and solution concentrations on fibre diameter," *Journal of Polymers and the Environment*, vol. 20, pp. 879-886, 2012.
- [69] P. Hawkes and J. C. Spence, *Science of microscopy*: Springer Science & Business Media, 2008.
- [70] J. Goldstein, D. E. Newbury, P. Echlin, D. C. Joy, A. D. Romig Jr, C. E. Lyman, *et al.*, *Scanning electron microscopy and X-ray microanalysis: a text for biologists, materials scientists, and geologists*: Springer Science & Business Media, 2012.
- [71] B. D. Cullity and J. W. Weymouth, "Elements of X-ray Diffraction," *American Journal of Physics*, vol. 25, pp. 394-395, 1957.

- [72] L. Müller and F. A. Müller, "Preparation of SBF with different content and its influence on the composition of biomimetic apatites," *Acta Biomaterialia*, vol. 2, pp. 181-189, 2006.
- [73] T. Kokubo and H. Takadama, "How useful is SBF in predicting in vivo bone bioactivity?," *Biomaterials*, vol. 27, pp. 2907-2915, 2006.
- [74] A. Sakaguchi, M. Nakano, J. Hieda, N. Ohtake, and H. Akasaka, "Dependence of ion concentration in simulated body fluid on apatite precipitation on titania surface," *Applied Surface Science*, vol. 347, pp. 610-618, 2015.
- [75] P. N. Chavan, M. M. Bahir, R. U. Mene, M. P. Mahabole, and R. S. Khairnar, "Study of nanobiomaterial hydroxyapatite in simulated body fluid: Formation and growth of apatite," *Materials Science and Engineering: B*, vol. 168, pp. 224-230, 2010.
- [76] D. A. Anderson, J. C. Tannehill, and R. H. Pletcher, *Computational fluid mechanics and heat transfer*. Washington New York: Hemisphere Pub. Corp. ; McGraw-Hill, 1984.
- [77] T.-Y. Wang and C. C.-P. Chen, "Thermal-ADI-A linear-time chip-level dynamic thermal-simulation algorithm based on alternating-direction-implicit (ADI) method," *IEEE Transactions on very large scale integration (VLSI) systems*, vol. 11, pp. 691-700, 2003.
- [78] G. Welsch, R. Boyer, and E. Collings, *Materials properties handbook: titanium alloys*: ASM international, 1993.
- [79] H. Kwon, W.-K. Baek, M.-S. Kim, W.-S. Shin, and J. J. Yoh, "Temperature-dependent absorptance of painted aluminum, stainless steel 304, and titanium for 1.07 μm and 10.6 μm laser beams," *Optics and Lasers in Engineering*, vol. 50, pp. 114-121, 2012.
- [80] D. Chatterjee and S. Chakraborty, "An enthalpy-based lattice Boltzmann model for diffusion dominated solid-liquid phase transformation," *Physics Letters A*, vol. 341, pp. 320-330, 2005.
- [81] A. Bogaerts and Z. Chen, "Effect of laser parameters on laser ablation and laser-induced plasma formation: A numerical modeling investigation," *Spectrochimica Acta Part B: Atomic Spectroscopy*, vol. 60, pp. 1280-1307, 2005.
- [82] X. Mao and R. E. Russo, "Invited paper Observation of plasma shielding by measuring transmitted and reflected laser pulse temporal profiles," *Applied Physics A*, vol. 64, pp. 1-6, 1996.
- [83] N. Bulgakova, A. Bulgakov, and L. Babich, "Energy balance of pulsed laser ablation: thermal model revised," *Applied Physics A*, vol. 79, pp. 1323-1326, 2004.
- [84] V. Oliveira and R. Vilar, "Finite element simulation of pulsed laser ablation of titanium carbide," *Applied surface science*, vol. 253, pp. 7810-7814, 2007.
- [85] W. F. Gale and T. C. Totemeier, *Smithells metals reference book*: Butterworth-Heinemann, 2003.

- [86] C. Glassbrenner and G. A. Slack, "Thermal conductivity of silicon and germanium from 3 K to the melting point," *Physical Review*, vol. 134, p. A1058, 1964.
- [87] K. Ujihara, "Reflectivity of metals at high temperatures," *Journal of Applied Physics*, vol. 43, pp. 2376-2383, 1972.
- [88] J. E. Hatch and A. Association, *Aluminum: properties and physical metallurgy*: ASM International, 1984.
- [89] (April 19, 2017). Available: http://www.efunda.com/materials/elements/TC_Table.cfm?Element_ID=Au
- [90] A. Kiani and M. Radmanesh, "High-Energy Nanosecond Laser Pulses for Synthesis of Better Bone Implants," in *High Energy and Short Pulse Lasers*, ed: InTech, 2016.
- [91] F. A. C. Andrade, L. C. de Oliveira Vercik, F. J. Monteiro, and E. C. da Silva Rigo, "Preparation, characterization and antibacterial properties of silver nanoparticles–hydroxyapatite composites by a simple and eco-friendly method," *Ceramics International*, vol. 42, pp. 2271-2280, 2016.
- [92] K. Wong, A. Boyde, and P. G. Howell, "A model of temperature transients in dental implants," *Biomaterials*, vol. 22, pp. 2795-7, Oct 2001.
- [93] O. Feuerstein, K. Zeichner, C. Imbari, Z. Ormianer, N. Samet, and E. I. Weiss, "Temperature changes in dental implants following exposure to hot substances in an ex vivo model," *Clin Oral Implants Res*, vol. 19, pp. 629-33, Jun 2008.
- [94] Z. Patel and G. A. Geerts, "Temperature changes along a dental implant," *International Journal of Prosthodontics*, vol. 24, 2011.
- [95] M. Ashtiani and R. Imani, "Transient Heat Transfer in a Dental Prosthesis Implanted in Mandibular Bone," in *26th Southern Biomedical Engineering Conference SBEC 2010, April 30-May 2, 2010, College Park, Maryland, USA*, 2010, pp. 376-379.
- [96] L. M. Jiji, *Heat conduction*. New York: Begell House, 2000.
- [97] M. Lin, F. Xu, T. J. Lu, and B. F. Bai, "A review of heat transfer in human tooth—experimental characterization and mathematical modeling," *dental materials*, vol. 26, pp. 501-513, 2010.
- [98] R. L. McIntosh and V. Anderson, "A comprehensive tissue properties database provided for the thermal assessment of a human at rest," *Biophysical Reviews and Letters*, vol. 5, pp. 129-151, 2010.
- [99] U. Gaur, S. f. Lau, B. B. Wunderlich, and B. Wunderlich, "Heat capacity and other thermodynamic properties of linear macromolecules. VIII. Polyesters and polyamides," *Journal of Physical and Chemical Reference Data*, vol. 12, pp. 65-89, 1983.
- [100] F. Brown and K. R. Diller, "Calculating the optimum temperature for serving hot beverages," *Burns*, vol. 34, pp. 648-654, 2008.
- [101] D. Spierings, F. Bosman, T. Peters, and F. Plasschaert, "Determination of the convective heat transfer coefficient," *Dental Materials*, vol. 3, pp. 161-164, 1987.

- [102] C. Marambio-Jones and E. M. Hoek, "A review of the antibacterial effects of silver nanomaterials and potential implications for human health and the environment," *Journal of Nanoparticle Research*, vol. 12, pp. 1531-1551, 2010.
- [103] J. R. Morones, J. L. Elechiguerra, A. Camacho, K. Holt, J. B. Kouri, J. T. Ramírez, *et al.*, "The bactericidal effect of silver nanoparticles," *Nanotechnology*, vol. 16, p. 2346, 2005.

Appendix A – Physical and thermal properties of the materials

Aluminium

Atomic weight	26.98
Density (kg/m ³)	2700
Melting point (°C)	660
Boiling point (°C)	2519
Latent heat of fusion (kJ/kg)	397
Latent heat of vaporization (kJ/kg)	10800
Heat capacity (J/kgK)	897
Thermal conductivity (W/m ² K)	247
Coefficient of thermal expansion (µm/mK)	23.1

Gold

Atomic weight	196.97
Density (kg/m ³)	19300
Melting point (°C)	1064
Boiling point (°C)	2856
Latent heat of fusion (kJ/kg)	64
Latent heat of vaporization (kJ/kg)	1736
Heat capacity (J/kgK)	129
Thermal conductivity (W/m ² K)	317.9
Coefficient of thermal expansion (µm/mK)	14.2

Silicon

Atomic weight	28.08
Density (kg/m ³)	2340
Melting point (°C)	1412
Boiling point (°C)	3270
Latent heat of fusion (kJ/kg)	1788
Latent heat of vaporization (kJ/kg)	13637
Heat capacity (J/kgK)	705
Thermal conductivity (W/m ² K)	156
Coefficient of thermal expansion (µm/mK)	7.6

Titanium

Atomic weight	47.87
Density (kg/m ³)	4510
Melting point (°C)	1668
Boiling point (°C)	3287
Latent heat of fusion (kJ/kg)	296
Latent heat of vaporization (kJ/kg)	8880
Heat capacity (J/kgK)	523
Thermal conductivity (W/m ² K)	11.4
Coefficient of thermal expansion (µm/mK)	8.6

Appendix B – Laser processing simulation software

A graphical user interface was developed for the model introduced in this thesis (Figure 42). In this program, after entering all the input values (Figure 43), all the results will be shown in a very user friendly way.

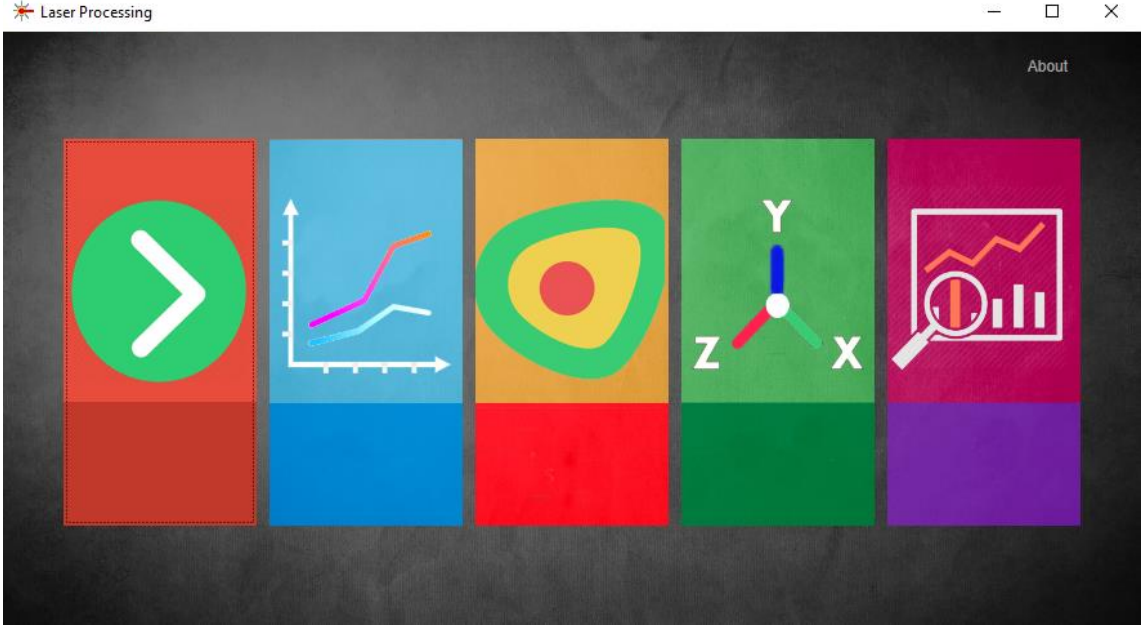


Figure 42 – The laser processing program

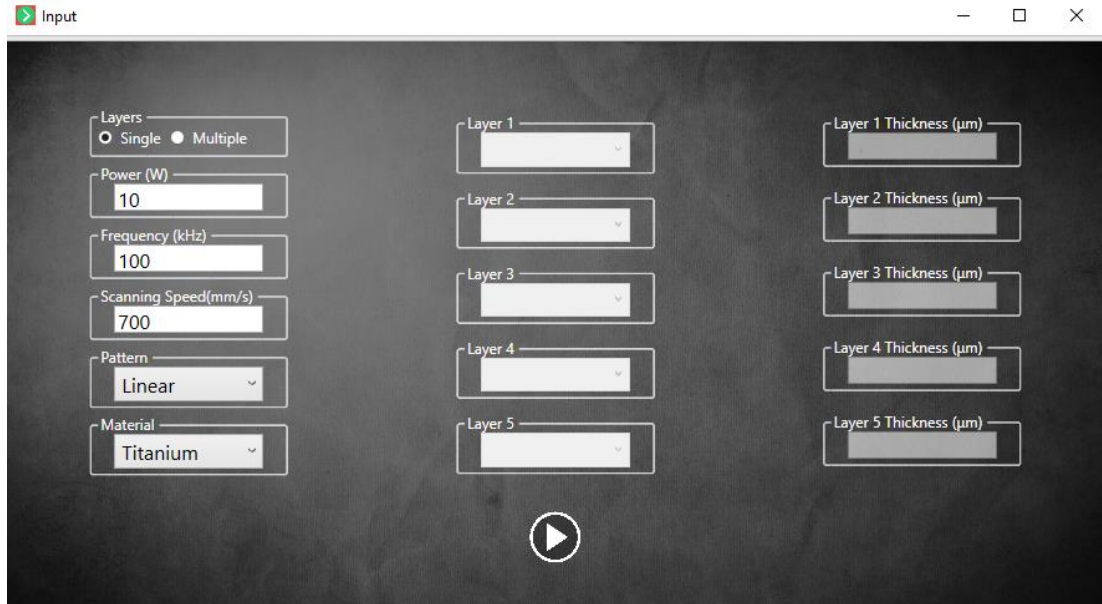


Figure 43 – Input values for laser processing of bulk materials and thin film multilayer structures.

By opening the “Line Graph” window (Figure 44), The groove/hole profiles and the molten zones are depicted as 2D graphs at different locations. Four different graphs can be shown simultaneously.

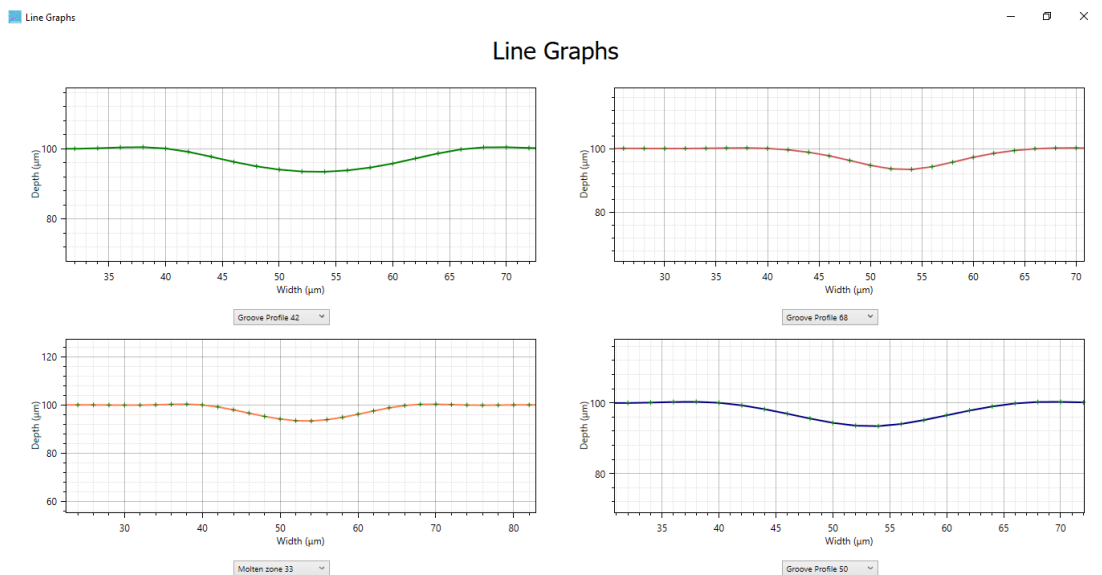


Figure 44 – The “Line Graph” window

The temperature contours at the surface and different cross-sections can be seen in the “Contours” window (Figure 45). Also by opening the “3D Graph” window (Figure 46), the ablated zone can be seen as a 3D graph. We can easily zoom in or out in all of these graphs and also in the 3D graph, we can rotate the object or in order to change the view.

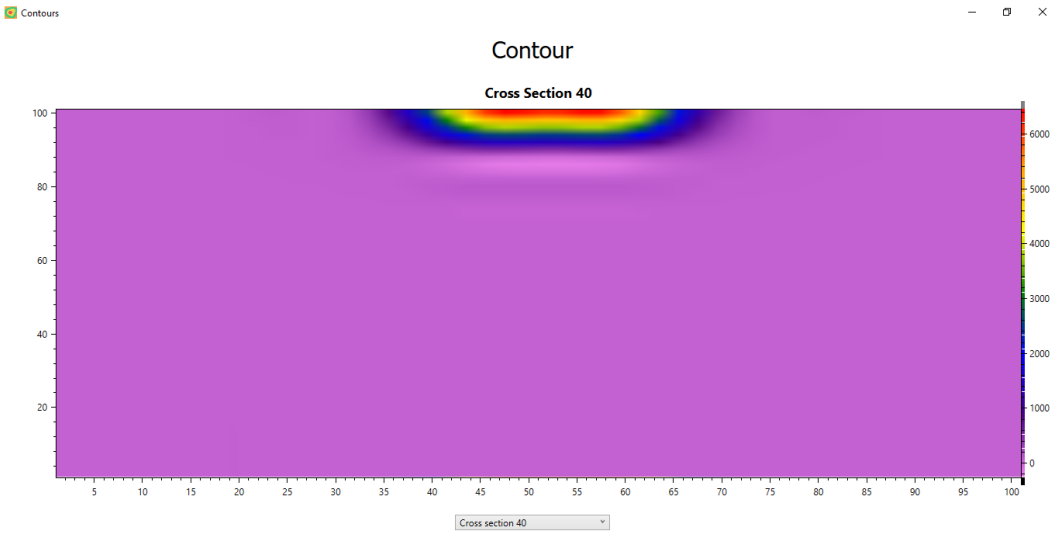


Figure 45 – The “Contours” window

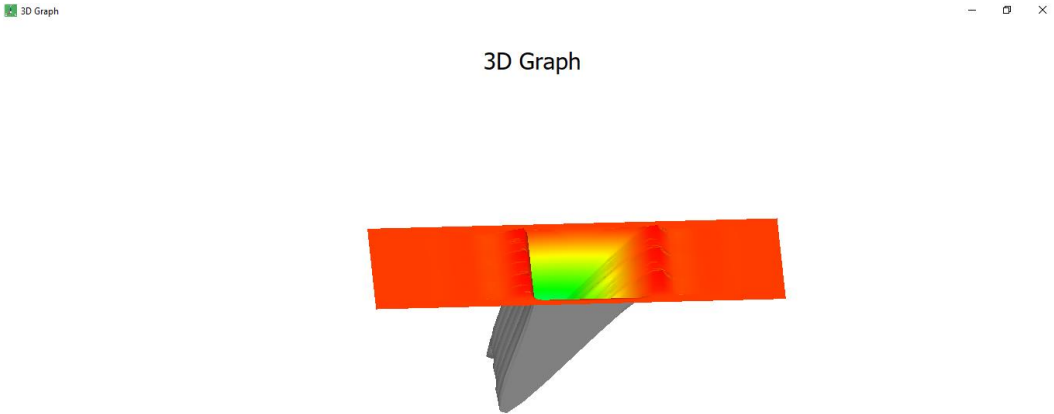


Figure 46 – The “3D Graph” window

Finally, a report will be generated that shows the laser parameters and materials as well as the minimum and maximum ablated depths and returns the average depth and standard deviation (Figure 47). Also. The report and all the graphs and contours can be easily printed on the paper.

The screenshot shows a window titled "Report" with a standard Windows-style title bar (minimize, maximize, close buttons). The window contains several input fields and a table of results.

Power (W)	Frequency (kHz)	Scanning Speed(mm/s)
10	100	700
Pattern	No. of Pulses	Avg. Temperature (°C)
LINEAR	31	2540

Layer 1	Layer 2	Layer 3	Layer 4	Layer 5
TITANIUM				
Thickness (μm)				
100	0	0	0	0

Minimum depth (μm)	Maximum depth (μm)	Average depth (μm)	Standard Deviation (μm)
2.12	4.81	4.02	0.99

Figure 47 – The “Report” window

Appendix C – List of publications

Journal papers:

1. Naghshine, B. B., Cosman, J. A., & Kiani, A. (2016). Synthesis of polycaprolactone-titanium oxide multilayer films by nanosecond laser pulses and electrospinning technique for better implant fabrication. *Journal of Applied Physics*, 120(8), 084304.
2. Naghshine, B. B., & Kiani, A. (2017). 3D transient model to predict temperature and ablated areas during laser processing of metallic surfaces. *AIP Advances*, 7(2), 025007.
3. Naghshine, B. B., & Kiani, A. (2017). 3D thermal modelling for laser processing of thin-film multilayer structures. *Beilstein Journal of Nanotechnology*, (Accepted).

Conference Paper:

1. Potential Use of Laser Processed Titanium, Coated with Electrospun Polycaprolactone Fibers to Modify Thermal Properties of Dental Implants, 33rd Annual Meeting of the Canadian Biomaterials Society

CURRICULUM VITAE

Name: Babak Baradaran Naghshine

Education:

M.Sc., Mechanical Engineering, University of New Brunswick (2016 – 2017)

M.Sc., Mechanical Engineering, Isfahan University of Technology (2011 – 2014)

B.Sc., Mechanical Engineering, Isfahan University of Technology (2007 – 2011)

Publications:

1. Refereed Journal Papers

1.1. Published

1. Naghshine, B. B., Cosman, J. A., & Kiani, A. (2016). Synthesis of polycaprolactone-titanium oxide multilayer films by nanosecond laser pulses and electrospinning technique for better implant fabrication. *Journal of Applied Physics*, 120(8), 084304.
2. Naghshine, B. B., & Kiani, A. (2017). 3D transient model to predict temperature and ablated areas during laser processing of metallic surfaces. *AIP Advances*, 7(2), 025007.

1.2. In Progress

1. Naghshine, B. B., & Kiani, A. (2017). 3D thermal modelling for laser processing of thin-film multilayer structures. *Beilstein Journal of Nanotechnology*, (Accepted).
2. Naghshine, B. B., & Saboonchi A. (2017). Optimized thin film coatings for passive cooling applications. *Optics Communications* (Under review).

3. Naghshine, B. B., Hassnpour S., & Saboonchi A. (2017). Heat transfer modeling of cold-rolled steel strip coils to assess the factors influencing the cooling cycle in hydrogen batch annealing process. Heat and Mass Transfer (Under review)

2. Conferences

2.1. Published Conference Papers

1. Potential Use of Laser Processed Titanium, Coated with Electrospun Polycaprolactone Fibers to Modify Thermal Properties of Dental Implants, 33rd Annual Meeting of the Canadian Biomaterials Society